



TAMPEREEN TEKNILLINEN YLIOPISTO
TAMPERE UNIVERSITY OF TECHNOLOGY

Erkka J. Frankberg

Plastic Deformation of Amorphous Aluminium Oxide

Flow of Inorganic Glass at Room Temperature



Julkaisu 1531 • Publication 1531

Tampereen teknillinen yliopisto. Julkaisu 1531
Tampere University of Technology. Publication 1531

Erkka J. Frankberg

Plastic Deformation of Amorphous Aluminium Oxide

Flow of Inorganic Glass at Room Temperature

Thesis for the degree of Doctor of Science in Technology to be presented with due permission for public examination and criticism in Konetalo Building, Auditorium K1702, at Tampere University of Technology, on the 2nd of March 2018, at 12 noon.

Doctoral candidate: Erkka Juhani Frankberg
Laboratory of Materials Science
Ceramic Materials Group
Faculty of Engineering Sciences
Tampere University of Technology
Finland

Supervisor: Erkki Levänen, Prof.
Laboratory of Materials Science
Ceramic Materials Group
Faculty of Engineering Sciences
Tampere University of Technology
Finland

Pre-examiners: Jérôme Chevalier, Prof.
MATEIS laboratory
Insitutit National des Sciences Appliquées de Lyon
France

Jari Juuti, Adjunct Prof.
Microelectronics and Materials Physics Laboratories
University of Oulu
Finland

Opponents: Jérôme Chevalier, Prof.
MATEIS laboratory
Insitutit National des Sciences Appliquées de Lyon
France

Roman Nowak, Prof.
Department of Chemistry and Materials Science
Aalto University
Finland

ISBN 978-952-15-4102-5 (printed)
ISBN 978-952-15-4108-7 (PDF)
ISSN 1459-2045

Abstract

This work is about properties of nanomaterials and inorganic glasses, precisely thin films of aluminium oxide (Al_2O_3 , nominal thickness of 20 – 50 nanometers). We show that a solid, amorphous, aluminium oxide thin film at room temperature behaves as a viscoplastic solid at a critical load and after which it deforms purely by viscous flow. We propose that the work of deformation for the viscous flow is given as

$$W_{\text{def}} = \frac{V_{\text{def}} * \rho}{M} Q_{\text{eff}}(\dot{\epsilon}), \quad [J] = \frac{[\text{m}^3] [\text{kg}/\text{m}^3]}{[\text{kg}/\text{mol}]} \left[\frac{\text{J}}{\text{mol}} \right],$$

where V_{def} is the plastic volume, ρ is density, M is molar mass and Q_{eff} is the effective activation energy. The critical load of viscous flow for amorphous solids is therefore given by

$$\sigma_{\text{crit}} = \frac{\rho}{M} Q_{\text{eff}}(\dot{\epsilon}), \quad \left[\frac{\text{N}}{\text{m}^2} \right] = \frac{[\text{kg}/\text{m}^3]}{[\text{kg}/\text{mol}]} \left[\frac{\text{J}}{\text{mol}} \right].$$

Hypothesis is tested in an experiment where we load pulsed laser deposited amorphous Al_2O_3 up to its critical load value near room temperature and up to 100% strain. Amorphous Al_2O_3 deforms elastoplastically up to a critical load and, at the critical load, solely by viscous flow, which is governed at the atomic level by diffusion activated by a strong gradient stress field. Parallel atomistic simulations verify the experimental results.

As nanomaterials are often amorphous (e.g. ceramic thin films) or contain large amounts of amorphous-like grain interfaces (e.g. polycrystalline nanomaterials), our theory gives valuable tools to interpret and engineer their mechanical properties. Results indicate that amorphous ceramics with nanoscale internal and surface flaws can be malleable and ductile in comparable magnitude as metals and predict that these materials have remarkable resistance to mechanical loads, wear and scratching. The presented results and theoretical considerations will help to understand complex plasticity phenomena in ceramics and glasses, such as plastic deformation during indentation experiments, grain boundary mediated superplasticity, creep assisted densification during pressure assisted sintering and static creep under constant load.

Forewords

Everything happens by movement of atoms. The atoms are set in motion according to principal physical laws, which determine the speed and direction of movement of each atom. The movement is not chaotic; atoms order themselves by various phenomena. As we currently lack a unified theory, we can say that the longest range ordering happens by gravity and the smallest range ordering by laws of quantum mechanics. These phenomena create finally the order of the Universe that we observe close around us and in deep space.

Yet we do not understand how fundamental physical laws can transform simple motion of atoms into deterministic action; we do not know why it is possible for me to make a decision to lift an apple in opposite direction to gravity. Decisions, consciousness and life itself are also motion of atoms to large extent, but we have not found reason why they became to exist. The inanimate Universe is more straightforward but eventually has given all the knowledge we now have, to understand the deterministic world. I believe we look for answers to any question, because we grave to find out why we exist. If we learn to understand the inanimate world, perhaps it will someday give us a glimpse of understanding of the deterministic world.

I fell in love with ceramic materials during my university studies, because they were difficult and there were more questions than answers. I am still in love and still many questions remain unanswered. What I learned is that often the most difficult task is to find the right question that has the potential to increase our understanding.

I am fundamentally a European. Without European border-crossing collaboration, we could have not reached our goal. I would like to give my best appreciation to all my European colleagues and friends at Institut National des Sciences Appliquées de Lyon, Istituto Italiano di Tecnologia Milano, Erich Schmid Institute of Materials Science Leoben, Helsingin yliopisto, Aalto-yliopisto and most of all Tampereen teknillinen yliopisto of all the help, discussions and feedback. Special thanks to Erkki Levänen, Karine Masenelli-Varlot, Fabio Di Fonzo and Jaakko Akola for trust and belief in me and our goal.

I Thank Tampere University of Technology graduate school, Tutkijat maailmalle - mobility grant, Tampere University of Technology strategic research funding, Centre Lyonnais de Microscopy (CLYM) and Réseau national de plateformes en Microscopie

Électronique et Sonde Atomique (METSa) for providing the resources to perform the research. Thank you Regina E. Kannisto and Matti P. Kannisto for everything. Thank you Niko V. Kannisto and Aki M. J. Kannisto for leading the way.

My deepest gratitude to my best friend and companion Annakaisa T. Frankberg for continued support, love and encouraging. This book was possible only because of you. I hope this work will be an inspiration to my children Alvar H. A. Frankberg, Urho A. Y. Frankberg and all of you thereafter, remember that sky is not the limit!

Finally, I sincerely agree that "Research is a journey you embark on with the hope that something unexpected will happen" - Bengt Holmström



Erkka J. Frankberg

21.5.2017

Strasbourg, France

The author's and supporting contribution

The people involved in the work have verified their supporting contributions.

Erkka J. Frankberg (**author**) planned and executed the research plan, and established all the necessary national and international collaborations required to accomplish the study. The **author** has written all discussion regarding the results and all presented original ideas originate from the **author**. The **author** developed the theory of plastic deformation of amorphous aluminium oxide. The **author** performed all TEM sample preparation and TEM characterization if not mentioned otherwise. The **author** developed the angled broad ion beam milling technique used to produce the necessary mechanical testing devices called “sapphire anvils”.

Francisco García Ferré and Fabio Di Fonzo at Italian Institute of Technology, Milano, Italy and Picodeon Oy Ltd at Ii, Finland, deposited the PLD films used in this study.

Siddardha Koneti at Insitut National des Sciences Appliquées de Lyon performed the TEM tomography measurements.

Lucile Joly-Pottuz, Erkka J. Frankberg and Karine Masenelli Varlot at Insitut National des Sciences Appliquées de Lyon, France, performed the *in situ* TEM mechanical compression and tensile test, STEM imaging and EDS mapping.

Turkka Salminen at Tampere University of Technology, Tampere, Finland and Thierry Douillard at Insitut National des Sciences Appliquées de Lyon, France, carried out the focused ion beam work.

Janne Kalikka and Jaakko Akola at Tampere University of Technology carried out the atomistic simulations.

Jouko Hintikka at Tampere University of Technology carried out the finite element simulations.

Mikko Hokka and Erkka J. Frankberg at Tampere University of Technology carried out the image correlation measurements.

Patrice Kreiml and Megan J. Cordill at Erich Schmid Institute of Materials Science, Leoben, Austria carried out the atomic force microscopy measurements

Physical concepts, symbols and abbreviations

All calculations in this book are based on SI-units if not mentioned otherwise.

In mechanical testing, the raw measurement data is collected as force F [N] measured by a force sensor. Force relates to the total work W [J] done by the test geometry by

$$W = Fs ,$$

where s [m] is the distance travelled under the load F [N]. In order to understand what is the mechanical loading capacity of the sample, the force is converted into stress σ [N/m²] in the sample as

$$\sigma = F/A ,$$

where A [m²] is the measure of contact area or cross-sectional area between the sample and the tool transmitting the force. True stress σ_t is defined as the momentary contact or cross-sectional area A_t under a load F

$$\sigma_t = F/A_t .$$

Engineering strain ε_E is the measure of relative deformation of a solid as

$$\varepsilon_E = l/l_0 ,$$

where l is the total elongation of the solid at each moment and l_0 is the original length of the solid or the measuring gauge.

Room temperature equals to be 300 K in this study.

Other physical concepts and symbols include:

U_0	Free energy in absence of stress [J]
V_0	Volume subjected to a uniform applied stress [m ³]
σ_{app}	Applied stress [N/m ²]
E	Young's modulus / Elastic modulus [Pa]
G	Shear modulus [Pa]

ν	Poisson's ratio []
c	Surface crack length [m]
h	Thickness of the crack [m]
γ	Surface energy [J/m ²]
c_{crit}	Critical crack length [m]
σ_f	Stress at fracture [Pa]
K_I	Stress intensity factor in tensile loading mode I [MPa · m ^{1/2}]
K_{Ic}	Critical stress intensity factor in tensile loading mode I [MPa · m ^{1/2}]
Y	Dimensionless stress intensity parameter, Griffith criterion []
Ω_{ion} or Ω	Ionic/Atomic volume [m ³ _{ions} /N _{ions}]
c_{ion}	Total concentration of ions diffusing through the solid [N _{ions} /m ³]
D_{ion}	Diffusivity / diffusion constant of ions [m ² /s]
Q	Driving energy for diffusion per ion [J/ion] or mole of ions [J/mol]
k_B	Boltzmann constant [J/K]
T	Temperature [K]
c_{vac}	Total concentration of vacancies diffusing through the solid [N _{vac} /m ³]
D_{vac}	Diffusivity of vacancies [m ² /s]
N_v	Concentration of vacancies [N _{vac} /m ³]
Q_v	Activation energy needed for creating a single vacancy [J]
N	Concentration of atomic sites [N _{sites} /m ³]
ρ	Density [g/m ³]
N_A	Avogadro constant []
M	Molar mass [g/mol]
A	Area [m ²]
t	Time [s]
ω	Dimensionless constant, Nabarro-Herring creep []
Ψ	Dimensionless constant, Coble creep []
ξ	Dimensionless constant, Viscous creep []
δ_{gb}	Thickness of the grain boundary [m]
η	Viscosity [Pa · s]
η_0	Bulk viscosity [Pa · s]
η_{eff}	Effective viscosity [Pa · s]
f	Volume fraction of grain boundary phase []
τ	Shear stress [Pa]
$\dot{\epsilon}$	Shear strain rate [1/s]
$\dot{\gamma}$	Shear strain rate [1/s]
ϵ	Strain []
T_g	Glass transition temperature [K]

W_{elastic}	Work of elastic deformation [J]
W_{plastic}	Work of plastic deformation [J]
W_{measured}	Experimentally measured total work [J]
$W_{\text{theor.}}$	Theoretically calculated total work [J]

Abbreviations:

PLD	Pulsed laser deposition
Al_2O_3	Aluminium oxide
nm	nanometer ($1 \cdot 10^{-9}$ m, 0.000000001 m)
TEM	Transmission electron microscope
SEM	Scanning electron microscope
DIC	Digital image correlation
FEM	Finite element method
AFM	Atomic force microscope

Contents

Abstract	3
Forewords	5
The author's and supporting contribution	7
Physical concepts, symbols and abbreviations	9
Contents	13
1. Introduction	15
1.1 Aims and scientific contribution of the study	17
1.2 Understanding brittle fracture	18
1.3 Plastic deformation of aluminium oxide: State of the art	23
1.4 Diffusion based plastic deformation of aluminium oxide.....	28
1.5 Creep deformation of aluminium oxide.....	33
1.6 Viscous flow of oxide ceramics	37
1.7 Shear banding and superplasticity	39
1.8 Size effects in plastic deformation of aluminium oxide.....	40
2. Methods and materials	43
2.1 Thin film deposition	43
2.2 TEM characterization sample preparation.....	45
2.3 TEM characterization	47
2.4 Tools development for in situ TEM mechanical testing.....	48
2.5 In situ TEM mechanical test sample preparation.....	50
2.6 Quantitative in situ mechanical testing in TEM	52
2.7 Measuring sample strain.....	55
2.8 Measuring contact and cross-sectional areas.....	59

2.9 Measuring deformation volume	60
2.10 Atomistic simulations	62
2.11 Finite element method simulations	63
3. Results and discussion	67
3.1 Structure and stability of pulsed laser deposited Al_2O_3	67
3.2 Tool development for in situ TEM mechanical testing.....	76
3.3 Characterization of the mechanical test samples.....	80
3.4 In situ TEM mechanical testing results	82
3.5 Simulated mechanical properties of amorphous Al_2O_3	92
3.6 Plastic deformation of amorphous aluminium oxide.....	96
3.7 Discussion on the mechanical behaviour of amorphous Al_2O_3	100
3.8 Theory of plastic deformation in amorphous Al_2O_3	109
3.9 Viscous behaviour of amorphous Al_2O_3 at room temperature	114
3.10 On the applicability of Nabarro-Herring and Coble creep	120
3.11 Modelling the stress-strain behaviour of amorphous Al_2O_3	122
4. Conclusions	131
References	133

1. Introduction

A coffee mug falls and shatters to pieces on the floor, spilling the dark substance on my light coloured fluffy carpet. In an instant I know that the carpet is forever stained and bite my lip while I scrape the floor with a wet towel.

This is the familiar nature of ceramic bulk materials, such as aluminium oxide (Al_2O_3): brittleness and fracture on impact. Based on the traditional view on mechanical properties of materials, we understand that at room temperature, ceramic materials have very limited capability of deforming plastically and because of that, improving ceramics resistance to fracture has been one of the primary scientific goals in materials science for decades.

In engineering, ceramics have many outstanding properties compared to metals and polymers, such as resistance to extreme heat, diffusion, corrosion and wear. In addition, ceramic materials exhibit a range of functional properties such as dielectricity, semiconductivity, photocatalysis, superconductivity, piezoelectricity and bioactivity. Main obstacle between wider utilization of ceramics superior capabilities in engineering is the brittleness of these ionic and/or covalently bonded materials [1, 2]. Ceramic lattice is prone to fracture which typically limits the ultimate strength to less than one percent compared to their theoretical strength [1, 2]. Main reasons for this are the lack of dislocation motion at low temperatures [3] and that the ceramic materials typically have a set of internal and surface flaws, which act to concentrate stress during loading leading to fracture [4, 5]. We can demonstrate the catastrophic nature of brittle failure simply by falling a coffee mug to a hard floor as shown in **Figure 1.1**.

However, when manufactured at nanoscale, ceramics can show significant increase in ductility [6, 7, 8, 9]. So far, the observed plasticity phenomena in aluminium oxide has been limited to 1 - 100 nm at least in two dimensions. Therefore the important questions for materials science now are: **(i)** whether the plastic behaviour can be transferred into a continuous material, 2D film or 3D bulk etc.; **(ii)** what is the microstructure of such a continuous material and **(iii)** what is the mechanism behind the hypothetical plasticity of the relevant microstructure. And most of all, can these phenomena be observed at ambient temperature where most of the engineering applications have to function?

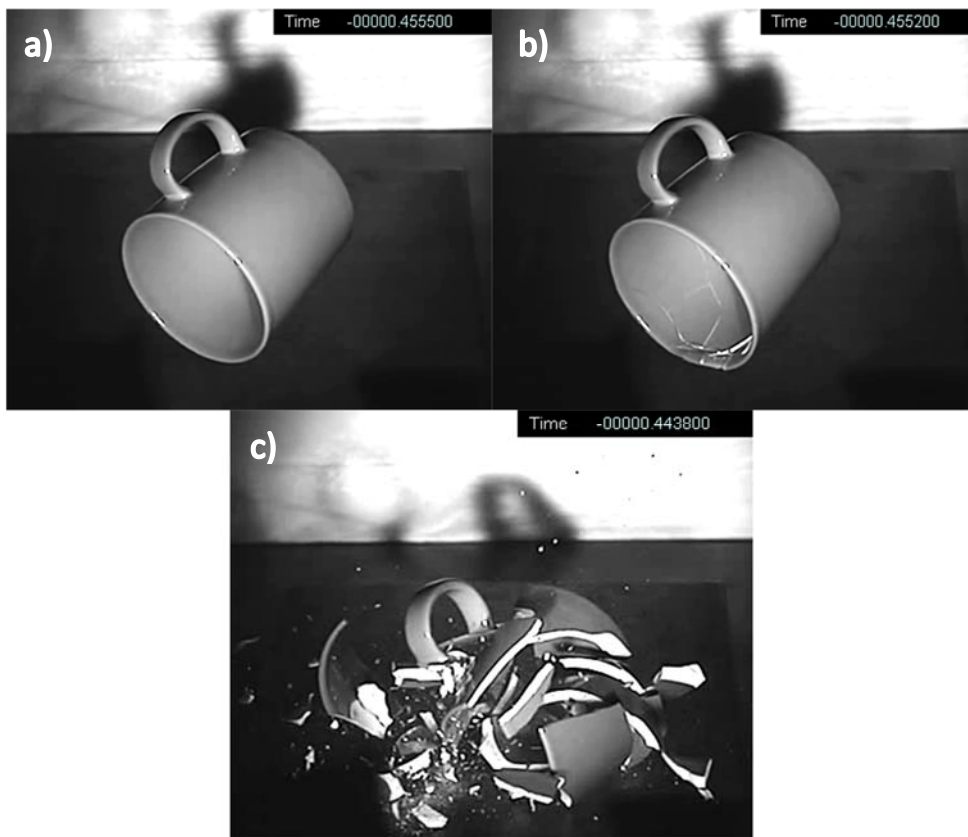


Figure 1.1: A coffee mug falling to the floor imaged using a high-speed camera. a) The coffee mug imaged in contact with the floor, b) only 0.3 ms later cracks have propagated through the structure, at the speed of sound, destroying the load bearing capability, and c) the mug shatters to numerous pieces by catastrophic failure. Copyright Erkkä J. Frankberg, Tampere University of Technology 2013

We selected aluminium oxide (Al_2O_3) as the study material for several reasons. First, it is normally extremely brittle in all single crystal and polycrystalline forms, and secondly it is a fundamentally important engineering material for the world: Oxygen (O) and Aluminium (Al) are the first and third most abundant elements in the earth's crust making AlO derivatives extremely abundant. As an example, the world production of Al_2O_3 in 2015 was 116 700 thousand metric tonnes [10], which is roughly 1/14 of the world's annual crude steel production (1 620 000 thousand metric tonnes [10]). Relatively cheap and abundantly available engineering ceramic, such as aluminium oxide, with room temperature plasticity would be a breakthrough in the field of engineering.

I am inclined to believe that material properties are not constant and can be changed by their surroundings. This is shown for example when steel wears down. The wear behaviour will be very different if you would wear it down in concentrated sulphuric acid, or you would heat the steel to 500 °C and then wear it down. The mechanical properties of materials are also constant only by our perception. If our existence would be based for example on a chemistry working at 1600 °C, we would never notice Al_2O_3 or most other ceramics to be brittle. As an example, it is recently shown that if you shoot a highly energetic electron beam through thin silica glass fiber, it will deform plastically even at room temperature! [11]. To make sense to it, similar conditions are observed quite close to us, in the space beyond Earth's magnetosphere, because the Sun is actually a huge electron gun. Here, a high temperature cannot be used to increase ductility; therefore, we search a solution from the extremely small structures (10^{-9} m) of aluminium oxide. The authors previously published work related to this topic are listed in references [12, 13, 14, 15, 16].

1.1 Aims and scientific contribution of the study

The quest for this study is to look for the theoretical and practical limits of the capability of ceramics and inorganic glass for plastic deformation. The main research question is: *Can amorphous ceramics/inorganic glasses flow at room temperature and significantly below the glass transition temperature?*

We study the materials capability for room temperature plasticity by conducting experimental mechanical tests *in situ* in transmission electron microscope. This allows us to observe and record visually the mechanism of plastic deformation in parallel to measuring the numerical mechanical response using suitable measuring devices. In addition, we study the mechanism of deformation by simulating the atomic structure and its behaviour under mechanical stress. Simulations gives tools to quantify and cross-verify the experimental results and yields insight to the deformation mechanisms that is not obtainable by experimental means. Leaning on the combined experimental and simulated results, we propose a theory explaining the observed mechanical response of amorphous aluminium oxide thin films.

The presented *thesis* suggests:

1. Amorphous aluminium oxide can flow/deform plastically at room temperature (300 K) and significantly below glass transition temperature

2. Proposal of a theory explaining the origin and predicting the work of deformation, flow stress and strain rate related properties and mechanisms in amorphous aluminium oxide
3. Demonstration that amorphous ceramics free of internal and surface flaws can be malleable and ductile in comparable magnitude as metals and predict that these materials have remarkable resistance to mechanical loads, wear and scratching.
4. The presented results and theoretical considerations will help to understand complex plasticity phenomena in materials, especially in ceramics including a glassy phase, such as plastic deformation during indentation experiments, grain boundary mediated superplasticity, creep assisted densification during pressure assisted sintering and static creep under constant load.

But first, in order to understand how ceramics can be plastic, we have to understand why ceramics are brittle.

1.2 Understanding brittle fracture

Aluminium oxide is a well-known gemstone appearing in various different colours. They are all called “sapphire” except the red colour (and pink) which is called the “ruby”. The signature blue colour of a sapphire comes from combined iron and titanium impurities by a phenomenon called “cooperative charge transfer” and the red colour of ruby comes directly from chromium impurity atoms. The atom bonding of aluminium oxide is characterized by ionic bonding with 63% ionic nature and the structure has no free electrons [17]. The electrons of aluminium and oxygen bind so strongly that they cannot interact with the energy available in the visible light spectrum and therefore a pure single crystal of $\alpha\text{-Al}_2\text{O}_3$ phase (also called sapphire) is completely transparent and colourless. Aluminium oxide characteristically responds to overloading by sudden brittle fracture, and although it is just below diamond in the traditional Mohs mineral hardness scale, a hammer blow can easily shatter it to small pieces (the case also for diamond!). In order to improve the deformation capability of aluminium oxide, we must understand why it is brittle, why ceramics are brittle.

Most solid materials have three distinctive forms of existence that dictate much of their mechanical properties. As shown in **Figure 1.2**, the material can be a single crystal with clear long range ordering of atoms, or the material can be polycrystalline; made up of several single crystals lowering the degree of long-range

order, or the material can be in amorphous/glassy state where no long range ordering exists. Let us consider all possible ways of plastic deformation for the different degrees of ordering.

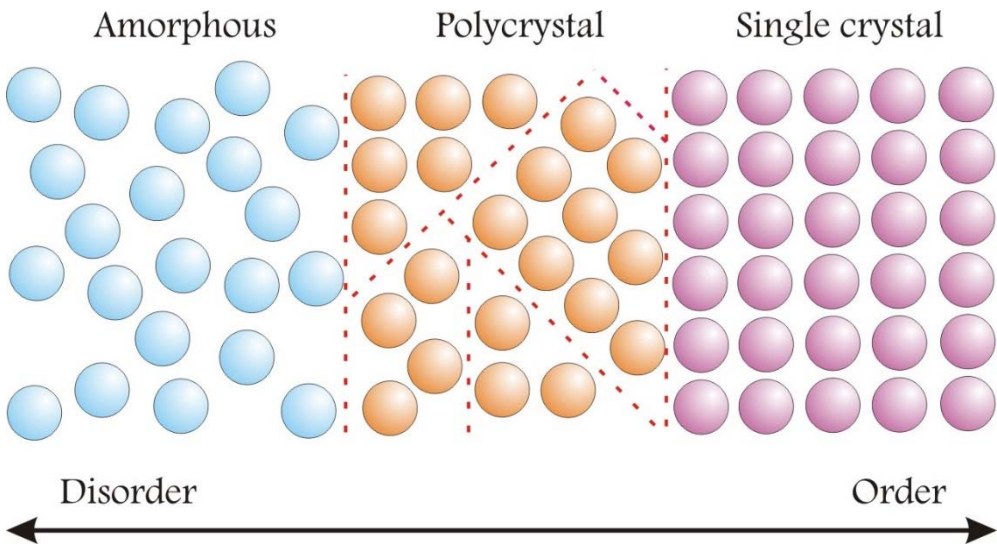


Figure 1.2: Atoms in a solid material can arrange by various configurations in which the degree of long range ordering changes. Copyright Erkka J. Frankberg 2017.

Plastic deformation can be defined as movement of vast amounts of ions/atoms relative to each other, which requires breaking of original bonds with neighbouring atoms and then reforming bonds with new neighbouring atoms [17]. The consequence is that once stress is relieved, ions/atoms do not return to their original positions. For single crystals of ceramics (and metals), the main source of plastic deformation is thought to be dislocation motion or dislocation “slip” [18]. In ceramics, more work is needed to create and move a dislocation as ceramics have a stronger atom bonding, and the single crystal structure of ceramics is more complicated than in metals because it usually consists of two or more different elements. The force acting against a moving dislocation is called the Peierls-Nabarro force or lattice friction, which needs to be overcome in order to move a dislocation one-step forward. For example, the average stress in aluminium oxide single crystal, needed to overcome Peierls barrier can be estimated to be in the range of 1000’s of megapascals, when for aluminium metal single crystal the same barrier is around 10’s of megapascals [18]. Requirement of charge neutrality adds to the complexity of the dislocation formation in ceramics [1], which is illustrated in **Figure 1.3** with an edge dislocation moving in a simple cubic sodium chloride (NaCl) crystal.

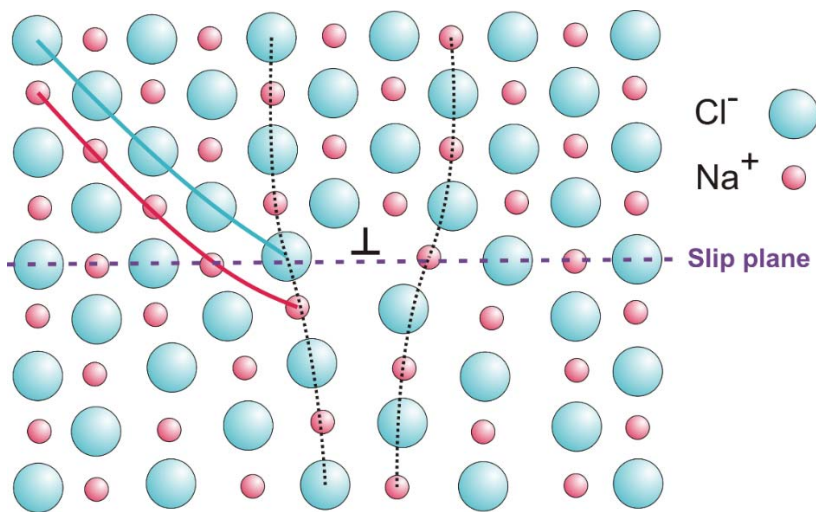


Figure 1.3: Dislocation core (\perp) in a simple cubic and ionic sodium chloride (NaCl) single crystal. Charge neutral dislocation is created here by adding extra plane of Na^+ (red line) and Cl^- (turquoise line) ions. Dislocation moves from left to right along the indicated slip plane. Note that a dislocation cannot propagate if a suitable long range ordering does not exist. Adapted from Barsoum [1], copyright Erkka J. Frankberg 2017.

Some geometrically simple ceramic single crystals such as magnesium oxide (MgO) and lithium fluoride (LiF) can go through limited amount of plastic deformation by dislocations before fracture [18]. However, as the dislocation movement is hard in ceramic crystal, and becomes harder as dislocations interact during the plastic deformation, the work needed to brake an atom bond eventually becomes lower compared to the work needed to drive the dislocations forward.

As the first bond brakes it creates a geometrically sharp flaw or “crack” that concentrates the pre-existing load to the tip of the crack. This leads to a cascade of atom bonds breaking at the crack tip because after each bond breaking there are less atom bonds to hold the same load. In ceramics, the crack is not easily deflected by creation of new dislocations at the crack tip and therefore the crack propagates catastrophically through the whole crystal [1].

A quantitative approach to fracture initiation was given by Griffith [5] in a theorem, which is now commonly known as the “Griffith criterion”. The basic idea is to balance the amount of elastic energy released in fracture to the energy consumed by creation of two new surface in the material. The fracture begins, when the stored

elastic energy overcomes the energy needed to create new surfaces. For a uniformly stressed bulk with a surface crack, the total energy for the combination becomes

$$U_{\text{tot}} = U_0 + \underbrace{\frac{V_0 \sigma_{\text{app}}^2}{2E} - \frac{\sigma_{\text{app}}^2}{2E} \left[\frac{\pi c^2 h}{2} \right]}_{\text{Elastic strain energy}} + \underbrace{2\gamma ch}_{\text{Energy related to formation of new surface}}, \quad (1.1)$$

where U_0 is the free energy in absence of stress, V_0 volume subjected to a uniform applied stress σ_{app} , E is the Young's modulus, c is the surface crack length and h is the thickness of the crack (and the material plate) and γ is the surface energy of the material (for detailed derivation of the equation see 1, 5 and 18). We assume that the fracture will happen right after maximum value of U_{tot} where we reach a critical crack length c_{crit} . To find the curve maximum, we can differentiate the **equation (1.1)** that is equated to zero and if we exchange σ_{app} with the stress at fracture σ_f , the equation can be reduced to

$$\sigma_f \sqrt{\pi c_{\text{crit}}} \geq \sqrt{2\gamma E}, \quad (1.2)$$

where the left hand side equation is often named as the “stress intensity factor” K_I [$\text{MPa}\sqrt{\text{m}}$] and the right hand side is called the “critical stress intensity factor” K_{IC} . The equation tells us that fracture will initiate when the stress intensity, the combination of stress and atomically sharp crack length, reaches a critical value. As the geometry of the specimens change, loading and the crack geometry can vary, we can correct the stress intensity factor by using a dimensionless stress intensity parameter Y [17] which yields

$$\sigma_f Y \sqrt{\pi c_{\text{crit}}} \geq K_{IC}. \quad (1.3)$$

For example a thin plate of infinite width and a through thickness crack with length $2c$ would have a value $Y = 1.0$ and for a semi-infinite plate with edge crack with length c would have a value $Y \cong 1.1$ [17]. Additionally for a thin specimen, the K_{IC} depends on the specimen thickness, but when the bulk thickness becomes much larger than the crack dimensions, the stress intensity factor becomes independent of bulk thickness [17]. Finally, we can argue that the stress intensity factor can never be larger than energy required to produce new surfaces. Therefore, we can conclude that fracture initiates when

$$K_I = K_{Ic} . \quad (1.4)$$

The surface energy is difficult to measure accurately for a given ceramic structure, therefore the values of K_I are mostly experimentally measured. Experimental fracture tests allow effective comparison of the “fracture toughness” of different ceramics. The Griffith criterion is found accurate when truly brittle materials $\gamma \approx 1 \text{ J/m}^2$ such as inorganic glasses are studied [18]. For $\alpha\text{-Al}_2\text{O}_3$, the surface energy has been determined to be in range of $2 - 4 \text{ J/m}^2$ depending on the crystal orientation [19]. In ductile materials, a plastic zone is created at the vicinity of highly stressed crack tip, which dissipates stored elastic energy as heat, and therefore the Griffith criterion gives exaggerated values for the surface energy γ . Griffith’s theorem was further developed to include also fracture of more ductile materials by Irwin [20].

In a perfect single crystal, a dislocation can move through the whole structure with more or less the same amount of work per step, since every step is identical (excluding the case when dislocations interact). In polycrystals, consisting of two or more crystals bound together, we have to consider that the dislocations need to transfer over the crystal boundary. As **Figure 1.2** illustrates, the shift in atomic long-range order between neighbouring crystals forces the dislocation to shift direction at the grain boundary. In ceramics, the shift is particularly difficult as the dislocation can move easily only in few slip planes. The Von Mises criteria states that a polycrystal must have five independent slip planes in order to accommodate three-dimensional plastic deformation [18, 21].

For example in the case of aluminium oxide we have 2 active slip planes at room temperature and only at 1600°C , 5 planes become active after which the dislocation based deformation is possible [18], another example is MgO which can deform plastically as a single crystal but is extremely brittle in polycrystalline form. In polycrystals, the flaw, which concentrates the stress, can also be the grain boundary between two crystals, as dislocation transfer through the disordered crystal boundary requires extra work. If the dislocation movement is blocked at the grain boundaries, eventually the same reasons lead to fracture as for the single crystal.

As the size of the single crystals become close to size of a single ion or few ions or atoms, say for example by melt quenching a liquid ceramic, we reach an amorphous state, a glass structure, where no long-range order of ions exists anymore (**Figure 1.2**). Dislocation slip requires long-range order of ions/atoms, which allow a series of exactly equal ion/atom steps through the whole crystal, therefore we rely on other mass transfer routes for inducing plastic deformation in amorphous materials.

As we do not have low energy passage ways e.g. slip planes for atoms to move, the atoms have to move step-by-step with each step requiring varying amount of work. The required work is distributed as each step the atom takes has a different geometry. This process is called viscous flow and as the name implies a material going through viscous flow behaves more as a liquid than a solid with a measurable viscosity. In this case, a wide distribution of atom steps need to be possible in order for the material to flow. If work is too low for higher energy atom steps, the process is too slow and the material builds up elastic stress until stepwise bond breakage leading to fracture. The energy for a single atom step is generally high in ceramics and it is therefore understandable that this process often requires high thermal activation energy. In the amorphous state, Peierls-Nabarro stress for a single dislocation step is of a same order of magnitude as in the case of a single crystal.

In reality, and mainly due to the used processing methods, crystalline and glassy ceramic materials are not perfect. Instead, the ionic structure has always a ready set of internal and surface flaws, which act to concentrate the stress during loading. At critical stress, crack propagates catastrophically from a pre-existing flaw leading to fracture of the material. Fracture toughness is a measure of materials intrinsic ability to resist fracture and for most ceramic materials, it can be estimated using the Griffith criterion introduced earlier. Traditionally based on the criterion, we improve the fracture toughness of ceramics by lowering the size of the internal flaws [22], by bridging the forming crack by fibre addition [23], by deflecting the crack propagation by engineering the grain shape [1], or by tailoring a rod-like grain structure for the material to maximize the creation of new surface upon fracture [24]. Perhaps most successfully the stress activated phase transformation of ZrO_2 has been used to improve fracture toughness of advanced ceramics [25]. Today these materials have numerous industrial applications, but in spite of strong research efforts, the room temperature fracture toughness of the toughest ceramics is still well below the fracture toughness of the most brittle metals.

1.3 Plastic deformation of aluminium oxide: State of the art

$\alpha\text{-Al}_2\text{O}_3$ is thermodynamically the most stable atomic arrangement, or “phase” of aluminium oxide [26]. Generally, the mechanical properties of the single- and polycrystalline $\alpha\text{-Al}_2\text{O}_3$ are well characterized as a function of temperature and the quantified data shows little possibility for plastic deformation close to room temperature or at ambient hydrostatic pressure. However, as we will discuss in this chapter, it is also known that when temperature is increased to several hundreds of degrees and a confining hydrostatic pressure is applied, crystalline Al_2O_3 can deform

plastically by slipping and twinning and by time dependent diffusion mechanisms related to viscous flow.

Nevertheless the simplest and the most striking evidence that plastic deformation happens even at room temperature and ambient pressure in all amorphous, crystalline and polycrystalline phases of Al_2O_3 is the simple hardness test using a diamond indenter. Measuring hardness is based on measuring the dimensions of a residual indent, in other words, the permanent mark left by the indenter on the material surface at room temperature. An example is shown in **Figure 1.4** where a residual indent is induced on a $\alpha\text{-Al}_2\text{O}_3$ / 2.5 vol. % nickel nanocomposite surface. The rectangular mark originates from the pyramid shape of the indenter. Cracks propagate from the corners of the indent, but the indenter mark itself is free of cracks indicating plastic material flow. Note that the crystal size of $\alpha\text{-Al}_2\text{O}_3$ is more than 40 times smaller than the diagonal diameter of the residual indent. This means that the plastic deformation is happening in a polycrystalline $\alpha\text{-Al}_2\text{O}_3$ at room temperature!

The paradox is that the dislocation theory introduced in previous chapter does not support the mechanism of plastic deformation at room temperature and ambient pressure in a single or polycrystalline aluminium oxide. To accommodate plastic deformation, the dislocations need to be mobile at a given temperature, but in reality the readily observed ultimate fracture strength ($\approx 0.1 - 1$ GPa) of single and polycrystalline Al_2O_3 is well below the minimum shear stress, ≈ 4.4 GPa at room temperature (RT) [3, 27], needed to activate even the most preferred prismatic slip plane. In the special case of single crystal Al_2O_3 whiskers, which are short and thin fibers of 1 – 10 micrometers in diameter, the ultimate tensile strength can be 20 GPa [28]. Furthermore, to accommodate three-dimensional deformation in a polycrystalline material (for example to induce a residual indent in hardness test); minimum five independent slip systems are needed as given by the von Mises criteria. For α -phase at room temperature, there are only two independent prismatic slip planes active as shown in **table 1.1**.

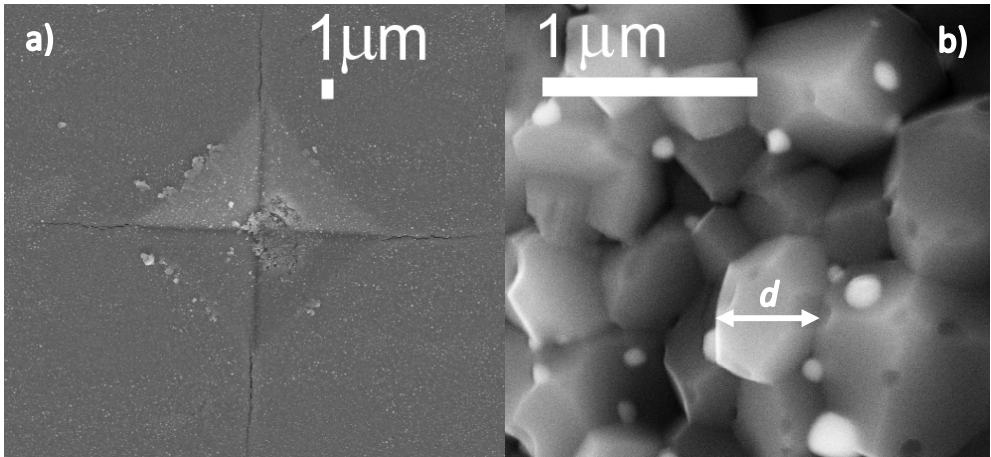


Figure 1.4: a) Top view of a residual indent mark left on the surface of a polycrystalline Al_2O_3 -Ni 2.5 Vol. % nanocomposite. Permanent plastic deformation created a residual indent with a diagonal diameter of $28.3\ \mu\text{m}$ and cracks have propagated from each corner of the residual indent. b) Cracked surface of the composite illustrating the average $\alpha\text{-Al}_2\text{O}_3$ crystal diameter (d) of $0.6 \pm 0.1\ \mu\text{m}$. Nickel can be seen as smaller grains with white colour. Copyright Erkka J. Frankberg 2012

Table 1.1: Slip systems in $\alpha\text{-Al}_2\text{O}_3$ single crystal at ambient pressure [18]

System name	Preferred slip system	Slip systems	Remarks
Basal	$> 600\ ^\circ\text{C}$	$(0001)1/3 < 2\bar{1}\bar{1}0 >$	Dominant system, occurs above $1100\ ^\circ\text{C}$ under shear at 1 atm. pressure
Prismatic	$< 600\ ^\circ\text{C}$	$\{1\bar{2}10\} < 10\bar{1}0 >$ $\{1\bar{2}10\} < 10\bar{1}1 >$	Occurs above $1600\ ^\circ\text{C}$ under shear at 1 atm. pressure
Pyramidal	-	$\{1\bar{1}02\} < 10\bar{1}1 >$ $\{10\bar{1}1\} < 01\bar{1}1 >$	Occurs above $1600\ ^\circ\text{C}$ under shear at 1 atm. pressure

In $\alpha\text{-Al}_2\text{O}_3$ crystals, the actual preferred low energy slip plane at low temperature ($< 600\ ^\circ\text{C}$) are the prismatic planes, but at higher temperature $> 600\ ^\circ\text{C}$ the basal plane becomes the low energy slip system, while rhombohedral twinning is also an important deformation mechanism at low temperatures [27, 29, 30]. However, with current manufacturing technology, for a macroscopic single crystal, at ambient pressure, a temperature above $1100\ ^\circ\text{C}$ is needed to activate any measurable plastic

strain [27], therefore basal slip system is the observed dominant system, while prismatic planes overcome the basal planes as the active slip system only at very high temperature of up to 1600 °C [18]. A molecular dynamic simulation study points out the inertness of the pyramidal slip planes up to very high temperatures [31]. Moreover, for polycrystalline α -Al₂O₃ the situation is largely inert, as five independent slip systems are active only from 1600 °C onwards.

However, if an α -Al₂O₃ crystal is subjected to high hydrostatic pressure, the room temperature plasticity of α -Al₂O₃ single crystal suddenly becomes plausible. Nobel laureate Percy Bridgman did one of the first tests for aluminium oxide crystals under hydrostatic pressure. In their studies, they first used single crystal rods of α -Al₂O₃ having visible bubbles or other flaws, which were enclosed in a hydrostatic pressure of 2400 MPa encapsulated in a thin copper sheet, at room temperature [32]. Under tensile stress of 860 – 960 MPa the flawed rods, quoting Bridgman, “Did not break at all, but failed by slip along well-defined slip planes, without loss of cohesion.” [32]. When using samples with no visible flaws the tensile stress was raised up to the maximum available value of 2800 MPa and the samples did not break and no evidence of permanent deformation was found [32]. Samples having minute flaws were subjected to compressive load and showed slow creep along defined slip planes at 2300 MPa as shown in **Figure 1.5**. When visually flaw free samples were subjected to compressive stress under hydrostatic pressure of 2400 - 2700 MPa encapsulated in a lead sheet, the samples failed by severe twinning or by slip at pressures of 5200 MPa and 9000 MPa respectively, depending on the loading angle of the crystal. The twinned distorted sample still held a 3400 MPa load after twinning. [32]

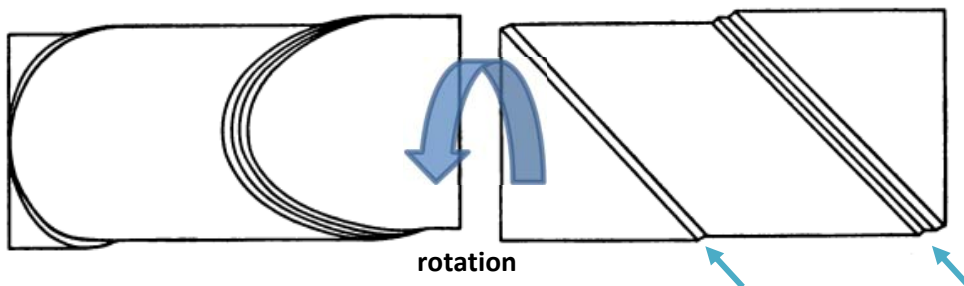


Figure 1.5: Slipping by defined slip planes in a single crystal α -Al₂O₃ under simple compressive stress at 2300 MPa and supported by hydrostatic pressure. Specimen was inspected to have minute internal flaws prior testing. [32] Reprinted under Google-digitized public domain rights.

Later Castaing *et al.* expanded the work of Bridgman to high temperatures up to 1800 °C under hydrostatic pressure of 1500 MPa and showed that the basal plane becomes the preferred slip system over the temperature of 1000 °C and as temperature is further increased, the needed critical stress along basal plane significantly decreases [33]. Further studies of single crystal α -Al₂O₃ at hydrostatic pressure of 1500 MPa showed that basal $\frac{1}{3}\langle 11\bar{2}0 \rangle(0001)$ dislocations and rhombohedral twinning can be activated beginning from 600 °C [34]. In addition, prismatic slip has been shown to have mobility as early as 200 °C under hydrostatic pressure with a resolved shear stress of ≈ 3 GPa [35].

Moreover Snow *et al.* performed mechanical test on polycrystalline α -Al₂O₃ under hydrostatic pressure of 1400 MPa and at temperature of 1150 °C and measured a plastic strain of $\approx 5\%$ under axial stress of 3300 MPa [36]. In order to accommodate polycrystal deformation based on Von Mises criterion, the pyramidal slip systems should be activated. However according to Korinek *et al.* [37], no clear evidence of pyramidal slip has been obtained so far, and prism plane slip and rhombohedral twinning with additional basal slip mainly account for the plastic deformation in the polycrystalline α -Al₂O₃ under hydrostatic pressure.

A compelling evidence for the Griffiths theorem that fracture needs to be an energy releasing process are the mechanical tests done to brittle materials under the confinement of a high hydrostatic pressure by several authors on Al₂O₃ introduced above. In the ideal case with an infinitely rigid hydrostatic pressure medium, the medium would not penetrate into the surface flaws and therefore the tensile stress needs to be at least equal to the hydrostatic pressure in order induce a fracture from surface flaws. As the real medium transmitting the pressure is not ideally rigid material such as a polymer or metal sheet the fracture begins lower than the ideal fracture stress. That is because at some pressure the sheet deforms, penetrates the cavities and works to increase the stored elastic energy, which is released upon fracture. Large variation in tensile strength as a function of pressure medium rigidity also underlines the dominating effect of surface flaws in fracture of brittle materials [32].

Amorphous and the numerous metastable transitions phases (γ , η , δ , δ^* , κ , θ and σ) of Al₂O₃ are somewhat less studied and very little are known of their dynamic mechanical properties. This is partly due to the difficulty of producing dense bulk samples of these phases. Reason for this is two-folded: First, the high temperature needed to fully densify aluminium oxide produced by powder processing route always leads to the most stable phase of α -Al₂O₃ [38]. Secondly, if a melted bulk

Al_2O_3 is rapidly quenched, it leads to intensive cracking by the cooling stress gradients (again in the absence of plastic relaxation) and probably therefore has not been considered much for mechanical studies. Other techniques such as plastic deformation induced recrystallization, familiar in metals processing, cannot be considered as three-dimensional plastic deformation of polycrystalline phases are blocked up to an ultra-high temperature.

By looking at different manufacturing methods for bulk ceramics, it is evident that the most effective processing route is the powder-processing route, which when full densification is allowed, exclusively leads to polycrystalline and brittle $\alpha\text{-Al}_2\text{O}_3$. Transition phases become important only when we study mechanical properties of extremely small structures also called nanostructures, which are discussed later in detail.

1.4 Diffusion based plastic deformation of aluminium oxide

Besides dislocation glide, the other relevant and well-studied plastic deformation mechanisms for ceramic materials are the time-dependant, diffusion based mechanisms such as creep and viscous flow.

In thermally activated diffusion or self-diffusion, an ion/atom or a molecule jumps to a next location when it reaches a critical activation energy to squeeze between its neighbouring ions/atoms/molecules [39]. This vacancy mediated diffusion is known to be the most important diffusion mechanism in metals [39] and most likely for ionic/covalent solids as well [1]. Location of the jump is typically a vacant nearest neighbour site, although some alloys can exhibit also double jumps [39]. **Figure 1.6** illustrates the energy needed for a jumping atom to perform a single diffusion step in to a vacant space. In a single crystal, the single step length and energy needed for a single step are well defined, but for example in steps across the grain boundaries and especially in amorphous material, the jump length and energy can vary in each step leading to uncertainties in quantifying these processes. The general flux [$\text{mol}/\text{m}^2\text{s}$] of ions through a solid is given as

$$F_{\text{ion}} = \frac{c_{\text{ion}} D_{\text{ion}}}{k_B T} Q \quad , \quad (1.5)$$

where, c_{ion} [$\text{N}_{\text{ions}}/\text{m}^3$] is the total concentration of ions (or atoms) diffusing through the solid, D_{ion} [m^2/s] is diffusivity of these ions, Q [J] is the driving energy for

diffusion per ion, k_B [J/K] is the Boltzmann constant and T [K] is the temperature [1]. The important notion regarding the ion flux is that always

$$c_{\text{ion}}D_{\text{ion}} = c_{\text{vac}}D_{\text{vac}} , \quad (1.6)$$

where c_{vac} is the total concentration of vacancies diffusing through the solid and D_{vac} is the diffusivity of vacancies, meaning that there is an equal flux of vacancies in opposite direction to flux of ions during diffusion [1]. It is necessary to understand that determining the numerical value of c_{ion} actually requires the measure of vacancy concentration.

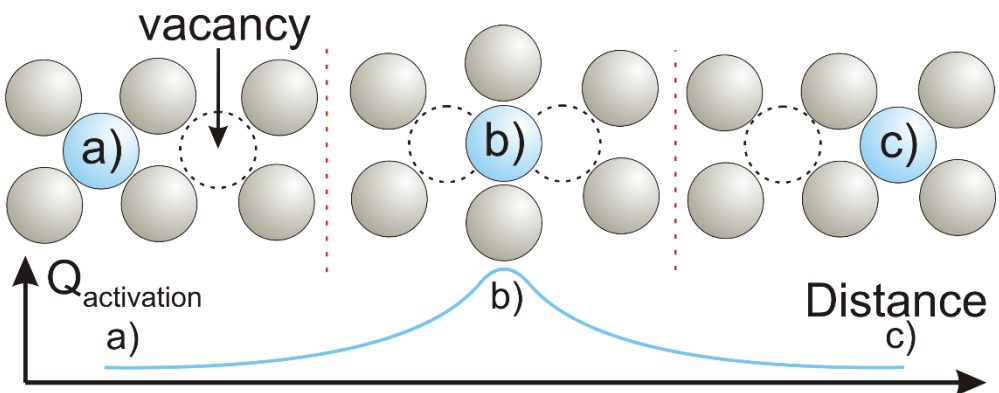


Figure 1.6: Vacancy mediated diffusion of ions or atoms in a single crystal lattice. Vacancy diffusion happens in the opposite direction to atom diffusion. Activation energy $Q_{\text{activation}}$ obtains a peak value at a critical distance b) from the low energy positions a) and c). Copyright Erkkä J. Frankberg 2017

The energy needed to induce a diffusion step can be seen analogue to the energy needed to induce a single dislocation step with Peierls-Nabarro lattice friction, although not necessary equal. The main difference to slipping is that diffusion is inherently a random process governed by available thermal energy in a solid [39], although external forces can enhance diffusion. Additional generalization could be made that all atom movement in a solid is diffusion based and governed by internal and external activation energy, but for slip, the steps are equal in length and magnitude given by the Burgers vector and happen along a well-defined low-energy diffusion path.

Vacancies are the most simple crystal point defects and they are key constituent determining diffusion and electronic properties of ceramics. Vacancy is simply an empty space, which normally would be inhabited by an ion (or atom).

Thermodynamic equilibrium requires that vacancies exist in all crystals at all temperatures [1, 18, 40]. A general Arrhenius model of vacancy concentration in a material is given as:

$$N_v = N e^{(-Q_v/k_B T)} , \quad (1.7)$$

where N_v is the concentration of vacancies, Q_v [J] is the activation energy needed for creating a single vacancy, k_B [J/K] is the Boltzmann constant, T [K] is the absolute temperature and N is the concentration of atomic sites

$$N = \rho N_A / M , \quad (1.8)$$

where ρ [g/m³] is density, N_A is Avogadro constant and M [g/mol] is molar mass.

The driving force for diffusion can be intrinsic e.g. concentration difference across the solid or external such as stress gradient, temperature gradient or electric field gradient across the solid [39]. **Table 1.2** summarizes the different external driving forces for diffusion. Regarding plastic deformation, the most interesting external driving force is the stress gradient that can generate a directed drift motion of atoms in addition to random motion [39].

Analogously to the lattice friction of ceramics, the activation energy needed to make a single atom step by diffusion is high compared to metals and polymers. The complexity of ceramic lattice and the ionic/covalent nature of bonding limit the movement of atoms by diffusion and increases the energy required to initiate diffusion. Important point is that also dislocations can move by diffusion under a constant or cyclic load. For ceramics the dislocation movement is again hindered by details discussed earlier and typically creep happens only at high temperature.

Table 1.2: Examples of external driving forces leading to directed drift motion of ions or atoms. Nabla (∇) expresses the 3-dimensional vector of the gradient driving force. [39]

Driving force	Expression	Remarks
Stress gradient	$-\nabla U_{el}$	U_{el} elastic interaction energy due to stress field
Temperature gradient	$-S/\nabla T$	S is the Soret Coefficient
Gradient of electrical potential	$-\nabla U$	U is the electrical potential energy
Gradient of chemical potential	$-\nabla \mu$	μ is the chemical potential

Oxides such as aluminium oxide are partly ionic compounds, which means they maintain a charge balance inside their structure. Charge balance is met in Al_2O_3 by combining two Al^{+3} ions with three O^{-2} ions. This requires special conditions for diffusion, as the charge balance has to be maintained also after every diffusion step. If the stoichiometry of the material is maintained, Stoichiometric defects form, which are called either Schottky or Frenkel defects. In a Schottky defect, vacancy pairs maintain the charge balance. For Al_2O_3 the simplest way to form a charge balance in Schottky defect would be to substitute two Al^{+3} ions with vacancies and three O^{-2} ions with vacancies summing up to five vacancies in total. In a Frenkel defect, an ion migrates into an interstitial atom site forming a vacancy in the original location. **Figure 1.7** illustrates Schottky and Frenkel defects for a simple cubic crystal of sodium chloride. Non-stoichiometric defects are also possible in ceramics. This often requires that the defects themselves hold an electric charge to maintain the charge balance, which is not possible in metals [18].

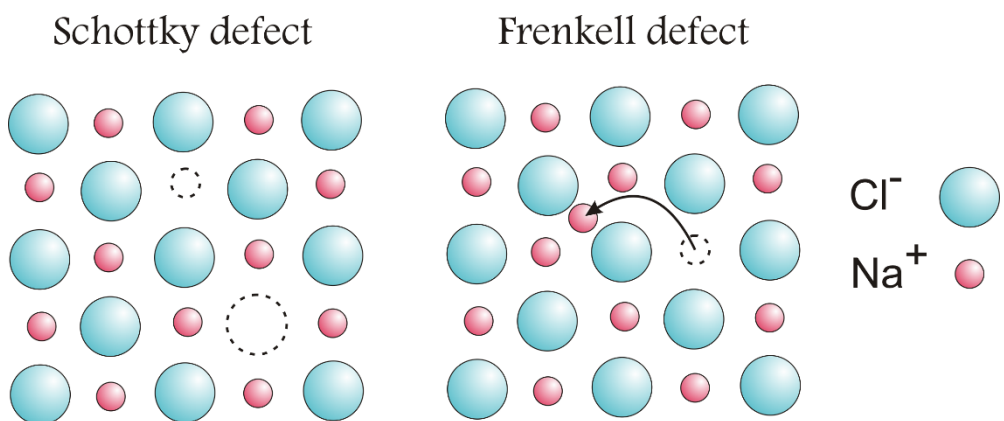


Figure 1.7: Illustration of Schottky and Frenkel defects in sodium chloride, simple ionic and cubic crystal with a chemical formula NaCl. Adapted from Barsoum [1], copyright Erkka J. Frankberg 2017

For Al_2O_3 it has been proposed that numerically the formation energy for stoichiometric defects is in order of Schottky < Al^{+3} Frenkel < O^{-2} Frenkel, which is in line with experimental observations [41]. The oxygen vacancy parameters have been shown to be similar in single crystal $\alpha\text{-Al}_2\text{O}_3$ and atomic layer deposition grown amorphous Al_2O_3 [42]. Experimental studies also indicate short-lifetime aluminium ion mediated Frenkel type defects in $\alpha\text{-Al}_2\text{O}_3$ [43]. Recently it has been proposed that nonstoichiometric oxygen vacancies and oxygen interstitial do not exist in amorphous Al_2O_3 [44]. The individual O^{-2} vacancies are compensated by the

amorphous structure in a manner that the electronic properties do not differ from that of the pristine material. Excess oxygen induces holes in the structure but are bound to the amorphous matrix by peroxide linking [44, 45].

Generally, thermally activated diffusion in ceramics is slow and requires high activation energy. The diffusion typically advances through the lowest energy path. The general relationship of diffusivity between different diffusion paths can be described as $D_L < D_p < D_{gb} < D_s$, where D_L is lattice diffusivity, D_p pipe diffusivity, D_{gb} is grain boundary diffusivity and D_s is free surface diffusivity [39].

Table 1.3: Averaged oxygen diffusion activation energy Q and averaged diffusion coefficient D_0 of different crystal structures/phases of Al_2O_3 . The temperature dependant diffusivity D can be calculated using Arrhenius-type equation $D = D_0 e^{(-Q/RT)}$.

Al_2O_3	Diffusion mechanism	Oxygen diffusivity D_0 [m^2/s]	Activation Energy Q [kJ/mol]
α – alpha [46]	Lattice (Undoped)	$3.8 \pm 120 * 10^{-3}$ (median \pm Std.dev.) ^a	595 ± 38 (median \pm Std.dev.)
	Pipe (= along dislocation line)	$2.7 \pm 1.9 * 10^{-2}$ (median \pm Std.dev.)	452 ± 13 (median \pm Std.dev.)
	Grain boundary (Undoped)	55 ± 127 (median \pm Std.dev.)	627 ± 230 (median \pm Std.dev.)
	Creep (Undoped)	0.48 (One value reported)	444 ± 30 (median \pm Std.dev.)
γ – gamma [47, 48]	Lattice (Undoped)	$1.7^{+75}_{-1.6} * 10^{-11}$ [47]	183 ± 58 (median \pm Std.dev.) [47]
Amorphous [47, 48]	Lattice (Undoped)	$8.6^{+56}_{-7.5} * 10^{-14}$ [47]	125 ± 19 [47]

^a Data by Reed & Wuensch and Oishi & Kingery (“extrinsic”) not included as deviate too much from consensus

Table 1.4: Aluminium diffusion activation energy Q and diffusivity D_0 of alpha Al_2O_3

Al_2O_3	Diffusion mechanism	Aluminium diffusivity D_0 [m^2/s]	Activation Energy Q [kJ/mol]
α – alpha [46]	Lattice (Undoped)	$25 \pm 25 * 10^3$ (median \pm Std.dev.)	382 ± 101 (median \pm Std.dev.)

Typically, the paths with higher disorder or smaller atom density require less energy for ions or atoms to take diffusion steps [39]. **Table 1.3** lists activation energy and diffusion coefficient D_0 of oxygen in different phases of Al_2O_3 and **Table 1.4**

aluminium activation energy and diffusion coefficient D_0 of α Al_2O_3 . The large scattering in the experimental data and lack of validated explanations for the scattering, together point out that we currently do not know very much about diffusion in Al_2O_3 [46]. The available data shows that oxygen diffusion activation energy seems to decrease when Al_2O_3 theoretical density decreases ($\rho_{\text{theor.}} = \alpha > \gamma > \text{amorphous}$). Literature values on aluminium lattice diffusion are confusing and more data is needed to understand the diffusion process.

1.5 Creep deformation of aluminium oxide

Based on the fundamentals of diffusion motion, creep is referred to be the time-dependant permanent deformation of single or polycrystalline material happening at a constant load, which is due to diffusion processes at high temperature [18]. In general, creep is a rather complex phenomena happening as a function of stress, time, temperature, grain size and shape, volume fraction and viscosity of glassy phases at the grain boundaries and dislocation mobility [1]. Notifiable creep requires a stress gradient in addition to thermal gradient, which dictates the general direction, or drift, of the diffusing atoms or ions. The shape change happens towards the applied stress as is logical. In a single crystal, creep can happen by diffusion of dislocations or diffusion of single atoms. Self-diffusion and creep are both diffusion based phenomena while the main difference is that creep (analogue also to sintering) rates for Al_2O_3 are determined by the slower ion, aluminium or oxygen, moving on its fastest path, e.g. through the lattice or along grain boundaries [46].

As simple “Fickian” presentation of diffusion as such is not suitable to describe creep, therefore creep diffusion through a crystal lattice is often called “Nabarro-Herring” creep. First Nabarro showed that in single crystals, vacancies can move from faces under tensile stress towards the faces under compression, leading to a permanent shape change [49]. Later Herring expanded this notion to include polycrystals [50]. Grain boundary diffusion is regarded as the preferred diffusion path at low temperature or when the grain size is small. Creep by grain boundary diffusion is called “Coble” creep [51]. Often both of these mechanisms are simultaneously active [18].

Figure 1.8 visualizes the vacancy-mediated diffusion by Nabarro-Herring and Coble creep. The figure is simplified as diffusion in ionic solids needs to consider also the cation/anion interaction and charge balance discussed earlier. Note that thermodynamically the volume under tensile stress has higher concentration of vacancies than volume under compressive stress [1].

For Nabarro-Herring creep, if we assume that stress vectors on surfaces under compression $-\sigma_{22}$ and under tension σ_{11} in **figure 1.8** $\sigma_{11} = -\sigma_{22}$, and if we assume that total work ΔW done in system equals the chemical potential of the system, then chemical potential $\Delta\mu = -2\sigma\Omega_{\text{ion}}$, where Ω_{ion} [$\text{m}^3_{\text{ions}}/\text{N}_{\text{ions}}$] is the atomic volume [1].

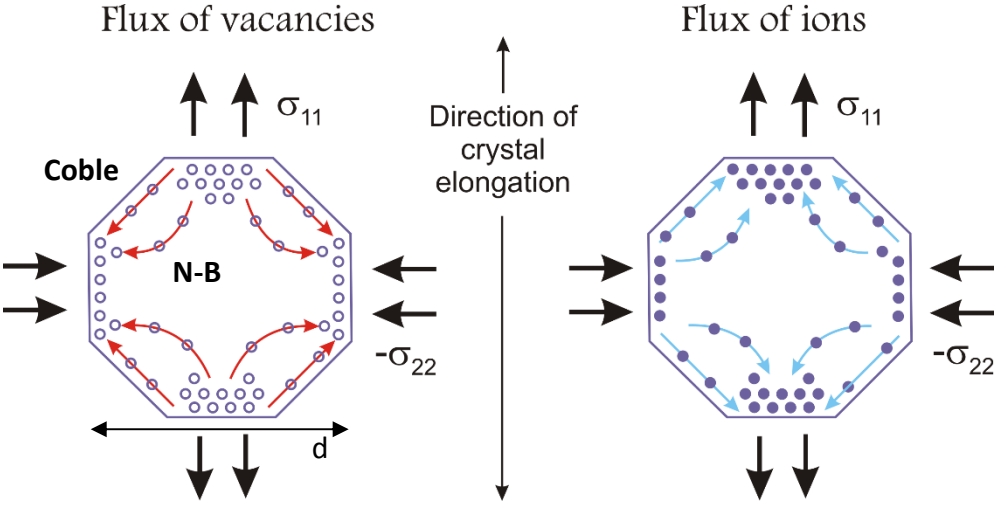


Figure 1.8: Diffusion of vacancies and ions in a single crystal with a diameter d [m] under tensile stress σ_{11} and compressive stress $-\sigma_{22}$, where $\sigma_{11} = -\sigma_{22}$. In Nabarro-Herring (N-B) model, diffusion happens through the crystal lattice and in Coble model through the grain boundary. Adapted from Barsoum [1], copyright Erkka J. Frankberg 2017

As average distance x between the two populations of vacancies is roughly $d/2$, then the driving energy becomes $Q = -d\mu/dx = 4\sigma\Omega_{\text{ion}}/d$. Using the **equation 1.5** the flux of atoms the becomes

$$F_{\text{ions}} = \frac{c_{\text{ion}} D_{\text{ion}}}{k_B T} \frac{4\sigma\Omega_{\text{ion}}}{d} \quad (1.9)$$

Then the total amount of transported ions through area A [m^2] which associated to the cross-sectional diameter of the crystal through which atoms are transported become

$$N = F_{\text{ion}} A t, \quad (1.10)$$

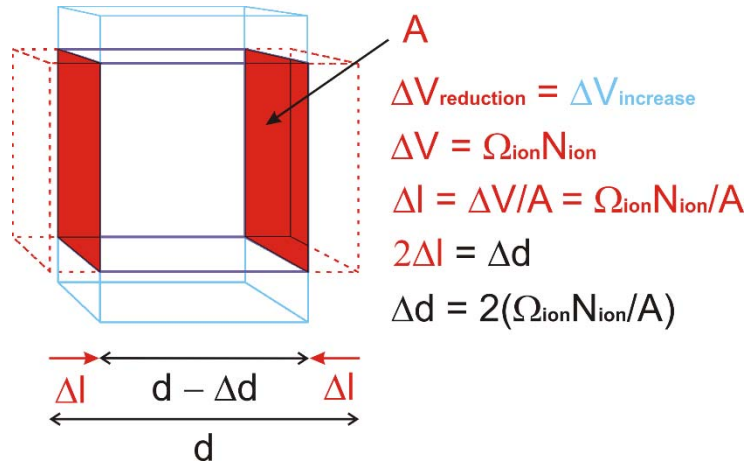


Figure 1.9: Change in diameter Δd of a cubic single crystal subjected to a uniform $\sigma_{11} = -\sigma_{22}$ stress during creep. Copyright Erkka J. Frankberg 2017

where t [s] is time. This will yield a change Δd [m] in the crystal diameter. **Figure 1.9** illustrates how diameter d of a cubic crystal changes during creep. Then we can write the full 2-dimensional strain ε caused by the volume of atoms as

$$\varepsilon = \frac{\Delta d}{d} = \frac{2(\Omega_{\text{ion}} N_{\text{ion}}/A)}{d} = \frac{2\Omega_{\text{ions}} F_{\text{ion}} t}{d} \quad (1.11)$$

Now we can combine the **equations 1.9** and **1.11** to yield a strain as a function of time, temperature and crystal diameter

$$\varepsilon(t, T, d) = \frac{8\Omega_{\text{ion}}^2 c_{\text{ion}} D_{\text{ion}} \sigma t}{k_B T d^2} \quad (1.12)$$

Now if we notice that $\Omega_{\text{ion}} c_{\text{ion}} [\text{N}/\text{m}^3 \cdot \text{m}^3/\text{N}] = 1$ and divide strain with time t , we get the respective critical creep strain rate

$$\dot{\varepsilon} = \frac{8\Omega_{\text{ions}} D_{\text{ion}} \sigma}{k_B T d^2} \quad (1.13)$$

which is the maximum strain rate of plastic deformation by rate limited diffusion at a given temperature in the crystal. As Herring shows [49] the equation often needs

to be fitted using a suitable constant to accommodate for example grain sliding in polycrystals. Then the creep strain rate equation reduces into

$$\dot{\epsilon} = \frac{\omega \Omega_{\text{ions}} D_{\text{ion}} \sigma}{k_B T d^2} , \quad (1.14)$$

where ω [] is a dimensionless constant with a value of, for example, 13.3 under simple tension and steady state conditions [18]. Coble creep follows the exact same thought as Nabarro-Herring, but now we assume that all diffusion happens through the grain boundaries. Grain boundaries are believed to be a faster diffusion path at low temperatures or when the average grain diameter becomes very small [1, 18]. The Coble creep strain rate becomes

$$\dot{\epsilon} = \frac{\Psi \Omega_{\text{ions}} D_{\text{ion}} \delta_{\text{gb}} \sigma}{k_B T d^3} , \quad (1.15)$$

where Ψ [] is a dimensionless constant with approximate value of ≈ 45 [1, 18] and δ_{gb} [m] is the thickness of the grain boundary. We can see that Coble creep is more sensitive to grain size (d^3) compared to Nabarro-Herring creep. Related to both creep modes, It is worth noting that the diffusion constant D_{ion} changes according to the chosen diffusion path (Nabarro-Herring/Coble) and will be more complex in ionic materials as movement of different anions and cations need to be considered [52]. Also when selecting a diffusivity value D_{ion} , it is generally accepted that creep is rate controlled by the slowest specie moving through its fastest diffusion path [46].

The creep of single and polycrystalline $\alpha\text{-Al}_2\text{O}_3$ has been studied extensively by several authors [46, 53]. Creep can be initiated at around 900 °C at 75 MPa and initiation stress lowered uniformly to 13 MPa at 1400 °C [54]. Starting temperature 900 °C agrees well with a general notion that creep commences in ceramics at around half of the absolute melting temperature [1] which in case of Al_2O_3 is ≈ 2345 K or 2072 °C. Dislocation movement was imaged in single crystal $\alpha\text{-Al}_2\text{O}_3$ during creep and showed predominantly basal slip accompanied by rhombohedral twinning at temperatures from 1400 - 1700 °C [30]. Cannon *et al.* studied creep of polycrystalline $\alpha\text{-Al}_2\text{O}_3$, with a grain size of 1 - 15 μm and found that diffusional creep is the most important mechanism for creep with aluminium ions controlling the rate of diffusion as grain boundary diffusion of oxygen ions is fast compared to aluminium ions [55]. Assumption of aluminium acting as the rate controlling species in creep has been criticized later on [46]. Experimental indentation results show that

plastic deformation can be obtained in nanocrystalline ceramics with lower strain rates than given by the critical value of Coble creep and behaviour changes back to brittle with higher strain rates [7]. Doping of Al_2O_3 with yttrium [56, 57] has been found to slow down grain boundary diffusion and therefore increases creep resistance.

1.6 Viscous flow of oxide ceramics

Viscous flow describes another form of diffusion mediated plastic deformation of amorphous solids (or liquids). The typical notion is that a liquid can deform under its own gravity by viscous flow when sufficient heat is available. Sometimes creep of grain boundary glass phase is said to undergo “viscous creep” [1], but is really the same phenomena as viscous flow. Traditionally viscous flow is taken advantage in glass forming such as glass blowing (**Figure 1.10**), glass fiber and flat glass manufacturing.



Figure 1.10: Traditional glass blowing at Nuutajärvi Glass Village, Urjala, Finland. Copyright Nuutajärvi Glass Village est. 1793.

A solid amorphous material or a glass is not easily defined as a separate phase such as the crystalline phases. Reason is that there is no sharp decrease in volume and enthalpy during glass formation, which is the case when a crystal is formed from the amorphous phase. Amorphous material is created from melt or gas phase by fast under cooling to a temperature where the atoms cannot anymore go through a phase transformation into a crystal. Then the material is a solid with a liquid-like

structure and typically has very similar basic properties compared to a corresponding solid crystalline phase [39]. The transformation from liquid to undercooled solid is often marked by a glass transition temperature T_g under which a change happens in the thermal properties of the material, namely specific heat and thermal expansion coefficient [39]. Typically for amorphous/glass materials, they do not exhibit a clear melting temperature, but the viscosity of the material gradually decreases with increasing temperature beyond T_g . The glass transition temperature for amorphous Al_2O_3 has been estimated to be anywhere around 973 K to 2000 K [58, 59], of which 973 K is also the temperature where amorphous Al_2O_3 is thermally crystallized [60]. At room temperature all allotropes of Al_2O_3 are therefore considered solid materials.

Several different models to explain viscous flow have been proposed such as “Absolute rate” theory, “Free volume” theory and “Excess-Entropy” theory [18]. Basic notion is that there is enough thermal activation energy available that solid glass changes into a viscous fluid, which then deforms similarly to any fluid. For oxide glasses the flow behaviour at high temperature can be close to “Newtonian” [18] meaning that shear stress needed to stir the fluid glass and the shear rate (also referred to as strain rate or stirring speed) are linearly proportional and the strain rate for viscous flow can be written as

$$\dot{\gamma} = \tau/\eta \quad (1.16)$$

where η [$\text{Pa} \cdot \text{s}$] is the proportionality factor called “viscosity” of a fluid, τ [Pa] is the shear stress or the force over area subjected to the fluid and $\dot{\gamma}$ [$1/\text{s}$] is shear strain rate (sometimes rate of shear strain), or stirring speed, which is the first order derivative of the shear strain [1]. Viscosity of fluids changes with temperature, as in higher temperatures, ions have more driving energy to diffuse and therefore require a smaller external stress gradient to move.

If a glassy intergranular film (IGF) is formed in between the crystalline grains in a polycrystal, creep can proceed by grain boundary sliding at high temperature [1, 18]. Grain boundary sliding is a thermally activated creep process which governed by the viscosity of the glassy phase. The effective viscosity η_{eff} of a polycrystal undergoing grain boundary creep can be estimated for example as

$$\eta_{\text{eff}} = \frac{\xi \eta_0}{f^3} \quad (1.17)$$

where ξ [] is a dimensionless constant, η_0 [Ns/m²] is the bulk viscosity of the grain boundary phase and f [] is the volume fraction of grain boundary phase [1]. The corresponding creep strain rate at certain stress can then be obtained using **equation 1.16**. At high temperature, creep can also happen by dissolution-precipitation process, which is analogue to mechanisms of liquid state sintering [18].

Whether glass structures below T_g can viscously flow under their own gravity and at ambient temperatures is still under debate, although severe objections have been presented against it [61, 62, 63]. It is said that structure of glass and dynamics of glass transition temperature remains the deepest unsolved problem in solid-state physics [61, 64]. If we for example think about vacancy-mediated diffusion in amorphous materials, we encounter problems already in defining what a point defect (e.g. vacancy) means in an amorphous material. Moreover, the whole theory of vacancy-mediated diffusion is based on well-defined atom/ion steps with well-defined energy over a homogenous crystal. In amorphous structure, each diffusion step will have a different activation energy!

1.7 Shear banding and superplasticity

Shear banding is another deformation mechanism closely related to amorphous structures, especially metallic glasses [65]. Shear banding refers to a sudden pulse of shear induced plastic deformation, which often happens just before fracture of the amorphous material. The shear deformation is localized on a thin band, which visually resembles shear slipping of single crystals. This mechanism has been mostly attributed to amorphous metals but can happen in various solid materials and even liquids [65]. It has been thought to be the main cause of fracture in amorphous metals or “metallic glasses” and dynamics of shear banding has been extensively studied experimentally and by computational methods over the recent years [65, 66]. The shear banding effect is very dynamic and difficult to predict and the available critical strain rate is not as clearly defined as in the case of creep and viscous flow.

Superplasticity is yet another special deformation mechanism for polycrystalline and amorphous materials, closely related to creep and viscous flow. Phenomena is found both in ceramics and in metals, for example in polycrystalline ZrO₂ [67] and needs moderately high temperature to occur, just as creep and viscous flow usually do. The reason why creep and viscous flow are so closely related is that the superplastic deformation is mediated by the disordered grain boundaries in which deformation is likely diffusion based. It is also most likely a rate limited process as

strain rate needs to be fitted inside a narrow window [67]. In fact, the biggest difference to normal creep is that superplasticity refers elongation of the sample from several hundred to even up to 1000 percent [18, 68]. One reason why superplasticity is separated from creep and viscous flow is that superplasticity has a set boundary conditions that need to be met in order it to happen. For example the grains need to be sphere symmetrical in diameter and the size distribution of the grains need to be small [18]. It is though that the main mechanism in superplasticity is a process called grain sliding [18, 68], which can be seen as analogue to viscous creep by grain boundary sliding discussed earlier. In grain sliding, the shape of the grains does not markedly change, but the grains switch places with each other allowing the bulk to undergo permanent plastic deformation. Drawback is that grain sliding is accompanied with extensive formation of cavities [18, 67].

Viscous flow of amorphous solids as such can produce extremely large elongations for example in glass fiber drawing. Therefore, to avoid confusion, superplasticity term should be used only for crystalline materials. The mechanisms of superplasticity are discussed in detail elsewhere [68].

1.8 Size effects in plastic deformation of aluminium oxide

So far, we have covered all the relevant plastic deformation mechanisms for different phases (including amorphous) of aluminium oxide. Based on the theory and experimental results, the chances to induce plastic deformation at room temperature seem scarce. Yet the conditions of the aforementioned mechanisms are not constant, as when we reduce the size of the deforming solid (crystalline or amorphous) the boundary conditions for slip and diffusion dramatically change. Next, we will discuss the plastic deformation occurring in very small structures below 100 nanometers or 0.0000001 m.

Nanostructures of Al_2O_3 are typically either fully amorphous [69] or a composite of nanocrystals in amorphous matrix [9] or fully nanocrystalline [70]. Generally the faster cooling rate methods with plasma as precursor have predominantly amorphous structure and obtaining a fully polycrystalline structure requires a post heat treatment or a heated substrate during coating. Electron and ion beams can also be used to induce crystallization of amorphous Al_2O_3 films and particles [71, 72, 73]

Once fully amorphous Al_2O_3 is heat treated, the first transition phase, gamma aluminium oxide ($\gamma\text{-Al}_2\text{O}_3$), crystallizes at temperature around 500 - 700 °C [74, 75].

This relatively high formation temperature actually makes it rather stable and very common phase alongside with the only thermodynamically stable Al_2O_3 phase alpha (α), which typically crystallizes around 900 – 1100 °C from one of the transition phases [26]. In amorphous films made by magnetron sputtering or pulsed laser deposition, small nanocrystals (1-10 nm) of γ -phase are known to form when coating is done at elevated substrate temperature [9, 76]. Even with partial crystallization, the films remain mostly amorphous; therefore, the film is an amorphous/crystalline phase composite.

As the structures are very small, also the flaws present in the structure become much smaller than in a typical macroscopic bulk. According to Griffith criterion, this allows much higher ultimate stress to be achieved which is experimentally shown for example using thin ceramic fibers. Additionally the diffusion length (e.g. crystal diameter) becomes very small allowing significant creep strain rates already at relatively low temperature. Therefore, the deformation mechanism can change allowing plastic deformation to occur even near room temperature [7].

First, let us consider mechanical properties of single crystals, e.g. small particles or “nanoparticles”. As earlier was discussed the macroscopic crystalline phases of Al_2O_3 are not considered to be able of plastic deformation at room temperature and at ambient confining pressure. The reason was that even the lowest energy slip could not be activated.

“Grinding limit” of materials is a well-known and practical experimental value that gives hints how size reduction affects the mechanical properties of particles [77]. Grinding refers to producing fine powders from coarse powder by milling e.g. fracturing larger particles in to smaller fractions. The small particle size in powder has many benefits in powder-based manufacturing and therefore the powder size has been pushed down towards nanometer range during the last decades [78]. As it turns out, there seems to be a limit of how small particles can be made by milling for a given material.

Karagedov *et al.* demonstrated grinding of coarse α - Al_2O_3 into ultrafine powder, which depending on the grinding additives and grinding media, produced a minimum crystallite size of 16 – 66 nm and “that a further increase in the duration of mechanical treatment will not lead to a further decrease of the size of the particles and crystallites” [79]. Knieke *et al.* further studied grinding limit of α - Al_2O_3 leading to a very similar grinding limit below 20 nm crystal size [80]. The mechanism behind the grinding limit was under debate, when in 2012, Calvié *et al.* gave a possible explanation for the grinding limit. They showed that transition alumina

consisting of δ (delta) and γ (gamma) phase nanoparticles under a critical size < 40 nm could not be fractured in real time compression tests done in transmission electron microscope, suggesting that at this size range particles deformed plastically without fracture even at room temperature [8, 81].

The results of Calvié *et al.* can be considered, if not a breakthrough, then a stepping-stone for a possible breakthrough in understanding plasticity of ceramics. The results seem to contradict the theory introducing brittle behaviour of ceramics, as the measurements were performed near room temperature and with no confining hydrostatic pressure.

These results push the theoretical boundaries of ceramics mechanical ductility towards comparable levels with metals. Individual nanoparticles are relatively uninteresting regarding engineering, since they lack the capability to be a significant structure! Therefore, we must ask whether the plasticity can be transferred into continuous 2D and 3D structures (perhaps made of nanoparticles), namely thin films or bulk nanostructures.

As Al_2O_3 nanoparticles, also thin films of Al_2O_3 have shown considerable potential for plastic deformation. Garcia *et al.* showed that relatively thick ($\approx 1 \mu\text{m}$) amorphous and polycrystalline composite Al_2O_3 thin films deformed plastically without any sign of cracking during nanoindentation experiments [9]. Most recently, Esmaeily *et al.* showed plastic deformation capability of amorphous Al_2O_3 nanofibers [82]. Viscous flow or creep of nanostructures near room temperature have also been demonstrated with amorphous SiO_2 [11, 83] and nanocrystalline TiO_2 [7] and from pure metals side for example in nanocrystal Ag [84]. In the case of SiO_2 the main reason enabling plastic deformation was attributed to be the effect of the energetic electron beam in transmission electron microscope [11, 83].

Few molecular dynamic simulation studies exist regarding mechanical properties of aluminium oxide. Interaction potentials for Al_2O_3 have been developed at least by Matsui [85, 86] and by Blonski & Garofalini [87]. Sarobol *et al.* [88] simulated 10 nm alpha Al_2O_3 particles in compression and found out that significant plastic strain can be accumulated, although fracture eventually happens. When they used 10 nm bicrystals with a grain boundary, fracture happened with less plastic strain and they conclude that the pre-existing defects play a key role in plasticity. Next, we will introduce the experimental methods used to study the plastic deformation of amorphous aluminium oxide thin films.

2. Methods and materials

The methods used in the study are divided into experimental and theoretical methods. As a summary, we tested the mechanical properties of Al_2O_3 thin films experimentally *in situ* in transmission electron microscope and the obtained experimental results were challenged with molecular dynamic simulations using the LAMMPS simulator code with a classical force field. Other methods are used to support and verify the obtained results.

We conducted the experimental work in collaboration with several different European research entities: Deposition of test samples were done at the Italian Institute of Technology (IIT) located in Milan, Italy and some additional samples were made at Picodeon Oy located in Ii, Finland. Characterization of samples was done at Institute National des Sciences Appliquées de Lyon (INSA Lyon) and at Tampere University of Technology (TUT), Finland. Mechanical testing setup was jointly build in INSA Lyon and TUT and the mechanical tests were carried out at INSA Lyon during 2016-2017. Theoretical methods were carried out at TUT and additional atomic force microscopy (AFM) measurements were performed at Erich Schmid Institute of Materials Science located in Leoben, Austria.

2.1 Thin film deposition

We deposited all samples using the pulsed laser deposition (PLD) method. In pulsed laser deposition, a short laser pulse or pulses interacts with a target material surface causing an ablation phenomena. In ablation, intense energy absorption turns a thin layer of target material into plasma of charged ions. As the plasma expands in the vacuum or background gas in the chamber, the nucleation and growth of crystals is rapidly quenched. PLD's advantage is the ability to preserve the stoichiometry and the chemical structure of the PLD target material in to the film [78, 89]. Due to high quenching rate, the as-deposited material is often amorphous [9, 89]. **Figure 2.1** shows a schematic presentation of a typical PLD setup.

Pulsed laser deposition of Al_2O_3 thin films was done on various substrates including sapphire ($\alpha\text{-Al}_2\text{O}_3$), silicon (Si) and sodium chloride (NaCl) using PLD coating equipment at the Nano2Energy Laboratory at Italian Institute of Technology (IIT) and the Coldab™ PLD coating system at Picodeon Oy Ltd. Finland. The samples were shipped to the test location in France as a normal protected package via international shipping. Samples were stored at room temperature and normal

atmosphere. The **table 2.1** lists all the available parameters used in the deposition processes. Parameters capable of producing fully dense films were chosen for the deposition [9].

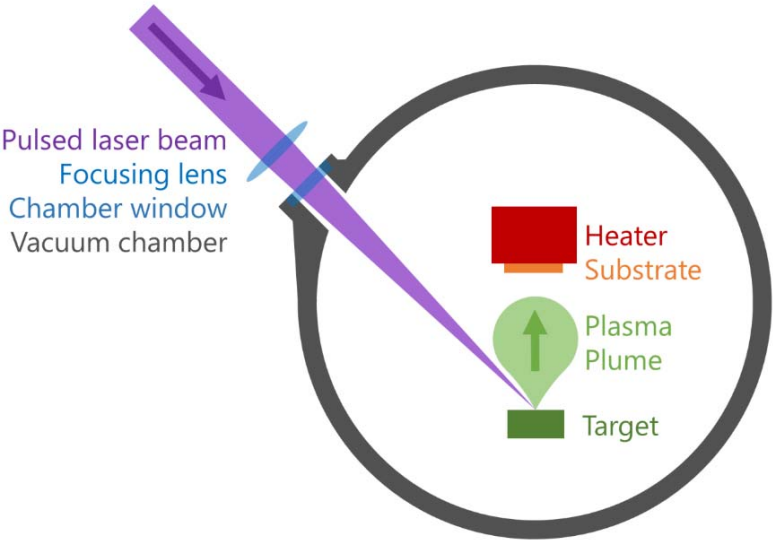


Figure 2.1: Schematic presentation of the pulsed laser deposition (PLD) process. Copyright Creative Commons CC0 1.0 Universal Public Domain Dedication

Table 2.1: List of PLD deposition parameters and samples produced

	Nano2Energy laboratory - IIT	Picodeon Oy
Target material	99.99 % pure, α - Al_2O_3	99.7 % pure, α - Al_2O_3
Distance to target	5 cm	-
Laser incidence angle to target	40°	
Temperature	Room temperature (RT)	-
Laser wavelength	248 nm	-
Laser fluency	3.5 J/cm ²	0.05 J/cm ²
Pulse duration	Picosecond laser	Picosecond laser
Repetition rate	20 Hz	-
Vacuum level	-	5.0 x 10 ⁻⁶ mbar
Oxygen back pressure	1.0 x 10 ⁻³ mbar	-
Substrate materials	NaCl, Sapphire	Silicon wafer
Samples produced	IIT1, IIT2 and IIT3	S1126
Nominal film thickness	20 – 50 nm	80 nm

Films coated on NaCl, α -Al₂O₃ and silicon substrates were used for characterization purposes and films on NaCl and α -Al₂O₃ were used for mechanical testing. Nominal thickness of the coatings was determined by deposition time using a nominal nm/s deposition rate. In samples coated by IIT, the substrate was kept stationary during deposition; however, as the used substrate size was small, $\leq 5 \times 5$ mm, the thickness variation is considered negligible. In the silicon wafer coated by Picodeon, the thickness variation was kept at minimum by optimally moving the substrate while scanning the laser on the target.

2.2 TEM characterization sample preparation

In addition to mechanical characterization, also a thorough TEM characterization was done to all samples. TEM characterization samples were prepared using several methods including focused ion-beam (FIB) lift-out method, abrading the sample surface, NaCl floating method and by direct deposition on an electron transparent sapphire edge. Next, we will introduce all the used methodology.

Direct deposition of samples was done on an edge of a single crystal α -Al₂O₃, which was thinned down to electron transparency using the AbeaM method introduced in the next chapter. A PLD Al₂O₃ film was deposited directly on the thinned edge at Italian institute of Technology with a nominal thickness of 50 nm. The sample was viewed in TEM on top of the sapphire thin edge without any further manipulation.

NaCl floating technique was utilized using cleaved 5 x 5 x 5 mm sodium chloride crystals with (100) crystal orientation. The PLD film was deposited on a freshly cleaved surface. After deposition, the film was removed from the NaCl substrate by slowly dipping the substrate into ion-exchanged water, and the self-standing film was left floating on the water surface. Next, the water level is lowered to allow the PLD film to float on a copper TEM grid with amorphous holey carbon coating. Finally, the TEM grid with the film was rinsed in ion-exchanged water to remove any traces of sodium chloride and dried at room temperature for several days prior to imaging in TEM. **Figure 2.2** shows a cleaved NaCl crystal and a floated PLD Al₂O₃ film freshly deposited on a copper TEM grid.

FIB lift-out sample was milled using a Zeiss Supra 55VP with a gallium ion source (Carl Zeiss Microscopy GmbH). A PLD Al₂O₃ film deposited by Picodeon Oy on a silicon wafer was selected to be prepared. The FIB lift-out technique is comprehensively introduced elsewhere [90].

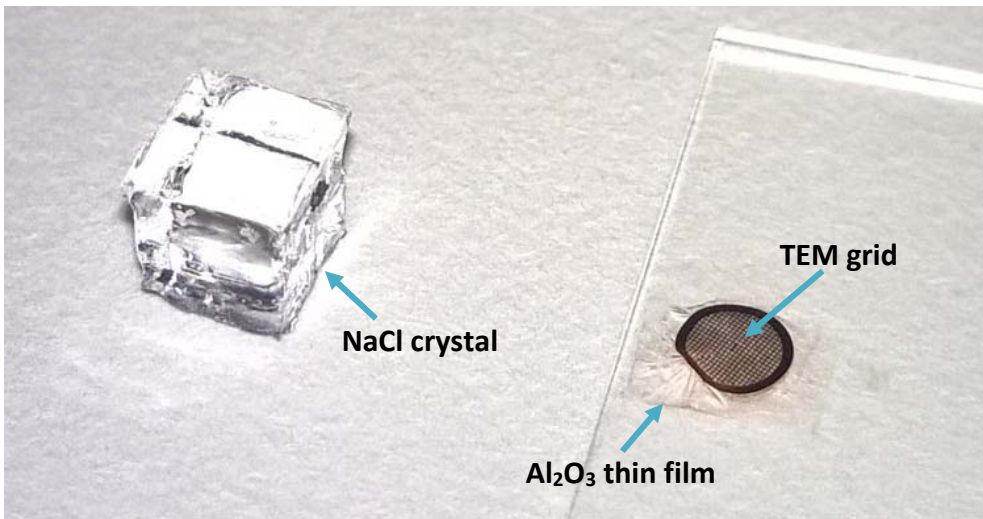


Figure 2.2: (Left) a cleaved NaCl crystal and (Right) freshly deposited PLD Al₂O₃ film on a copper TEM grid transported using the floating technique. Copyright Erkka J. Frankberg 2016

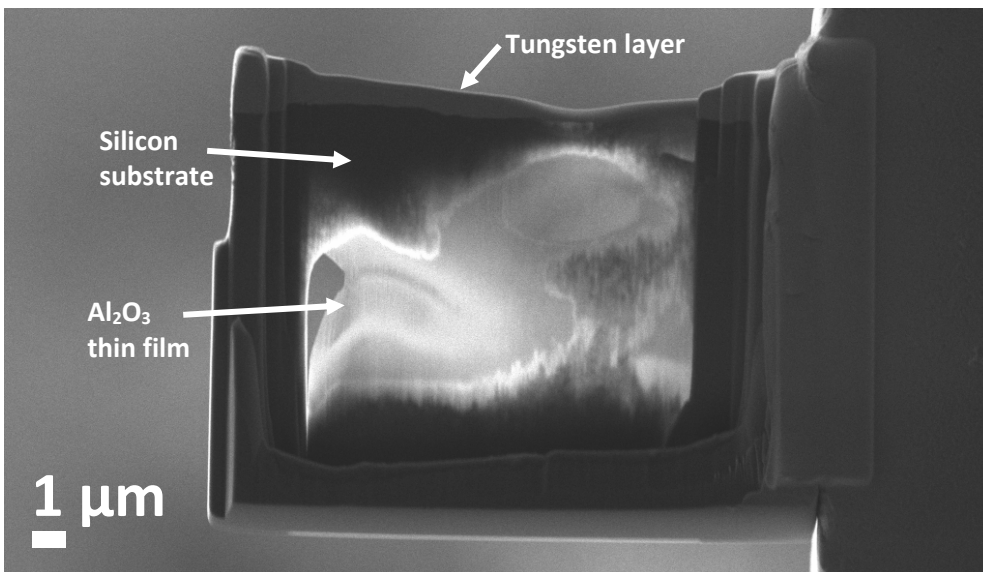


Figure 2.3: Scanning electron microscope image of the FIB lift-out sample after final thinning, lighter contrast shows the areas of the sample that were thin enough to be imaged in TEM. Copyright Thierry Douillard / Erkka J. Frankberg 2016

Shortly, our FIB lift-out procedure consisted of several steps: First, a film of gold was sputtered on the whole PLD Al_2O_3 film surface for protection. A trench was milled and then next a protective layer of tungsten (W) was deposited on the cross-section of the film by gas injection system (GIS) for further protection during milling. Roughly a 1 μm thick piece was removed by lift-out where a micromanipulator is attached to the work piece by gas injection system and then cut free using FIB. The piece was then transported and attached with GIS on a TEM sample holder. Finally thinning of the sample was done attached to the TEM sample holder. **Figure 2.3.** shows the FIB lift-out sample after final thinning.

Lastly, TEM sample from the film coated by Picodeon Oy was fabricated by abrading the film surface using a P4000 abrasive paper in ethanol. Once abraded, few drops of the ethanol with abrasion residuals was dropped onto a copper TEM grid with amorphous holey carbon coating and left to dry at room temperature before imaging in TEM.

2.3 TEM characterization

The deposited thin films were characterized to determine the as-deposited microstructure of the films, measure the film thickness, determine their stability under electron beam conditions and to confirm the chemical composition of the films. In addition, the produced nanomechanical testing tools were studied using TEM and TEM tomography to determine the dimensions of the tools and the electron transparency of the tools.

Transmission electron microscopy was the main tool to characterize all materials. Different equipment used for the studies for each sample is given in **table 2.2**:

Table 2.2: List of equipment used for transmission electron microscopy characterization

	Electron source	Acceleration voltage	Used imaging modes	Study of samples deposited on
Jeol JEM 2010	LaB ₆	200 kV	TEM	Silicon
Jeol F2010	FEG	200 kV	TEM, STEM	NaCl, Sapphire, Silicon
FEI Titan ETEM, Aberration corrected	FEG	300 kV	TEM, STEM	NaCl, Sapphire

Electron dispersive spectroscopy (EDS) with and without scanning mode (HAADF-STEM) was used to study the elemental composition of the samples and electron diffraction was used to study the crystallinity of the samples.

Electron tomography was performed on the ABeaM and FIB milled mechanical testing tools prior to film deposition on the tools in transmission electron microscope. First few drops of dilute gold colloid was pipetted on top of the anvil, dried and then cleaned in a plasma cleaner for 20 s. The tilting series was done at 300 kV in scanning transmission electron microscopy (STEM) mode from -60° to $+60^\circ$ with image taken every 2° . The reconstruction of the 3D image was done based on ART algorithm and image treatment with Image J software using IMOD package and .DM3 format in digital micrograph software.

Scanning electron microscopy (SEM) was also used as a supplementary characterization and imaging method with Zeiss Crossbeam 540 and Zeiss Supra 55VP scanning electron microscopes.

2.4 Tools development for *in situ* TEM mechanical testing

Special anvil tools were developed for the compressive/shear testing of the PLD Al_2O_3 films. The tools were milled on a single crystal sapphire ($\alpha\text{-Al}_2\text{O}_3$) 2 x 2 mm rectangles with a thickness of 75 μm (Optics Concept SAS). The rectangles had been polished for optical transparency from both sides, with an approximate R-plane ($1\bar{1}02$) crystal orientation. A new dual ion milling technique was developed, which utilizes Angled Broad ion beam Milling (ABeaM) combined with focused ion beam (FIB) milling.

In ABeaM, a conventional broad ion beam (BIB) mill can be used; here we used Ilion II (Gatan Inc.). In broad ion beam milling, the milled sample is protected by an alloy blade to localize the milling and to produce a flat milled area parallel to the Ar^+ ion beam.

In ABeaM, the sample is tilted (roughly $70 - 80^\circ$) in respect to the alloy mask so that a sharp edge of $20 - 30^\circ$ is formed on the sample. The beam exposed sample height was kept below 150 μm . **Figure 2.4** illustrated the sample and mask geometry used in ABeaM. Each sapphire substrate was milled for 4 – 6 hours without active cooling, starting from room temperature and using a 6 keV beam energy.

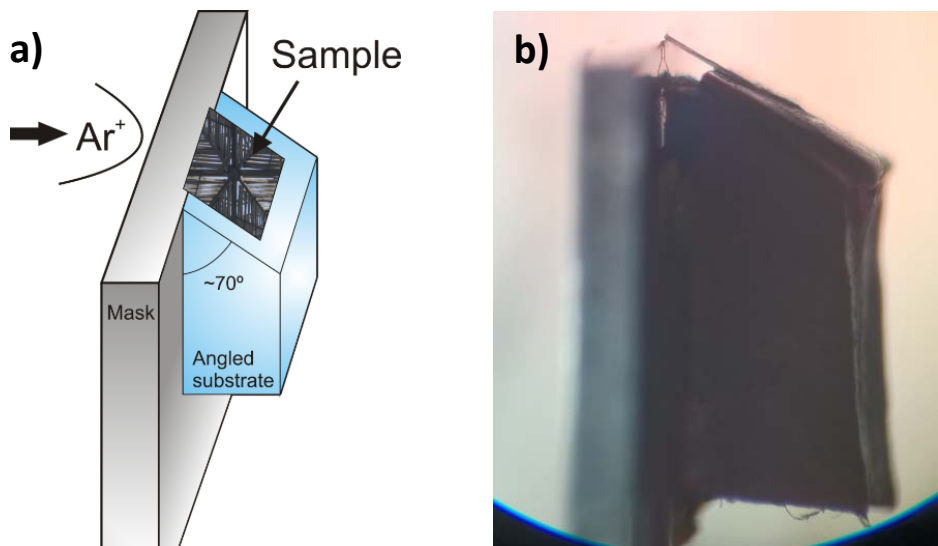


Figure 2.4: a) schematics of the sample orientation in respect to the Ar⁺ ion beam and to the alloy mask and b) an optical stereomicroscope side-view of the milling setup with a mounted, 75 μm thick, sapphire rectangle. Copyright Erkka J. Frankberg 2016

The produced thin section is further milled using focused ion beam to produce sapphire anvils on which a PLD Al₂O₃ film can be deposited. **Figure 2.5** illustrates the geometry of the anvil tools for compression and shear testing of thin films.

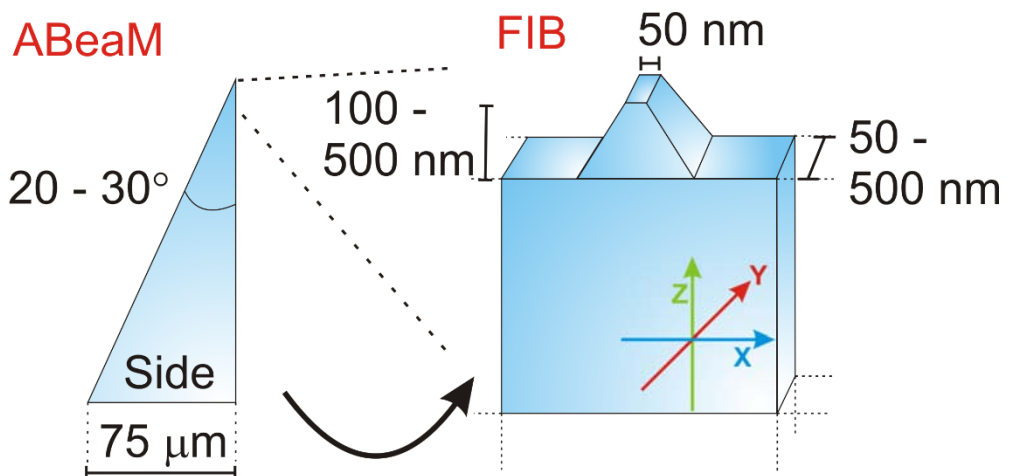


Figure 2.5: Schematic presentation of a sapphire anvil tool to be used for *in situ* mechanical testing of thin films in TEM. Copyright Erkka J. Frankberg 2017

The FIB in use was a Zeiss Crossbeam 540 with a gallium ion source (Carl Zeiss Microscopy GmbH). SEM inspection of the samples was performed with the same device. The FIB procedure consisted of rough milling of the shape with 30 kV acceleration voltage and 50 pA current. A second step with 10 pA current was added to allow finer adjustment of the anvil size as the ion beam spot dimensions depend on the current. Finally, a 2 kV acceleration voltage and 15 pA treatment was added to reduce the amorphous layer that is likely to form due to the damage by the energetic gallium ions.

2.5 *In situ* TEM mechanical test sample preparation

For compression/shear tests, a PLD Al_2O_3 film was deposited directly on the anvil tools milled into the edge of a single crystal sapphire described earlier. Deposition was done in Italian institute of Technology on two sapphire crystals IIT2 and IIT3 with a nominal thickness of 40 and 20 nm respectively. In total 76 anvil tools were coated and the suitable ones were chosen for test samples. Direct deposition was chosen because the sample is not manipulated in anyway (ions, mechanical etc.) before the mechanical testing, retaining the as-deposited structure and properties.

For tensile tests, a PLD Al_2O_3 films with a nominal thickness of 50 nm deposited on NaCl crystals were transferred using the floating technique on top of a special push-to-pull (PTP) devices fabricated on a piece of a silicon wafer. **Figure 2.6** shows an optical microscope image of the push-to-pull device.

Push-to-pull devices had a nominal 150 N/m stiffness and were manufactured by Hysitron Inc. Floating covers the device fully with the film and the device is then cleaned using FIB in a manner that only a small tensile specimen of approximately 500 nm in width is left attached between the stationary edge and moving edge of the device. The film was attached to the silicon from both sides with platinum using the FIB gas injection system. **Figure 2.7** shows an example of the film-coated push-to-pull device ready for mechanical testing.

Three tensile test samples were successfully prepared using the described strategy. In tensile tests, the amount of samples is more limited as only one sample can be placed on one push-to-pull device.

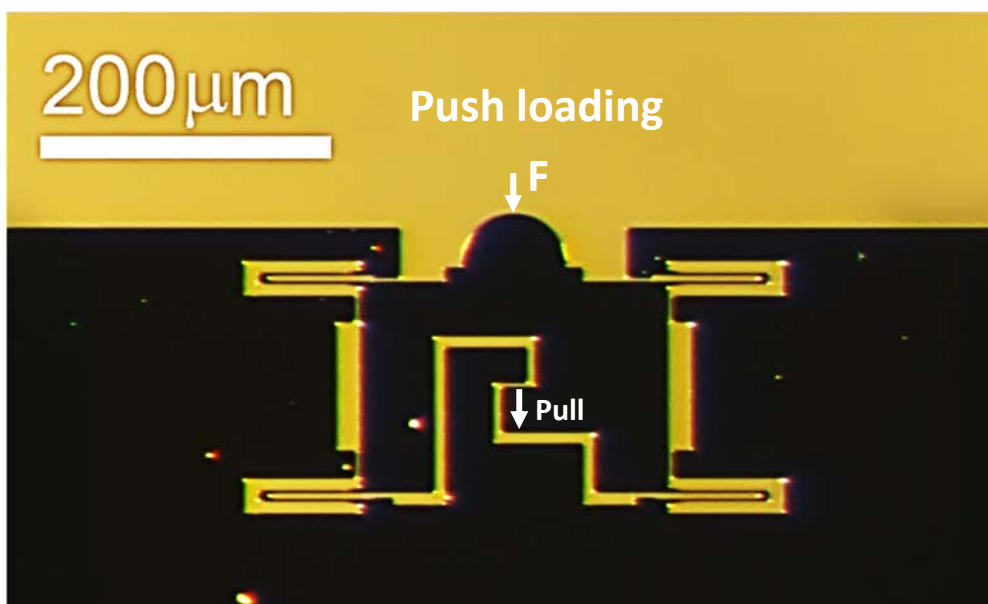


Figure 2.6: Optical microscope image of a silicon push-to-pull device with nominal spring constant of 150 N/m, which we used to perform tensile tests on PLD Al_2O_3 *in situ* in transmission electron microscope. Copyright Erkka J. Frankberg 2017

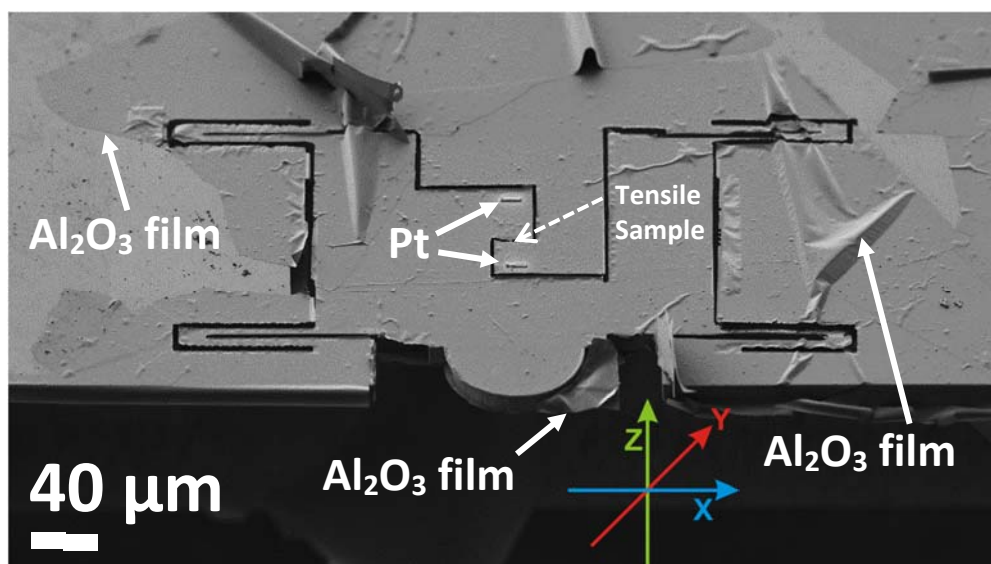


Figure 2.7: Scanning electron microscope image of a silicon push-to-pull device with Al_2O_3 thin film floated on the device and cleaned with FIB to produce a tensile sample ready for testing in TEM. Copyright Turkka Salminen / Erkka J. Frankberg 2017

2.6 Quantitative *in situ* mechanical testing in TEM

We conducted the mechanical testing in real time inside a transmission electron microscope. This allows simultaneous acquisition of numerical mechanical response as force versus displacement and imaging the deformation mechanism with electrons. The reason for choosing this method is that the elemental processes happening during deformation in PLD Al_2O_3 are unknown and it is possible to observe them using TEM.

We used two different equipment for *in situ* mechanical testing: a Hysitron PI 95 PicoIndenter TEM sample holder (Bruker Inc.) and a Nanofactory TEM sample holder (Nanofactory Instruments AB). The device is mounted on a TEM sample holder and can be placed directly in the TEM sample holder slot for a given TEM model. **Figure 2.8** shows optical images of the nanomechanical testing devices. For practical reasons, all quantitative *in situ* tests were performed using the PI 95 system.

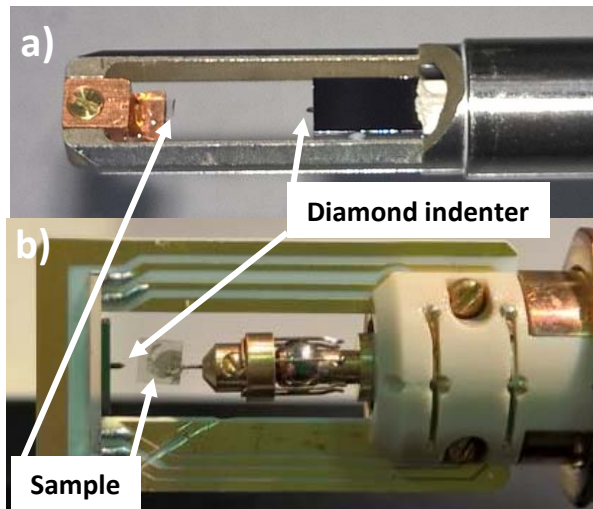


Figure 2.8: Optical images of the functional tips of the *in situ* testing devices for transmission electron microscope. a) Hysitron PicoIndenter P95 *in situ* sample holder for FEI microscopes and b) Nanofactory sample holder for JEOL microscopes. Copyright Erkkä J. Frankberg 2016

Testing devices use a capacitance based measurement to measure both total force (N) and total displacement (nm) [91]. Once a force is imposed on the diamond indenter, the movement of the capacitor plates in respect to each other produces characteristic changes in the capacitance which can be interpreted as changes in

displacement. The changes in capacitance generate an electrostatic force between the measuring electrodes which is used to measure the loading force. The PI 95 device used for all quantitative mechanical tests has nominal load noise floor of 200 nN with 1 mN maximum force and a nominal ≤ 0.02 nm displacement resolution [91]. In tensile test, the spring force of each push-to-pull device was measured after the sample was broken. For each push-to-pull device, three spring force measurements were averaged and the average was subtracted from the tensile test data to produce the true force subjected to the tensile sample alone.

The sapphire substrate with the coated anvil tools or a push-to-pull device was glued on a dedicated copper sample holder using “crystal bond” adhesive at < 150 °C using a hot plate. The sample holder was then screwed in place as in **figure 2.8**. Next, the sample holder was inserted in the TEM sample holder socket. The stationary sample/PTP device and the diamond indenter tool are aligned in x, y and z direction in the TEM by moving the diamond indenter. The **figure 2.9** shows the typical aligned setup in TEM before each compression/shear tests and tensile tests.

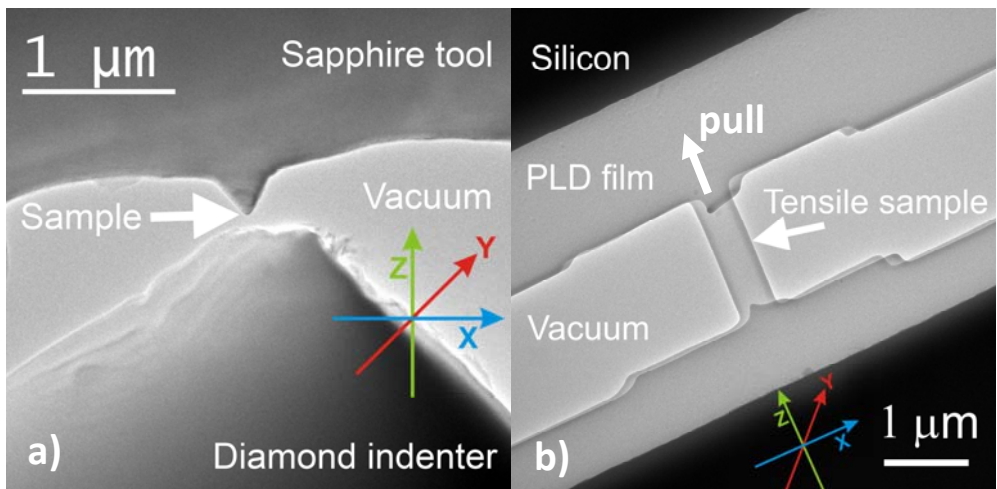


Figure 2.9: Transmission electron microscope images of a) typical setup prior to each *in situ* compression/shear test and b) a typical setup prior to each *in situ* tensile test. As the film typically covers the push-to-pull device from both sides, the backside film is cut using FIB, which leaves some traces of the cut film as shown in the TEM image of the tensile specimen. All tests proceed primarily along the Z-axis. Copyright Erkka J. Frankberg 2016 - 2017

All mechanical tests were performed by displacement controlled manner. For compression/shear testing 1 nm/s nominal speed was used for both indenting and retraction with a 3-5 s hold at peak force and for tensile testing we used 1 nm/s

nominal speed for indenting and indentation was continued until fracture. The tests were filmed with 25 frames/s and MJPEG video compression using a video capture software included in the Hysitron picoindenter P95 software bundle. Note that when using the push-to-pull device, the movement of the indenter is forward and the device geometrically transfers the forward movement into pulling in the sample.

Compression/shear tests were performed using a nominal 87 000 X magnification and an average screen current of 3.57 nA during imaging. Tensile test was performed with a nominal magnification of 10 000 X and an average screen dose of $0.29 \text{ e}/\text{\AA}^2\text{s}$ during imaging. Dwell time with the electron beam ON was kept minimum prior to all tests.

Tests were performed in 3 different modes: Electron beam ON, electron beam ON/OFF and electron beam OFF. For the electron ON tests, the whole deformation process was imaged alongside with the mechanical force/displacement data produced by the indenter tool. For electron beam ON/OFF tests, the beam was turned OFF during the test to record the effect of the electron beam on the mechanical properties.

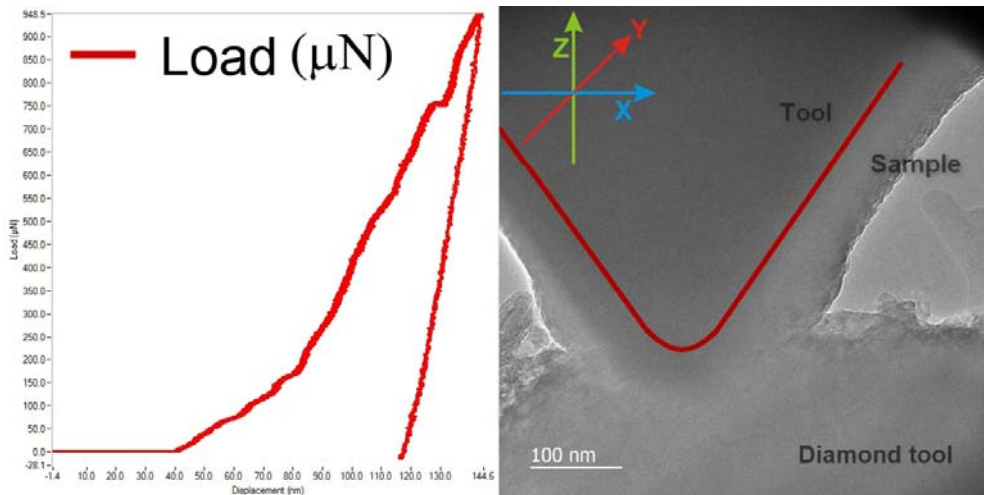


Figure 2.10: A side-by-side image of the raw data acquisition at the test end-point of the sample 3.1. At this moment, the diamond tool is being retracted away from the sample and the load has returned to zero value. The diamond tool moves primarily along Z-axis during indentation. The area under the load curve represents the plastic deformation work $W=Fs$. Copyright Erkka J. Frankberg 2017

For electron beam OFF tests, the electron beam was kept ON only during the microscope alignment procedure, switched OFF (Using “beam blank” command) just prior to contact with the diamond indenter and kept OFF during the whole mechanical test.

Each test creates force and displacement raw data and the data was linked to the *in situ* video created by using a time stamp for each data point that corresponds to a particular video frame. A raw data acquisition is demonstrated in the **figure 2.10**.

2.7 Measuring sample strain

We used a combination of *in situ* capacitive measurement and digital image correlation (DIC) to measure the strain [] in the sample films. Sample strain was obtained by measuring the displacement [m] of the testing device or displacement of the sample and comparing the displacement to the original length of the sample.

Using digital image correlation, in compression/shear test we measure only the displacement of the tools due to overlapping of the tool and the sample and in tension, we can measure the sample displacement directly. Both capacitive and digital image correlation measured displacement indicates the momentary change in the displacement in respect to the original size of the sample, which corresponds to engineering strain in the PLD Al₂O₃ film. The used DIC software algorithm was revised by using manual image correlation for some datasets and the results matched each other well. The capacitive measurement is used to produce quantitative data only in the case of electron beam OFF tests, where using DIC was not possible. For beam OFF the capacitive measurement were calibrated as introduced later, as otherwise the measurements by capacitive means were found not to be fully reliable.

Digital image correlation was conducted at Tampere university of Technology by Mikko Hokka. Digital image correlation was used to have an independent quantification of the sample strain during *in situ* TEM experiments. Individual images were extracted from the *in situ* videos with an interval of 0.5 – 3.3 s and digital image correlation was used to calculate the 2D displacement vectors on the selected regions of interests in the obtained microscope images.

The DAVIS Software Suite (v.8.3.1) from LaVision was used to carry out the DIC calculations. A simple scale calibration was used to convert pixels into nanometers using the scale bar in the microscope images. The 2D displacement calculations

were carried out using a subset of 35 by 35 pixels and step size of 10 pixels. A high accuracy interpolation with 6th order spline functions were used for the subpixel interpolation, whereas a 2nd order nonlinear shape functions were used allowing more complex deformation of the subset. In the case of displacement calculations of the upper and lower parts, the regions of interests were selected far away from the contact zone of the two pieces where the strains are small. However, for the evaluation of the strains in the contact zone, large deformations were observed and the subsets were expected to deform significantly.

In compression/shear tests, the displacement was calculated as the difference between the displacement of the lower part (diamond indenter) and the upper part (coated tool), by selecting a region of interest from the indenter and the sample separately, and measuring the displacements as an average between the selected areas. The area was selected so that no other bulk feature overlapped the area during the whole test. An example for the data exportation is shown in **figure 2.11**, where the red rectangle indicates the area where the displacement values were extracted.

In tensile test, the displacement was measured from the displacement of the moving upper part and stationary lower part of the tensile sample (**Figure 2.9**). Both manual image correlation and DIC software algorithm were used by following the moving edge of the tensile sample from image to image.

The uncertainty estimation for DIC software algorithm used in compression/shear tests was carried out by calculating the displacements on the upper part of the compression setup prior to contact. The coated tool in upper part should not move prior to contact, and therefore, any displacements can be used as an estimate for the noise level. The magnitudes of the individual sources of the uncertainties are quite difficult to quantify for *in situ* TEM tests, and therefore an overall error estimate is used instead.

Figure 2.11 shows the displacements obtained in the upper part of the image after calculating the displacements for nine consecutive frames. The maximum displacement in this frame is approximately 3.5 nm and it is located in the lower part of the analysed region as indicated by the white colour. The maximum uncertainties are typically observed on the edges of the analysed regions, and they can easily be omitted when extracting the average values for further analysis. Furthermore, in the **figure 2.11** the typical displacement values are between 0.2 nm and 0.8 nm. The average displacement in the red rectangle is close to 0.5 nm, which represents the noise level in the DIC analysis.

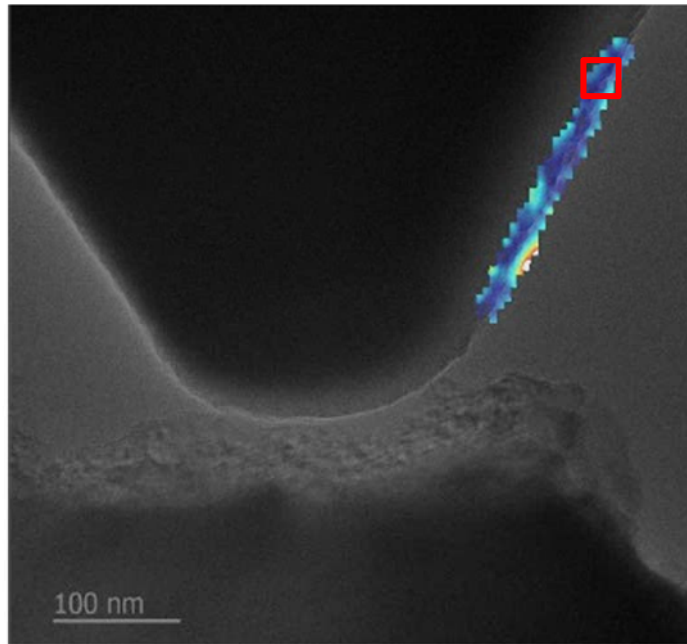


Figure 2.11: Estimation of the data noise level in digital image correlation measurements. Red rectangle indicates the area where the displacement values were extracted. Copyright Mikko Hokka / Erkki J. Frankberg 2017

This value reflects the mechanical vibrations of the testing and imaging systems when the test apparatus is moving, as well as the noise and uncertainties originating from the DIC calculations. In the example shown in **figure 2.11**, one pixel corresponds to 5.43 nm, and therefore, the accuracy of the DIC analysis is in the order of one tenth of a pixel, which is reasonable considering the challenging imaging conditions and limited contrast in the images.

By comparing the capacitive and digital image correlation results, we notice that both give a linear slope for displacement. **Figure 2.12** shows how the average displacement values of capacitive and DIC displacement match surprisingly well, but that the displacement slope of the same sample with capacitive measurement can significantly differ from the DIC measurement. We assume that the DIC measurement is the real representation of the displacement, which means that the capacitive displacement measured becomes rapidly more inaccurate as the measured data points are increased. As the nominal film thickness is 50 nm the capacitive measurement can still give an acceptable correlation in the early stage of the measurement, but whenever possible, the capacitive displacement must be

corrected and can be done, as the slope of single measurement appears always linear. The investigation on the origin of the error in capacitive displacement measurement was out-of-scope of this work. Calibration of the capacitive displacement was done according to the manufacturer's instructions before any testing.

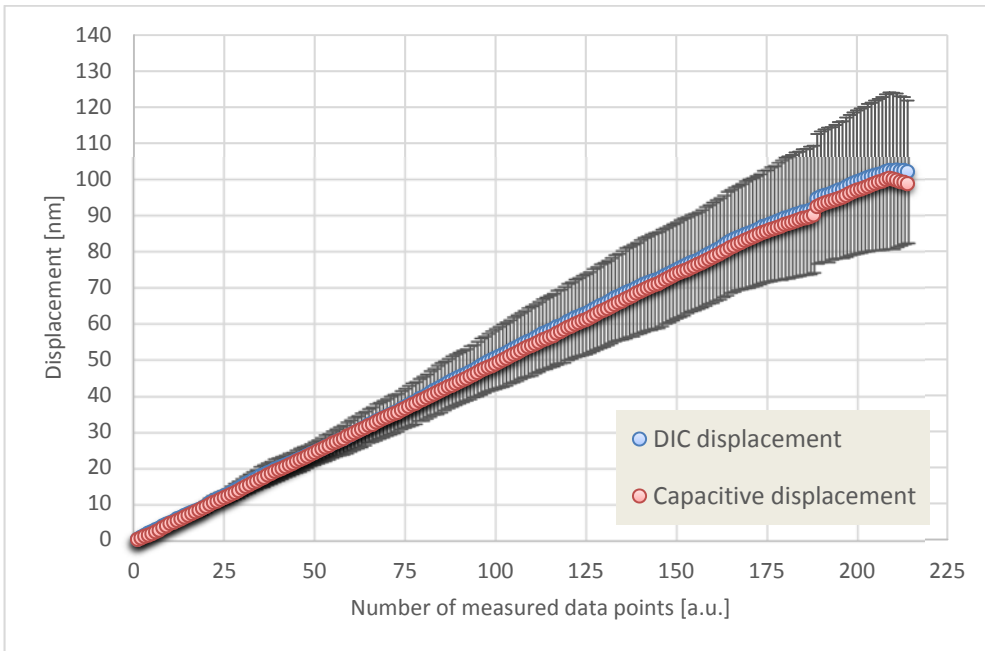


Figure 2.12: The averaged capacitive and DIC displacement data of 8 individual beam ON compression/shear tests in transmission electron microscope. Error bars represent the standard deviation of DIC data, standard deviation of capacitive data is very small compared to DIC error and not presented in the figure. The DIC data shows that the capacitive measurement becomes increasingly inaccurate when the total displacement in a test is increased. The deviation is not observable in the capacitive data alone. Copyright Erkka J. Frankberg 2017

In the Beam OFF compression/shear tests where DIC is not possible, the capacitive displacement data can be calibrated due to the nature of the test setup: When we reach a 1.0 sample strain, the elastic stress starts to build up again as we start to deform the much stiffer sapphire below the sample film. As the capacitive/DIC displacement relationship is always linear, we can mark the transition point as strain 1.0, if we change the sample thickness to allow 1.0 strain at this point, then the calibrated capacitive displacement will give an accurate engineering strain value.

Sometimes a clear elastic stress increase at 1.0 strain is not observed and is probably due to delamination of the sample film from the substrate tool.

2.8 Measuring contact and cross-sectional areas

In order to quantify stress in compression/shear and in tension, we have to quantify the area of loading. For compression/shear, we measure the contact area between sample and indenter and for tension, we measure the smallest cross-sectional area of the sample.

The compression/shear contact area was determined using several complimentary techniques. Projected areas of the residual indents were determined primarily using SEM images of projected residual indents combined with *in situ* TEM images during and after tests (TEM images not available during beam OFF tests). To estimate the real contact area in respect to projected area, Patrice Kreiml and Megan J. Cordill performed additional atomic force microscopy (AFM) measurements at Erich Schmid Institute of Materials Science. Atomic force microscopy measurements were primarily used to find out a correction factor for the projected areas to produce an estimated real contact area for each sample. Additionally AFM was used to verify SEM measurements of projected areas of the residual indents. Moreover, projected areas were verified using a finite element model by comparing the experimental contact area given by the model as a function of contact load.

In compression, typical estimation of the contact area was done by measuring the two largest diameters D_{1end} (x – axis) and D_{2end} (y – axis) of the residual indent by using TEM and SEM images and calculating the projected area A_{proj} of the elliptical residual indent $A_{proj} = \pi(D_{1end}/2)(D_{2end}/2)$. The ratio between diameters in the ellipse was determined to approximately 1.6 using microscopy images, which was used for all calculations. Projected area was then corrected with a correction factor 1.36 given by AFM, to yield an estimate of the true contact area A ($A = A_{proj} * 1.36$). The same correction factor was applied for all area measurements. The measured true area of the residual indent was set to be the contact area at the point where the test had retracted back to a zero load. For that, we calculated from the data that an elastic spring back of approximately 8.5 % (displacement) happens once loading changes from peak to zero load. True contact area ($D_{1peak} * D_{2peak}$) at peak load was then calculated by removing the elastic spring back from both residual indent diameters. The shape of the sample is symmetrical so the change in the two diameters during compression was assumed linear.

We can estimate the starting contact area (D_{1start} and D_{2start}) on the sample from *in situ* TEM images (D_{1start} also available for beam OFF tests, and $D_{2start} = D_{1start} * 1.6$) and contact area during peak load from residual indents. The area from peak stress to the start is then calculated to happen by linear steps between measuring points as $\Delta D_1 = (D_{1peak} - D_{1start}) * N_{step}$ and $\Delta D_2 = (D_{2peak} - D_{2start}) * N_{step}$ while $\Delta D_1 \neq \Delta D_2$ and number of steps N_{step} is the number of the data point between D_{1start}/D_{2start} and D_{1peak}/D_{2peak} . True stress was then obtained by dividing the measured force with the measured immediate elliptical contact area for each data point.

In the tensile tests, we measured the change in the sample length using DIC. Then we estimated the thickness (y-axis) of the film using TEM cross-section images (example shown in **Figure 3.1**) of films deposited with the same parameters. For the sample PTP3 it was determined to be 42 nm (nominal thickness 50 nm). The change in width and thickness of the tensile sample (x-axis and y-axis) were measured by manual image correlation from *in situ* TEM data introduced earlier. First we determined from the *in situ* TEM images, the start ($d_{start} = 560$ nm) and end width ($d_{end} = 522$ nm) on x-axis. To determine the immediate width during each measuring step the change is determined to happen by linear steps $\Delta d = (d_{start} - d_{end}) * N_{step}$ in the sample. The ratio (d_{start}/d_{end}) = 4.5 % is then assumed equivalent to the change in thickness of the sample during loading from start ($h_{start} = 42$ nm) to end ($h_{end} = 42 * 0.045$), as $\Delta h = (h_{start} - h_{end}) * N_{step}$. True stress was obtained by dividing the measured force with the measured immediate rectangular cross sectional areas for each data point.

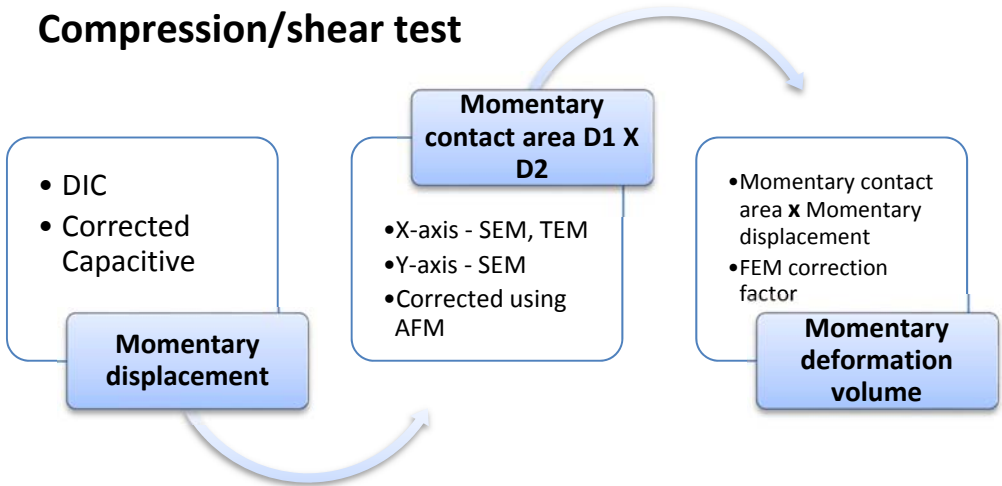
2.9 Measuring deformation volume

For theoretical work and viscosity calculations, we need the deforming volume V_{def} at each measuring step. A flow chart in **Figure 2.13** summarises the methods used to determine displacement/strain, area and volume in this study.

For compression/shear tests, the projected deformation volume V_{proj} was first estimated by multiplying the estimated true contact area [m^2] with sample DIC displacement [m] related to each measuring step. Then to obtain the true deformation volume V_{def} , we used finite element simulations to correct the measured projected values. This is because the FEM model takes into account the magnitude of the von Mises stress field induced inside the sample under compression/shear. Therefore, as we could match the contact area as a function of load in the experiments and in the finite element simulations, we could calculate a

correction factor using the true plastic volume given by the FEM model. The obtained correction factor 4 was then applied to all calculated projected volumes to yield the true deformation volume V ($V_{\text{def}} = V_{\text{proj}} * 4$).

Compression/shear test



Tensile test

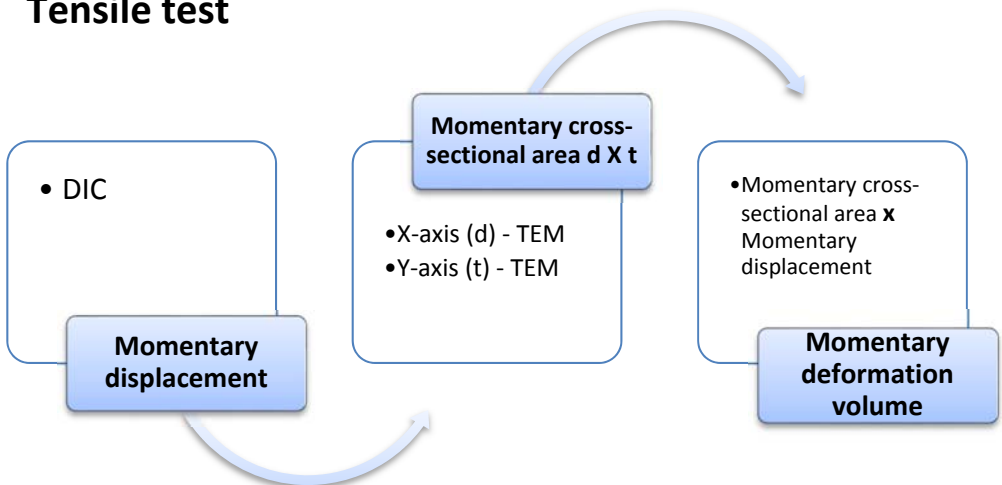


Figure 2.13: Schematic presentation of the workflow in measuring momentary displacement, area and deformation volume related to *in situ* TEM compression and tensile testing. Copyright Erkka J. Frankberg 2017

For tensile tests, we assume that each moment the true deformation volume equals to the sample image correlation displacement multiplied by the immediate cross-

sectional area. Constructing a FEM model of the tensile test setup was out-of-scope of this work.

2.10 Atomistic simulations

Theoretical simulations were conducted at Tampere university of Technology by Janne Kalikka. Main idea was to compare the experimental mechanical response to the mechanical response predicted by the classical Newtonian interaction potential for amorphous Al_2O_3 . The independent numerical results on the mechanical properties were used to verify the obtained experimental results.

Atomistic simulations were carried out using the open source Large-scale Atomic/Molecular Massively Parallel Simulator (LAMMPS). For the LAMMPS simulations we use the Al_2O_3 interaction potential developed by Matsui [85], since it has been shown to effectively simulate amorphous [92], liquid [93] and different crystalline phases of Al_2O_3 [94]. All simulations were conducted using periodic boundary conditions in x, y and z directions in a cubic simulation cell to mimic bulk behaviour. A time step of 1 fs was used, temperature and pressure were controlled with a Nosé-Hoover thermostat and barostat as implemented in LAMMPS.

The amorphous template structure was created following the procedure described in Gutiérrez *et al.* [92]. A structure with 2.75 g/cm^3 density was heated to 5000 K, and equilibrated for 45 ps. The structure was then cooled to 3000 K over 60 ps, and equilibrated for 55 ps. The simulation cell was then scaled to increase the density to 3.175 g/cm^3 , and equilibrated for another 55 picosecond, after which the structure was cooled to 650 K over 650 ps. From this template a structure of desired size was cut, and equilibrated to 1 atm. pressure in 300 K over at least 300 ps after which the equilibrium density was 3.255 g/cm^3 . **Figure 2.14** shows the equilibrium structure of the ready simulation cell used to study mechanical properties of amorphous Al_2O_3 .

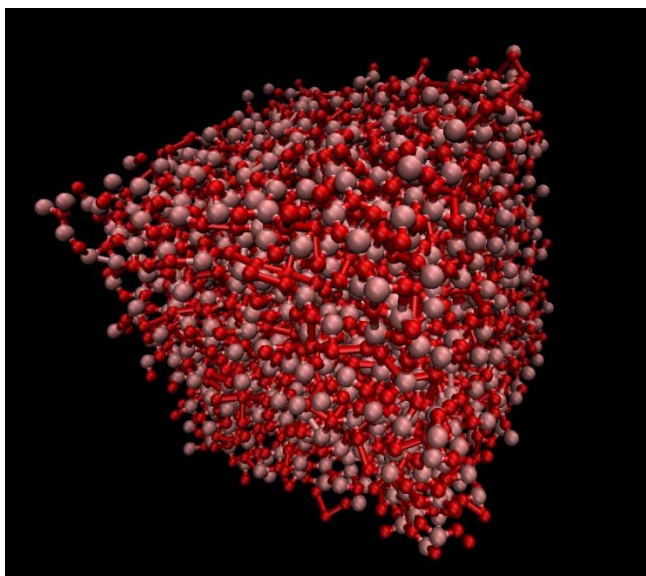


Figure 2.14: Rotated image of the equilibrated cubic simulation cell used to simulate the mechanical properties of amorphous Al_2O_3 using LAMMPS code. Aluminium ions are presented as red and oxygen ion as light brown. Copyright Janne Kalikka / Erkka J. Frankberg 2017

All compression and tensile simulations were done at 300 K. The simulated unit cell was a cube with 3 - 5 nm edge length consisting of 4000 - 12 000 atoms. Compression and tensile pull was done to 0 - 30 % strain with strain rates corresponding to 0.5 - 8 ns total compression time or tensional pull time. In practice, the simulation cell length along the direction of compression/tension was changed every 100 fs during the simulation and the deformation of perpendicular directions were controlled by 1 atm. constant pressure in those directions.

2.11 Finite element method simulations

Finite element method (FEM) simulations were conducted at Tampere university of Technology by Jouko Hintikka. Simulations were performed in three dimensions using the Abacus standard software bundle. The mechanical behaviour model was build using literature data for pulsed laser deposited Al_2O_3 elastic modulus and Poisson ratio [9, 76] and using the current molecular dynamic simulations results for elastic modulus and flow stress/critical stress. FEM simulations were carried out to verify contact area measurements (TEM, SEM and AFM) and measure the active elastic and plastic volume as a function of loading force in experimental

compression/shear tests. **Figure 2.15** illustrates the 2D geometry of the quarter model.

Experimental results on contact area measurements indicated that the resulting projected contact area of the residual indents have an elliptical shape with approximate 1.6 ratio between the radii D_1 and D_2 , which indicate that contact between tip and counter surface occurs with elliptical contact geometry. Diamond counter surface was modelled as a cylindrical block with thickness and radius of 150 nm and 320 nm respectively so that one of the flat faces is the contact surface. Sapphire tip was modelled by sweeping an arch with radius R_1 along secondary arch with radius R_2 . Hence, the shape of the tip had double curved surface. The R_1 corresponds to experimentally measured tip radius of 96 nm. R_2 radii can vary from sample to sample therefore different R_2 radii were used to study its effect on the resulting plastic volume. The height of the tip was 270 nm. The tip was divided in two sections so that 60 nm thick top layer could be given different material properties than the bulk of the tip, representing the thin film specimen. The model utilizes symmetry in two directions so that only a quarter of the geometry was modelled.

Used element was linear hexahedron with hybrid formulation (C3D8H) for the tip, which is suitable for simulating large strains. Standard linear hexahedron elements (C3D8) were used in the diamond counter surface. Element size varies in the model but was approximately 7 nm at the contact, though 5 nm and 10 nm mesh sizes were used also to verify that used element size was sufficiently small. The simulation used adaptive re-meshing rule (ALE) to cope with large mesh distortion due to large plastic deformation.

Symmetry boundary conditions were applied to the symmetry planes of the model. The bottom surface of the tip and the top surface of the counter surface were coupled to two separate reference points. Initially, all degrees of freedom for the two reference points were set to zero, and the test was then simulated by moving the reference points towards one another in linear fashion in a single load step with 40 calculation increments with the setting for non-linear geometry set on (NLgeom). Contact between tip and counter surface was modelled using standard "hard contact" formulation in normal direction, and the contact was frictionless.

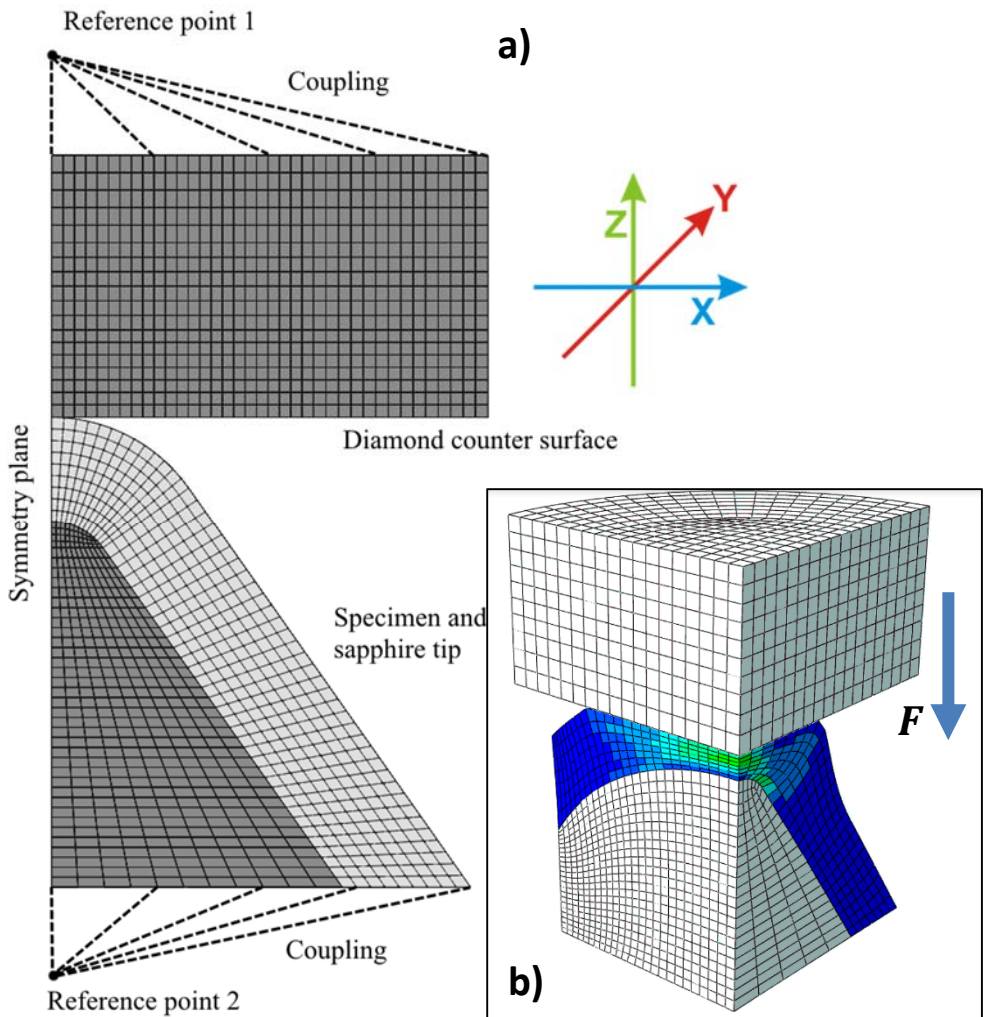


Figure 2.15: a) Two dimensional illustration of the used quarter symmetrical finite element method model and with axis's corresponding to the *in situ* experimental setup and b) a rotated image of the quarter symmetrical model during a compression simulation. Copyright Jouko Hintikka / Erkka J. Frankberg 2017

The diamond counter surface and the bulk sapphire tool were given linearly elastic material properties without plasticity. The specimen on the surface of the tip was given elastic plastic material following isotropic hardening rule (von Mises). The elastic-plastic mechanical behaviour model was adapted from the molecular dynamic simulations results and from literature [9, 76].

Table 2.3 lists the elastic moduli and Poisson ratio for compression tools and for the sample film and **Table 2.4** lists the abacus parameters for the plastic part of the mechanical behaviour model.

Table 2.3: Elastic moduli and Poisson's ratios for the used materials.

	Elastic modulus [GPa]	Poisson ratio []
Diamond	1200	0.22
Sapphire	350	0.30
Amorphous Al₂O₃	195.3 [9] (70*)	0.294 [9]

* To study the effect of lower elastic modulus, also 70 GPa was used.

Table 2.4: Plastic material model for finite element method simulations of amorphous Al₂O₃.

Sy1 (Yield starts)	3 GPa
ep1 (Amount of plastic yield)	0
Sy2 (Flow stress)	4.5 GPa
ep3	0.847

Next, we will go through the most important results and discuss their meaning and contribution regarding the introduced theory of plasticity in amorphous Al₂O₃.

3. Results and discussion

In this section, we show all results of the experimental mechanical testing of pulsed laser deposited Al_2O_3 films in transmission electron microscope and compare them to the atomistic simulation results.

First, we cover the characterization results that are important to understand the as-deposited structure of the Al_2O_3 films and how they react to the testing environment, mainly a high-energy electron beam. In addition, we discuss the tool development results regarding *in situ* TEM mechanical testing. Finally, a theory explaining the mechanical behaviour is introduced and discussed.

3.1 Structure and stability of pulsed laser deposited Al_2O_3

The precise structure of the pulsed laser deposited (PLD) Al_2O_3 films is under a debate [9, 76, 74] (Albeit, the structure of all glasses is under debate), therefore a thorough examination of the film structure is needed to understand the mechanical test results. To study the effect of sample preparation on the film structure and characteristics, samples were prepared using several different sample preparation methods introduced in the previous chapter.

All PLD Al_2O_3 films were characterized in TEM. The electron dispersive spectroscopy reveals that all samples compose of mainly aluminium and oxygen. In addition, no sodium or chlorine was found in the carefully rinsed NaCl float samples. The FIB lift-out sample contains a minor peak of gallium, the FIB ion source material, which is a well know effect of focused ion beam milling.

The thin films that where directly deposited on thin sapphire edge and the mechanical test anvils (IIT1, IIT2 and IIT3) have a native, as-deposited structure, which is mostly amorphous and metastable. In addition, the NaCl floated samples were found to be largely amorphous and appear and behave very similarly as the directly deposited native samples. Both directly deposited and floated samples also contain modified areas with nanocrystals of roughly 4 - 10 nm diameter, but the concentration of nanocrystals in the fully native areas is found to be low in most cases, approximately 0 – 10 crystals per 1000 nm^2 . **Figure 3.1** shows as cross section view of directly deposited PLD Al_2O_3 film on top of an ABeaM thinned sapphire edge (sample IIT1). The thicknesses of the film vary from the nominal thickness, which is taken into account when quantifying the mechanical test results.

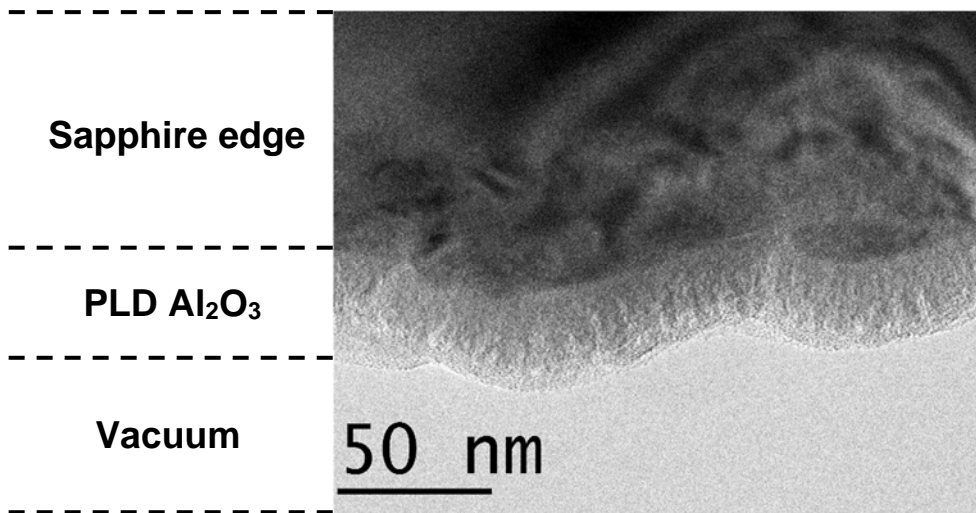


Figure 3.1: Transmission electron microscope cross-sectional image of a PLD Al₂O₃ film directly deposited on an electron transparent sapphire edge, sample name IIT1. Copyright Erkka J. Frankberg 2016

In the as-deposited state of the film, the metastability of the amorphous phase is primarily indicated by a fast crystallization upon a critical electron beam dose. **Figure 3.2** illustrates the crystallization behaviour of the amorphous Al₂O₃. The amorphous rings have vanished after 120 s from beginning of the irradiation and show spot pattern typical for crystalline structure. After several minutes of irradiation, small 20 - 40 nm crystal are observed in bright field images by diffraction contrast. Native ($t = 0$ s) electron diffraction image is obtained by moving the electron beam in diffraction imaging mode in to a native region of interest. Once the crystallization is launched, it is fast and cascades outwards from a given point until the whole electron beam affected area is crystallized. The electron beam induced crystals can have a wide range of sizes from few tens of nanometers to micron size. The electron beam induced crystallization behaviour of the as-deposited PLD Al₂O₃ is found to be largely similar to previously reported behaviour of amorphous Al₂O₃ [71, 73, 95].

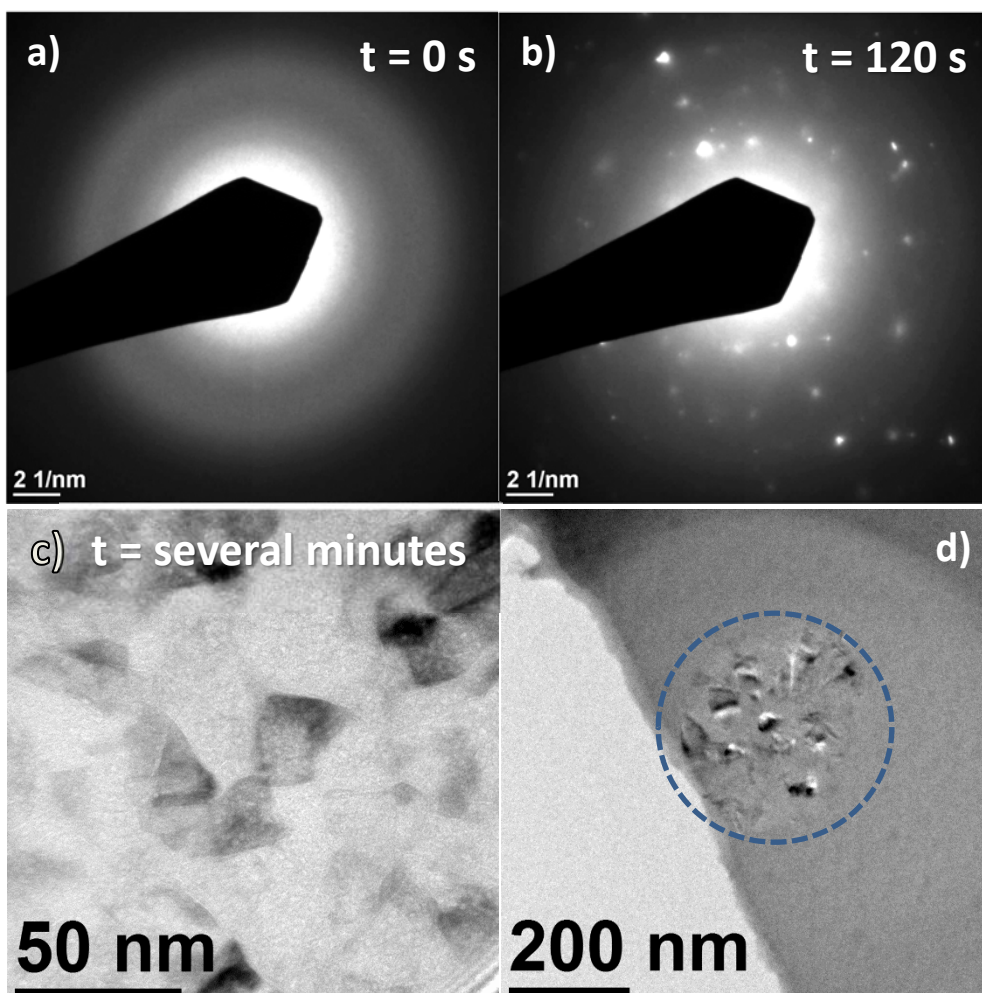


Figure 3.2: a) Electron diffraction pattern of as-deposited PLD Al_2O_3 film prepared by NaCl floating technique showing amorphous rings. b) Diffraction pattern after 120 s exposure to the electron beam at diffraction imaging conditions, showing that rings patterns vanish and a spot pattern emerges which indicates crystallization of the film. c) A bright field TEM image with inserted objective aperture, after exposure of several minutes to the electron beam, showing diffraction contrast from nanocrystals with 20 – 40 nm diameter. d) Finally a lower magnification image of an electron-beamed area showing a crystallized area of roughly equal to the beam spot size used during the crystallization. Copyright Erkkä J. Frankberg 2016

As noted earlier, some areas of PLD Al_2O_3 films show very different morphology and behaviour under electron beam compared to the as-deposited areas. Common to all these areas is, that they are no longer reactive to the electron beam and are

either fully amorphous or contain small nanocrystals typically in range of 1 - 10 nm. These areas are found often, but not exclusively, in the edges where the sample has for example ruptured during sample preparation. **Figure 3.3** shows how some areas have enough nanocrystals to give a clear spot pattern in electron diffraction. The two visible circles in the pattern are indexed to belong to (400) and (440) planes of gamma (γ) phase Al_2O_3 according to ICCD PDF 00-050-0741.

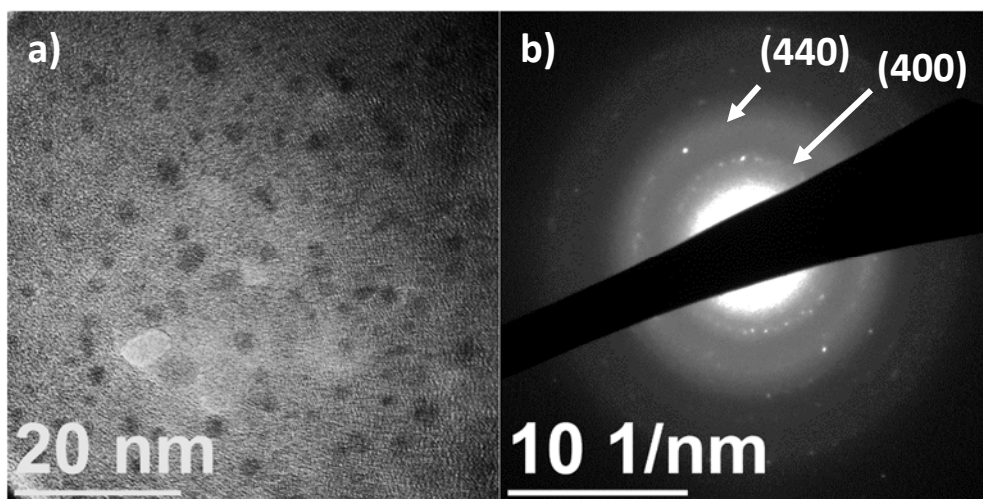


Figure 3.3: Example of a modified area in PLD Al_2O_3 film prepared by NaCl floating technique. a) Bright field image where the dark spots scattered in lighter background are 1 - 4 nm crystals in amorphous matrix as indicated by b) the electron diffraction pattern taken from the same location indicating rings from (400) and (440) planes of gamma (γ) Al_2O_3 . Copyright Erkkä J. Frankberg 2016

In several cases indicated by **figure 3.4**, individual or groups of Al_2O_3 nanocrystals are detected in amorphous Al_2O_3 matrix. As a direct evidence of crystallinity, single nanocrystals show phase contrast at high resolution [96]. Some groups of nanoparticles imaged by diffraction contrast inside the film do not show phase contrast, mainly due to too thick surrounding amorphous matrix and the crystallinity of these areas was detected by electron diffraction (as in **figure 3.3** and **figure 3.4c**). Unlike possible voids, these crystals are highly inert to electron beam. Voids and void formation in the PLD Al_2O_3 films is discussed later in detail.

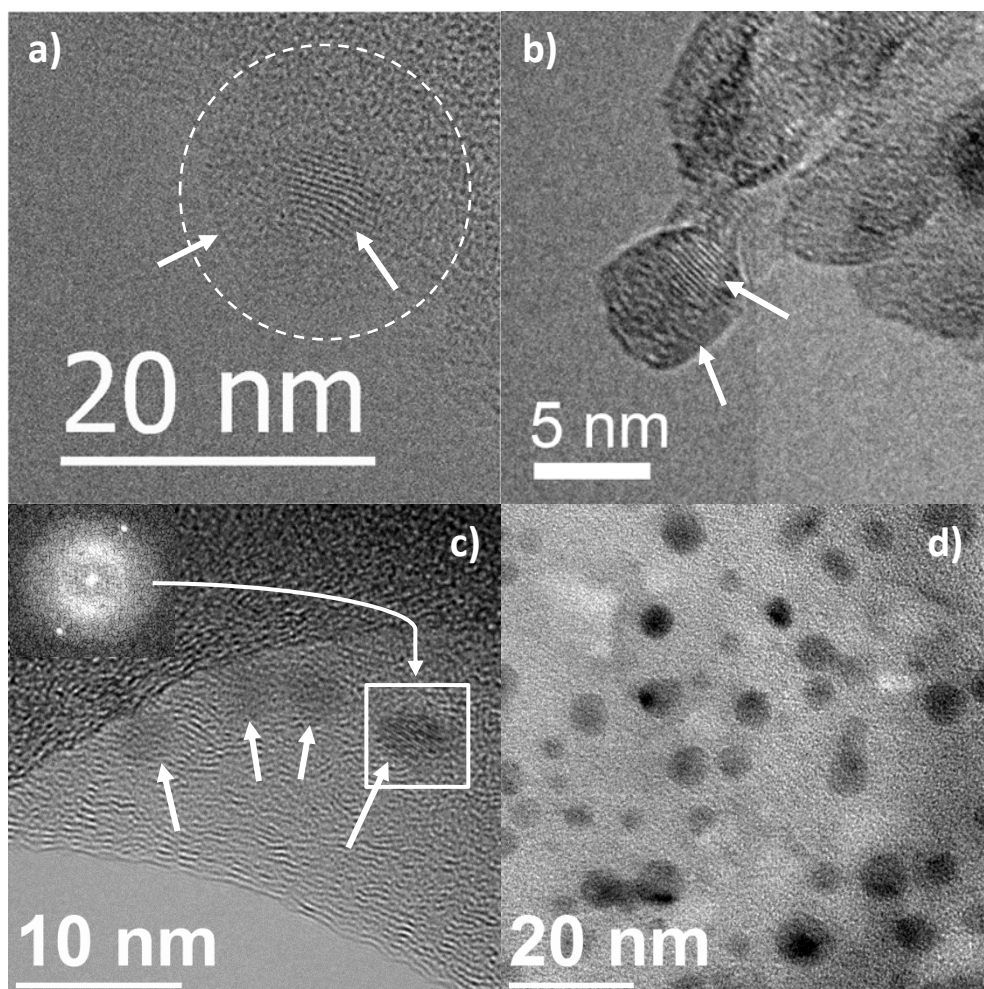


Figure 3.4: Samples prepared by NaCl floating technique showing a) & b) high resolution TEM images of an Al_2O_3 nanocrystal inside a round, amorphous shell. c) Group of nanoparticles with a local electron diffraction located by a white box and showing a Fourier transformation pattern of a single nanocrystal and d) a larger group of nanoparticles without clear phase contrast. All areas with nanocrystals are stable in a condensed electron beam in both 200 – 300 kV acceleration voltage. Copyright Erkka J. Frankberg 2016

We also found that the beam-induced crystallization does not happen in some of the thin sections close to the rupture. We believe that this indicates a mechanical relaxation process through mechanical stress and strain during rupture. **Figure 3.5a** shows a fully amorphous relaxation area at a ruptured edge and a relaxed strip of material along the edge that resists crystallization, and as a comparison, an edge

that allows crystallization all the way. Crystallization happens normally outside the relaxed areas as indicated by **figure 3.5b**.

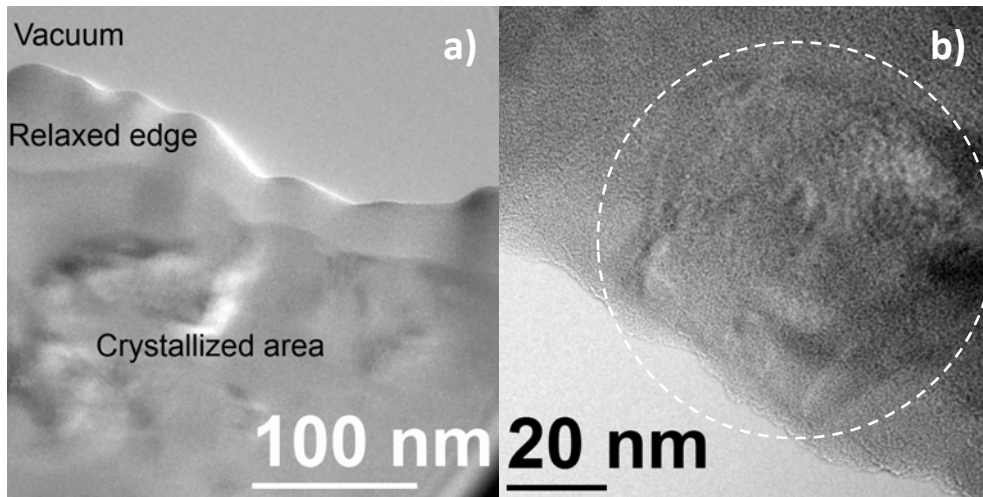


Figure 3.5: TEM images of a) mechanical relaxation of the ruptured edge in Al_2O_3 film prepared by NaCl floating technique where electron beam induced crystallization happens only outside the relaxed sample edge and b) a Non-relaxed sample edge, which allows full crystallization. Copyright Erkka J. Frankberg 2016

The general morphology of the films is smooth without signs of defects or voids, but in addition, in some locations of the film we detect rough granular structures that could originate from small condensates formed by cooling from plasma prior to hitting the substrate [73]. A light contrast lines between the granules can be detected, which likely are elongated voids between the granules, indicating that the structural cohesion in these areas is not perfect after deposition. The condensates often include a void inside which is deceptively similar in shape, size and contrast to the nanocrystals we found in some areas. Adjusting the focus in over and under focus reveals them voids and when imaged with condensed electron beam, the voids disappear. The same diffusion process that induces crystallization and subsequent densification of the structure probably causes disappearing of the voids. Vacancies in the void are diffused outward to allow minimization of surface energy in the voids. **Figure 3.6** shows examples of condensates and voids inside the condensates and how the void contrast changes during defocusing.

Samples prepared by FIB lift-out and by abrading produce quite different structure and stability to the film.

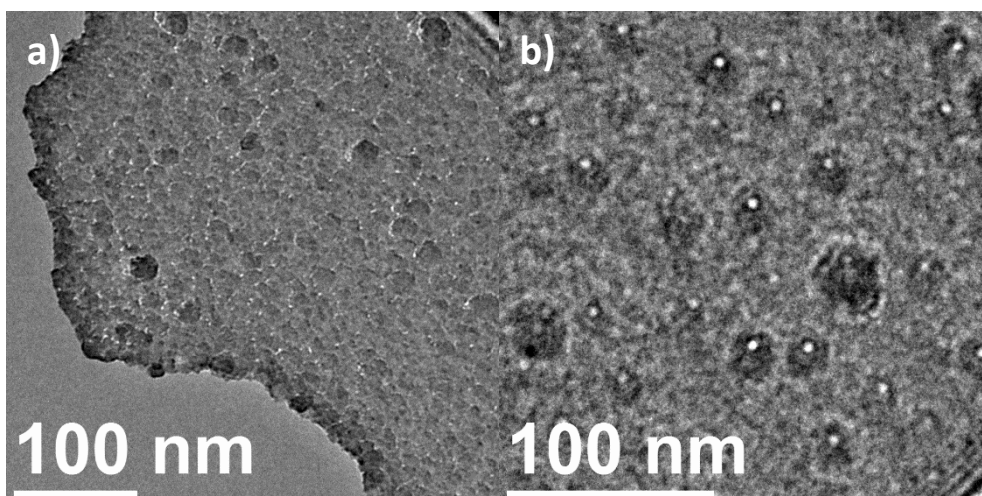


Figure 3.6: Defects produced during thin film deposition. a) An example of the rough granular structure found in some parts of the Al_2O_3 films with light contrast lines between the darker round granules indicating poor cohesion and b) individual condensates with a void (white dots) inside each condensate. Copyright Erkka J. Frankberg 2016

The FIB lift-out sample has reacted with the gallium ion beam during sample preparation, which is detected by electron dispersive spectroscopy as a gallium peak all around the sample. The film is mostly amorphous similar to as-deposited films. In addition, small concentration of nanocrystals are found around the film, both in edges and in the body of the film, embedded in the amorphous matrix.

A major difference to previous results is that the whole film is inert to the electron beam, which indicates a relaxation has happened, but this time likely induced by the penetrated gallium ions as minimal mechanical manipulation is subjected to the film during preparation. **Figure 3.7** shows nanocrystals on Al_2O_3 film produced by FIB lift-out technique in TEM. Crystals seems to form bands of higher concentration parallel to the direction of the ion beam. The crystals are determined to be gamma alumina by measuring the distance (d-values) between the crystal planes in different orientations from electron diffraction pattern. Closest match is found to (400), (440) and (444) planes of gamma Al_2O_3 according to ICDD PDF 00-050-0741.

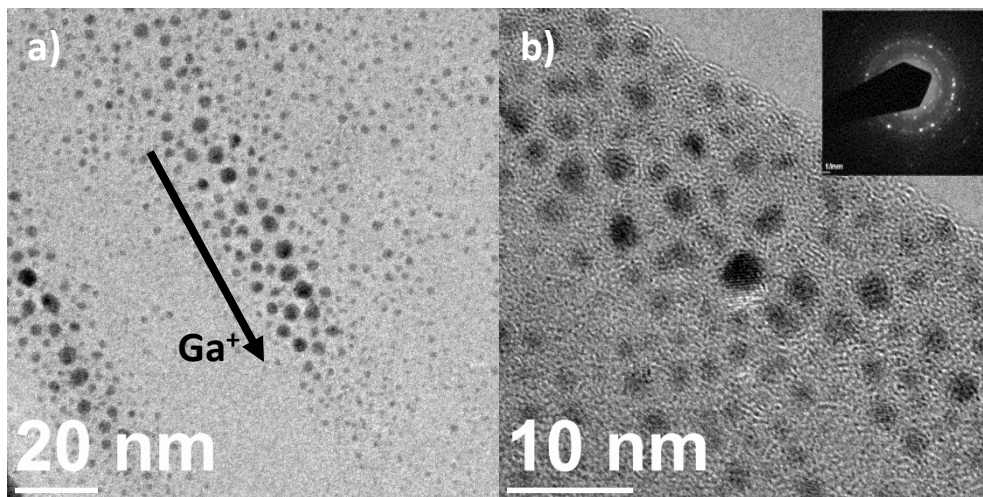


Figure 3.7: PLD Al_2O_3 film prepared by FIB lift-out technique showing a) bands of crystals formed parallel to the direction of the Ga^+ beam and b) high resolution bright field image of individual gamma (γ) phase Al_2O_3 nanocrystals in amorphous matrix with the corresponding electron diffraction pattern as an insert. Copyright Erkka J. Frankberg 2016

In the sample produced by abrasion, mechanical relaxation is again evident. Sample is revealed full of nanocrystals with a layer of amorphous surrounding each crystal. The crystal size is large compared to crystals found in most other samples, but have comparable size as the electron beam crystallized samples, although these were roundish in shape. In addition, this sample does not react to electron beam in any way. **Figure 3.8** shows bright and dark field TEM images of the abraded Al_2O_3 film samples with an electron diffraction insert. The electron diffraction pattern reveals fragments of crystalline silicon from the wafer substrate. But as EDS gives mainly Al and O with only a minor Si peak and the d-values of the high intensity rings correspond closely to (400) and (440) crystal planes of polycrystalline gamma (γ) phase Al_2O_3 (ICCD PDF 00-050-0741), we can state that the sample is a piece of the original PLD Al_2O_3 film.

The sample film has turned on itself during preparation to produce a double thickness film. Therefore, the film appears too thick to detect any phase contrast originating from the crystals. Dark field imaging reveals the concentration of crystals in the sample. As the TEM sample is contaminated with large amount of silicon fragments, this sample preparation method is not as useful as NaCl floating technique for example, or would require much thicker Al_2O_3 film to prevent substrate fragment generation during the abrasion.

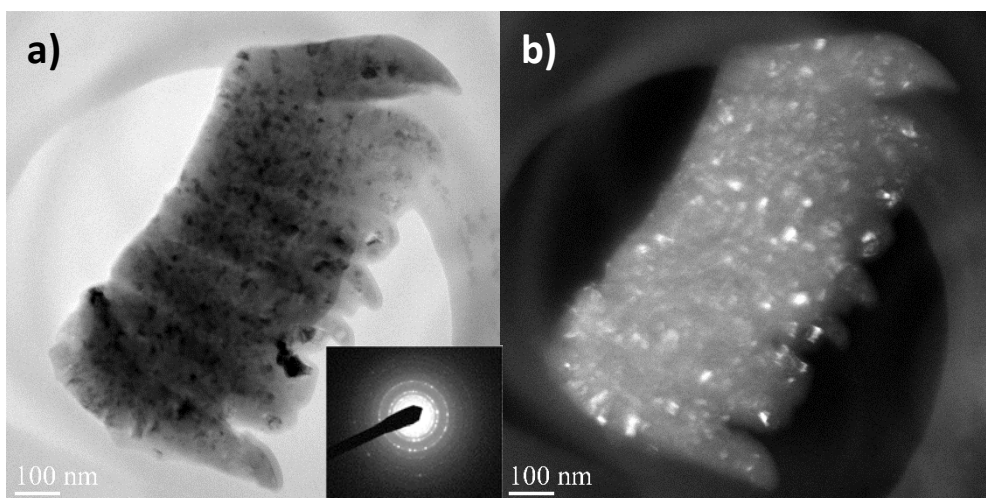


Figure 3.8: Abrasively produced TEM sample showing a) bright field TEM image with an electron diffraction insert indicating gamma (γ) phase Al_2O_3 crystals in amorphous matrix and b) dark field TEM image revealing the concentration of crystals (light contrast) scattered in the amorphous matrix. Copyright Erkka J. Frankberg 2016

As a summary, the pulse laser deposited structure is mostly amorphous and metastable and crystallizes upon critical dose of electrons when imaged using transmission electron microscope. All samples contain at least a small concentration of Al_2O_3 nanocrystals embedded in the amorphous matrix and the crystals have been identified to be gamma (γ) phase in all cases. The areas with nanocrystals are stable and do not crystallize further under the electron beam. The films are mostly homogenous and dense and the used pulsed laser deposition parameters seem to produce dense films. However, the films also contain some areas with rough granular structure and/or porosity between the granules indicating poor cohesion in the deposited material. As the poorer quality areas are found mostly on the edges of the samples, it can also be an artefact caused by the sample preparation, as we do not find this granularity in directly deposited films. In all cases, nanocrystals residing outside the sample edges are difficult to image in high resolution as the amorphous matrix is thick compared to the crystal diameter.

Based on all the characterized samples having the intricate structure of nanocrystals in amorphous matrix, two options exist: Crystals are produced either by selection of pulsed laser deposition parameters yielding crystals or created by stress/strain or defects induced by the sample preparation after film deposition. Either way it seems possible that PLD Al_2O_3 can be partly crystallized, which would have a tremendous impact also in the mechanical properties, if the crystal size and concentration can

be controlled. Also we can envision that fully crystallizing the PLD Al_2O_3 films is possible by other means than heat, as is demonstrated recently [72], which could improve the stability of the film considerably for applications that require chemical and thermal inertness.

3.2 Tool development for *in situ* TEM mechanical testing

The edges produced by the ABeaM technique on several sapphire substrates was found to be adequately electron transparent from approximately 100 to 300 nm distance from the edge in TEM with 200 – 300 kV acceleration voltages. Electron dispersive spectroscopy shows a minor peak of argon contamination on the edge which is anticipated. **Figure 3.9** illustrates the appearance of the milled sapphire edge using optical microscope, scanning electron microscope and transmission electron microscope.

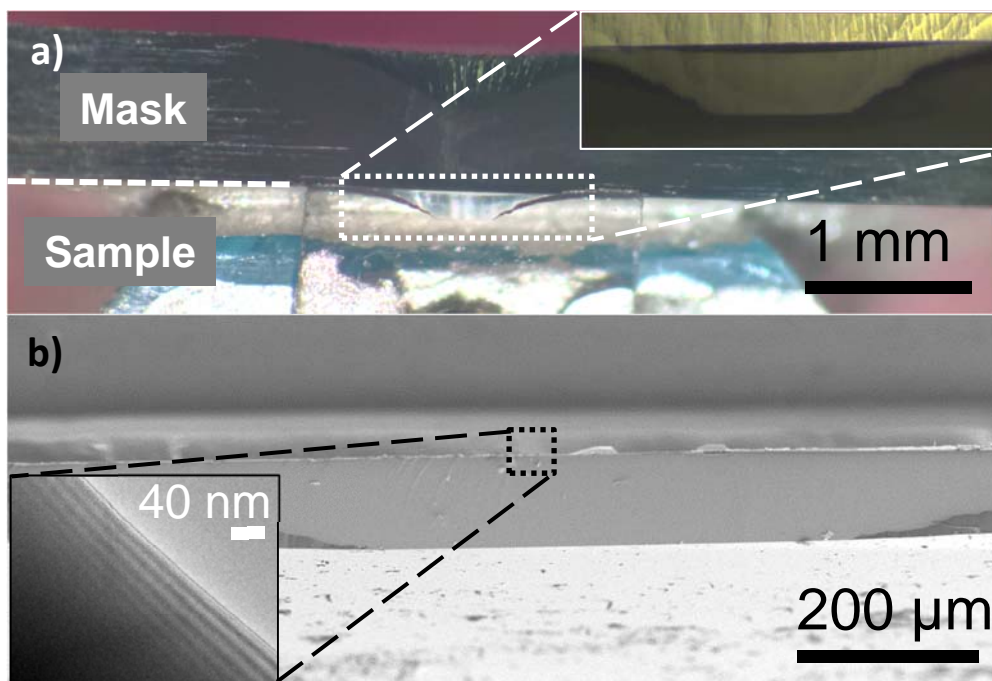


Figure 3.9: a) Optical microscopy images of the ABeaM produced sapphire edge right after milling and an insert showing the optical microscope view inside the broad ion milling device. b) Scanning electron microscope image of the milled edge and insert of the transmission electron microscopy image of the sharpened edge showing regular thickness fringes on the electron transparent sapphire edge. Copyright Erkka J. Frankberg 2017

When the thin edge is further processed using FIB, we produce anvils with a sharp, electron transparent tip. The **Figure 3.10** shows a top view of a group of 4 anvils in scanning electron microscope. Due to the charging effect, the anvils appear blurry at higher magnifications in SEM. For better image quality, TEM imaging reveals the cross sectional shape and dimensions of the uncoated anvils shown in **figure 3.11**. The **figure 3.11c** gives an example of the dimensions of the tips, with an opening angle of approximately 75° and a radius of curvature of approximately 20 nm. The tips with the optimized FIB milling parameters presented in the experimental section, produces a small 2 - 3 nm amorphous layer on the surface of the anvil detected using transmission electron microscopy. As the ion damaged amorphous surface layer will most likely have a different mechanical response compared to the original crystalline sapphire substrate, a smallest possible layer is desirable.

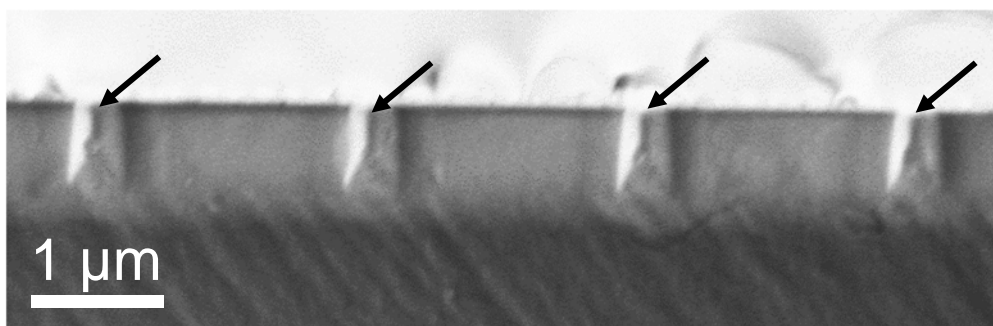


Figure 3.10: Scanning electron microscope top-view image of a group of 4 anvils produced using combined Angled Broad ion beam Milling (ABeM) and focused ion beam (FIB) milling techniques. Copyright Erkka J. Frankberg 2017

In addition, we performed a transmission electron microscope tomography on one of the uncoated anvils. **Figure 3.12** shows rotational tomography images of a sapphire anvil tool. The tomography reveals that the tip is elongated resembling a sharp wedge shape. The tip is tilted so that a cross-section view of the tip in TEM should be and is electron transparent although the total length of the tip is quite large regarding sufficient transparency in TEM. Note that the tomography shows sharp cross-sections at the 90° ends of the anvil, in reality the slope is more gradual.

The planned shape of the anvil was to have a flat tip with x-axis diameter of around 50 nm. Due to challenges in FIB milling, some of the tips are relatively sharp as tomography **figure 3.13a** shows, but in some cases the anvils have a flat tip. **Figure 3.13b** shows a comparison of two different tip profiles produced.

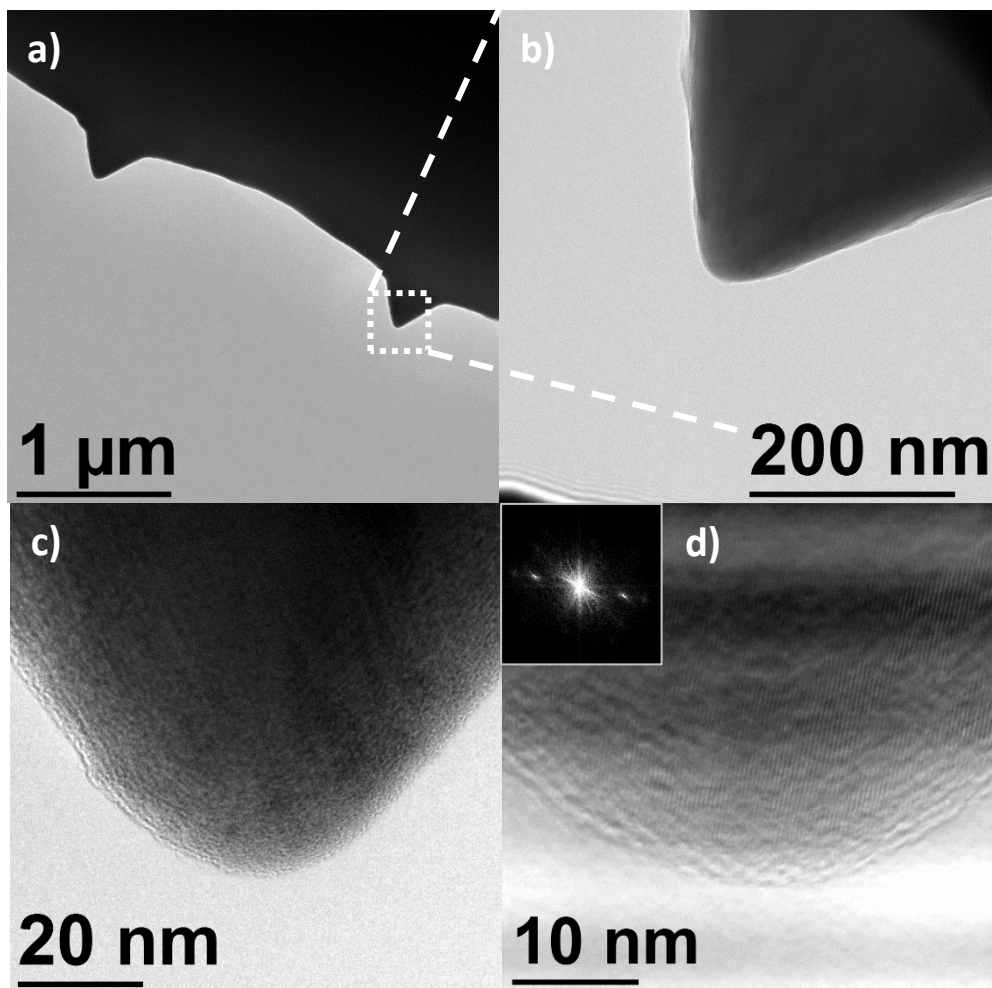


Figure 3.11: Transmission electron microscopy images of a sapphire anvil produced by combined Angled Broad ion beam Milling (ABeM) and focused ion beam (FIB) milling techniques. a) Profiles of two adjacent anvils, b) profile of a single tip c) dimensions of a single tip and d) a filtered (HRTEM Filter, D.R.G. Mitchess, v.1.3 Feb 07) high resolution image with an insert of Fourier transformation from the same image revealing the crystallinity of the tip. Copyright Erkka J. Frankberg 2016

Based on the characterization of the newly developed anvil tools, ABeM is a promising TEM sample preparation technique for direct TEM observation of bulk samples, also for heat sensitive samples such as polymers as the milled sample can be cooled down to for example liquid nitrogen temperature during milling. Combined with focused ion beam milling, ABeM is proven a powerful technique especially when milling non-conductive and hard materials (Al_2O_3 , SiC and diamond

etc.) where the FIB milling speed is inherently slow and milling is difficult due to non-conductive nature of these materials. ABeaM can be used to pre-thin a section of a hard material, which is then easier to process further using FIB.

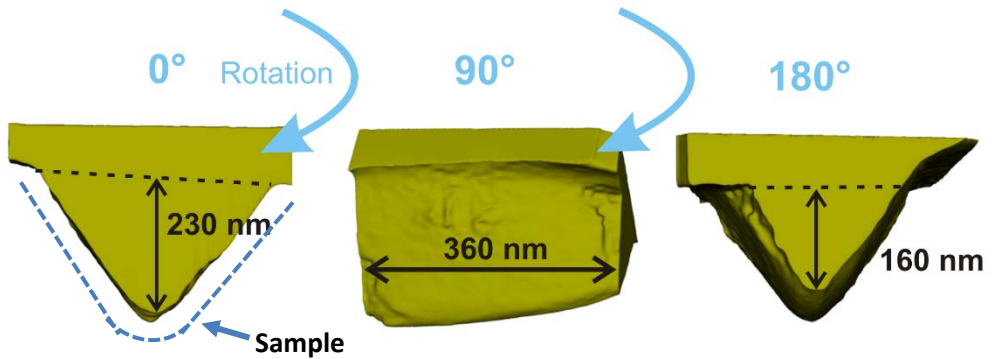


Figure 3.12: Tomography images showing a typical shape of the sapphire anvil used for mechanical testing. 0° angle represent the angle used during *in situ* TEM mechanical testing. Tomography reveals a negative slope towards back-end of the tool, which explains the transparency of the tip of the sapphires tool in TEM. Copyright Siddardha Koneti / Erkkka J. Frankberg 2016

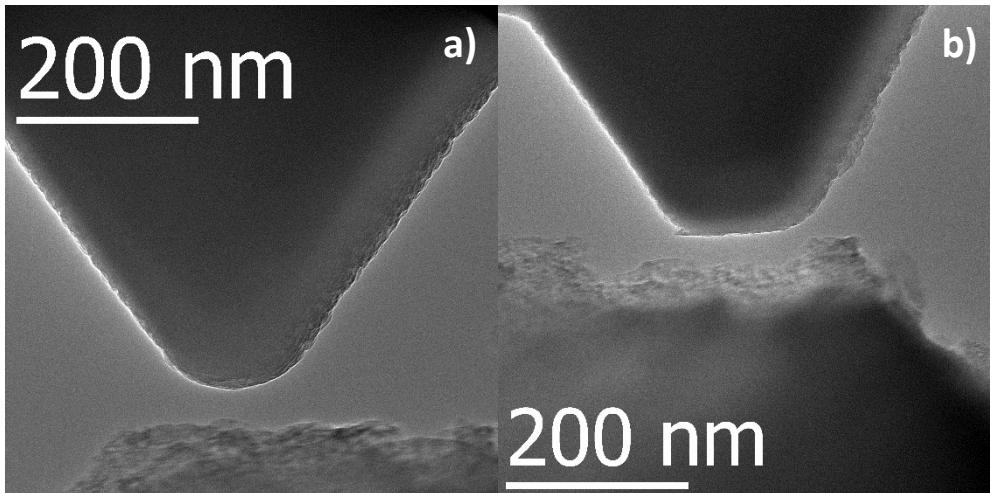


Figure 3.13: Comparison of sharp and flat tip anvil profiles. Copyright Erkkka J. Frankberg 2016

After optimizing the process parameters, we could scale the milling process up, to produce sets of 4 anvils with total amount of 84 anvils. The anvils can be coated in a single step using PLD or possibly by any other thin film method such as atomic

layer deposition, physical vapour deposition, magnetron sputtering etc. This process substantially improves the tools available for *in situ* mechanical testing of thin films. After deposition, the sample film at the tip of the anvil tool is electron transparent and directly observable by transmission electron microscope.

3.3 Characterization of the mechanical test samples

In the compression/shear test setup, after direct deposition of the PLD Al_2O_3 film on the sapphire, the film covers the anvils homogeneously as shown in **Figure 3.14**. The anvil is still recognisable below the coating, which allows accurate measurement of the film thickness for strain and strain rate calculations. The structure and stability of the film deposited directly on the anvils corresponds to the as-deposited state of the materials discussed earlier, which means that it will crystallize under a condensed electron beam. Therefore, a small magnification was selected to be used in the mechanical tests, to fully avoid crystallization and lessen the effect of electron beam induced surface diffusion on the mechanical test results.

In the tensile test, the sample was transported on to the push-to-pull device using the NaCl floating technique and further milled using focused ion beam to produce a tensile test specimen geometry. Examination reveals that due to ion beam damage, the composition of the film changes along the width of the sample. **Figure 3.15** shows the transmission electron microscope images of a tensile test specimen.

The damaged areas seem to cover approximately 80 – 130 nm from edge towards bulk from both sides of the tensile sample. The parts of the sample outside the clearly defected area are free of crystals and still react normally to electron beam and crystallize. This signals that most of the film is still in the as-deposited state and that the mechanical data closely represents the behaviour of a fully amorphous Al_2O_3 . The defected area is the probable cause of the fracture of the sample discussed in the next chapter. After the tensile tests, the structure still remains free of crystals and crystallizes under condensed electron beam. In future studies, the focused ion beam milling should be avoided as much as possible during sample preparation, as it will damage the samples and likely modify the mechanical response.

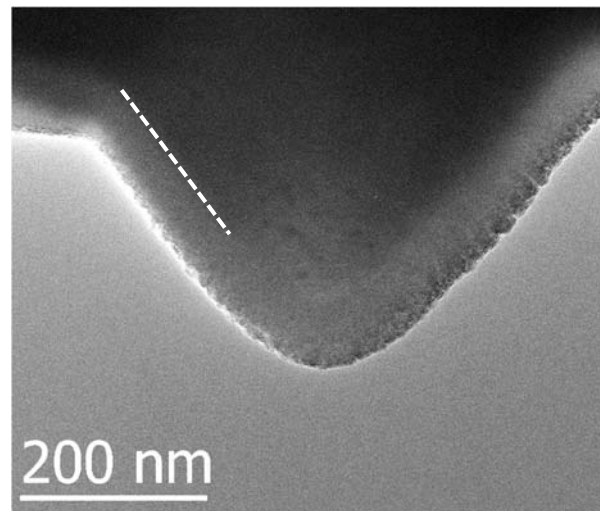


Figure 3.14: Transmission electron microscope image of a sapphire anvil directly coated with a pulsed laser deposited film of aluminium oxide. The sapphire tool is visible under the thin coating, a dashed white line points out the boundary between the film and the sapphire tool. Copyright Erkka J. Frankberg 2016

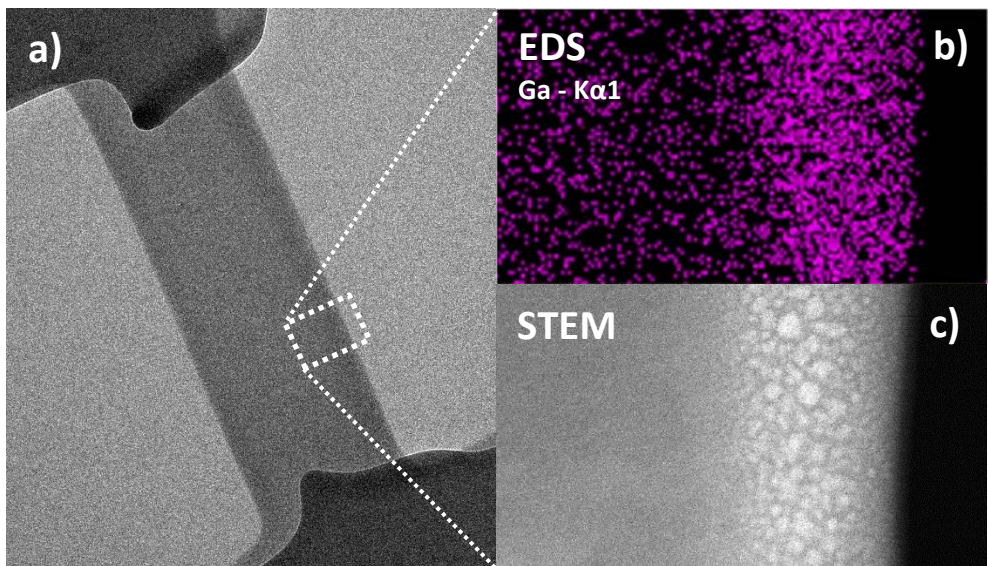


Figure 3.15: a) A general TEM image of a tensile sample and b) an EDS map and c) a STEM image of the sample edge taken from the same location. No Al_2O_3 crystals are detected in the sample before or after the mechanical test. TEM images show contrast changes on both sides of the FIB milled tensile samples, and are revealed gallium (Ga) implantation clusters by combined STEM and EDS mapping. Copyright Erkka J. Frankberg 2017

3.4 *In situ* TEM mechanical testing results

In total 15 coated anvils and 1 tensile sample were successfully tested using three different imaging modes: electron beam ON, electron beam OFF or electron beam ON and switched OFF during the test. **Table 3.1** summarises the tested anvils and the used imaging mode for each anvil.

Table 3.1: A summary of tested samples and the used imaging mode for each sample. In X.Y. coding, X indicates the set of four anvils and Y means the number of the anvil inside the set. Marking “2c” in 6.4 means the second compression data.

Loading mode	<i>In situ</i> samples	Imaging mode
Compression	2.3	Beam ON/OFF
“	3.1 - 3.3 - 5.1 - 5.4 - 6.4 2c - 7.1 - 7.3	Beam ON
“	3.2 - 3.4 - 5.3 - 6.2 - 6.4 - 7.2 - 7.4	Beam OFF
Tension	PTP3	Beam ON

As we conduct the compression/shear tests, the PLD films exhibit permanent plastic deformation, changing the film morphology. Additionally the films can undergo delamination from the sapphire substrate, which needs to be taken into account when analysing the mechanical test results. **Figure 3.16** Shows the mechanical damage in anvil 2.3 after two separate loading. After third consecutive loading, the film is delaminated from the substrate indicated by a characteristic brighter contrast lines.

As an exception to the mechanical tests samples, the sample 2.3 contains two darker dots which are crystals residing in the amorphous matrix. However, as noticed during characterization of freestanding films, the concentration of nanocrystals is very low and none of the anvils we tested contained nanocrystals in the film section located directly at the tip of the anvil. Therefore, the average experimental test results represent the behaviour of a fully amorphous PLD Al_2O_3 structure.

The true stress and engineering strain were calculated using the methodology introduced in chapter 2. With one exception (sample 6.4 2c), all shown test results are taken from the first compression or tensile loading performed on the sample. **Figure 3.17** and **figure 3.18** summarise the results for *in situ* TEM compression/shear tests, with beam switched ON and switched OFF respectively.

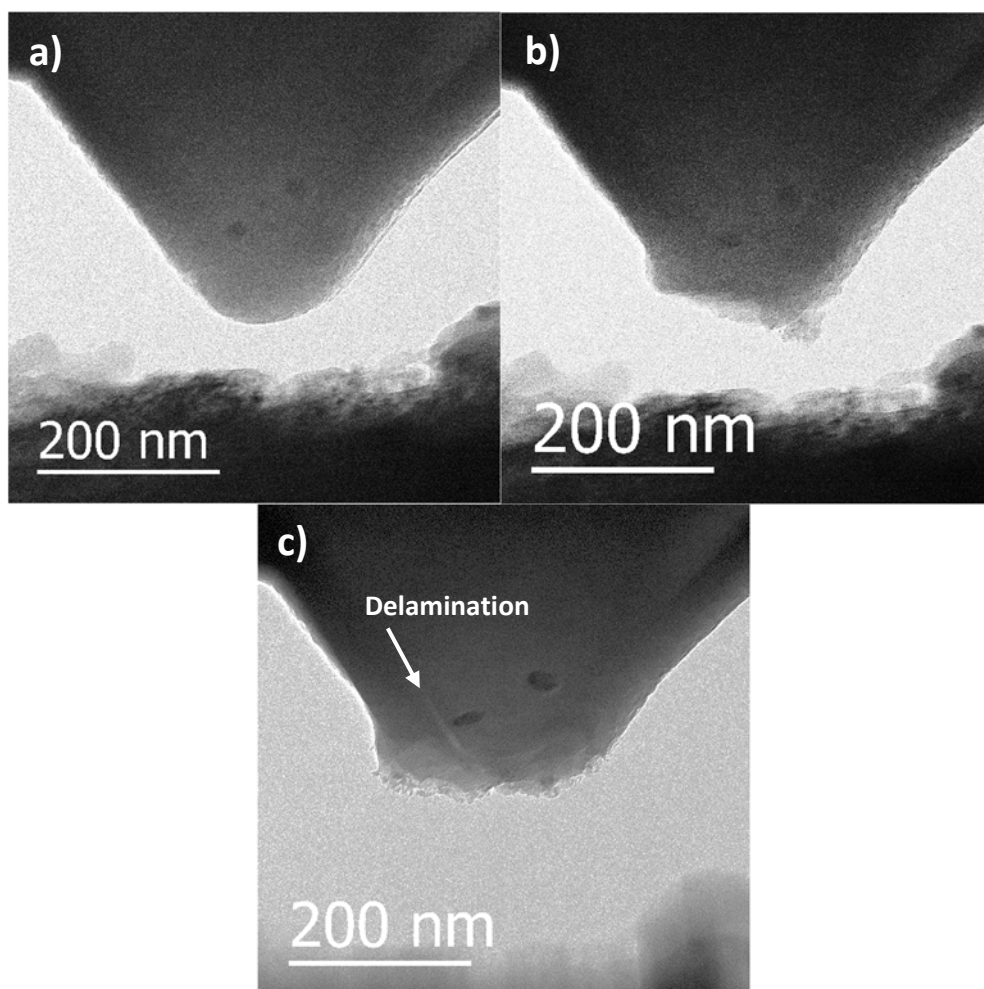


Figure 3.16: Transmission electron microscope image of 2.3 anvil a) aligned before loading and after b) the first and c) the third mechanical loading. After first loading b), the morphology of the tip is permanently changed but no delamination or fracture is detected as no permanent contrast changes occur. c) After the third test, the film is heavily deformed as the thickness of the film has reduced more than 50 % and the film has been delaminated from the sapphire substrate. Still, no fracture of the film is detected by contrast changes characteristic to fracture, nor it is detected in mechanical test data.

The most striking feature in all compression/shear testing results is that we reach the yield stress of amorphous Al_2O_3 between 3.5 – 4.7 GPa. Deformation continues with plastic flow value until we reach 80 - 90 % elongation. Once yielding, the stress values oscillate around a relatively constant average value, indicating that the structure is flowing and no strengthening or weakening of the structure happens, which is likely to happen in amorphous materials when temperature is constant.

During 90 - 100 % elongation, the stress turns gradually back into characteristically elastic response as we reach the sapphire tool and it starts to contribute to the mechanical response of the sample. Once the sapphire tool is reached, the stress increases elastically up to the end of the test, or when the sapphire yield stress is reached or when the maximum force limit of the test device is reached. The maximum elastic stress measured once the sapphire tool was reached was several gigapascals higher than the flow stress of the sample. Therefore, the tool can be thought as fully rigid compared to the sample film. In some samples, the stress also remains almost constant and signals that the amorphous film has delaminated from the sapphire tool.

The average elastic modulus of PLD Al_2O_3 films was around 20 - 30 GPa, which is low compared to literature values of elastic modulus 110 - 204 GPa for dense amorphous Al_2O_3 [9, 76, 97]. The reason for this is believed to be the following: First, the accurate area measurement is a challenge in the early stages of the tests, underlined by the large stress deviation. There are multiple contact points related to the surface roughness of the diamond indenter, and the elastic deformation happens parallel with local plastic yielding. In other words, the early contact stress has both elastic and plastic component mixed together. Secondly, we measure fully amorphous structure leading to lower elastic modulus. Earlier studies use traditional nanoindentation [9, 76, 97], in which the volume of deformation is huge compared to the deformation volume of *in situ* TEM compression/shear tests. Therefore more crystals will contribute, which is measured as higher elastic constant. Finally, the used experimental setup produces of a mixed compression/shear loading mode in which the lower shear modulus will contribute to the measured elastic modulus.

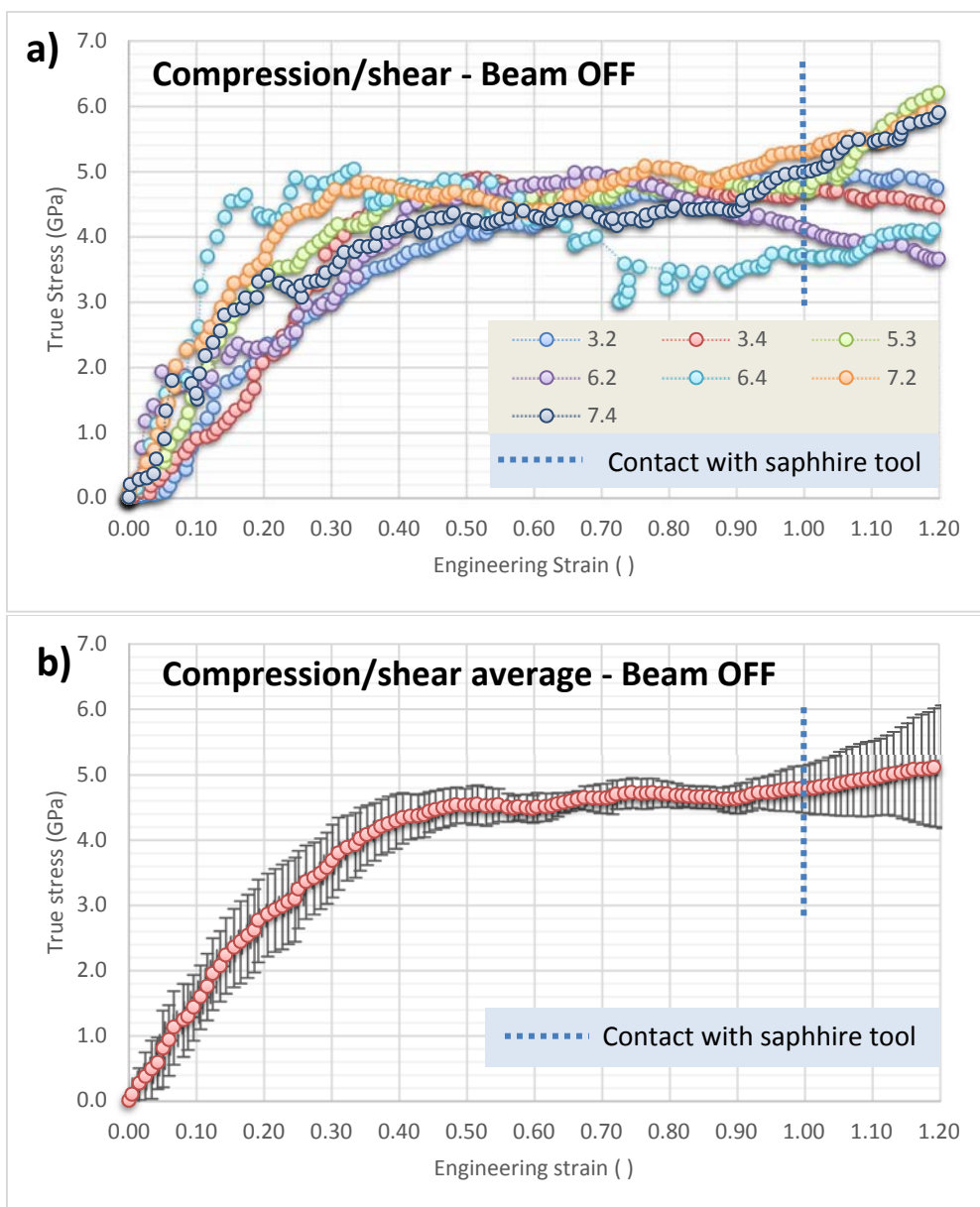


Figure 3.17: Experimental *in situ* TEM compression/shear test results without the effect of electron beam. a) Stress of individual measurements and b) average stress of 6 samples as a function of average strain. Results represent the mechanical properties of fully amorphous Al_2O_3 . 6.4 data points were discarded from average data as they are too far away from data consensus. Capacitive strain calibrated using a known contact point with the sapphire tool. Stress error in standard deviation. Copyright Erkka J. Frankberg 2017

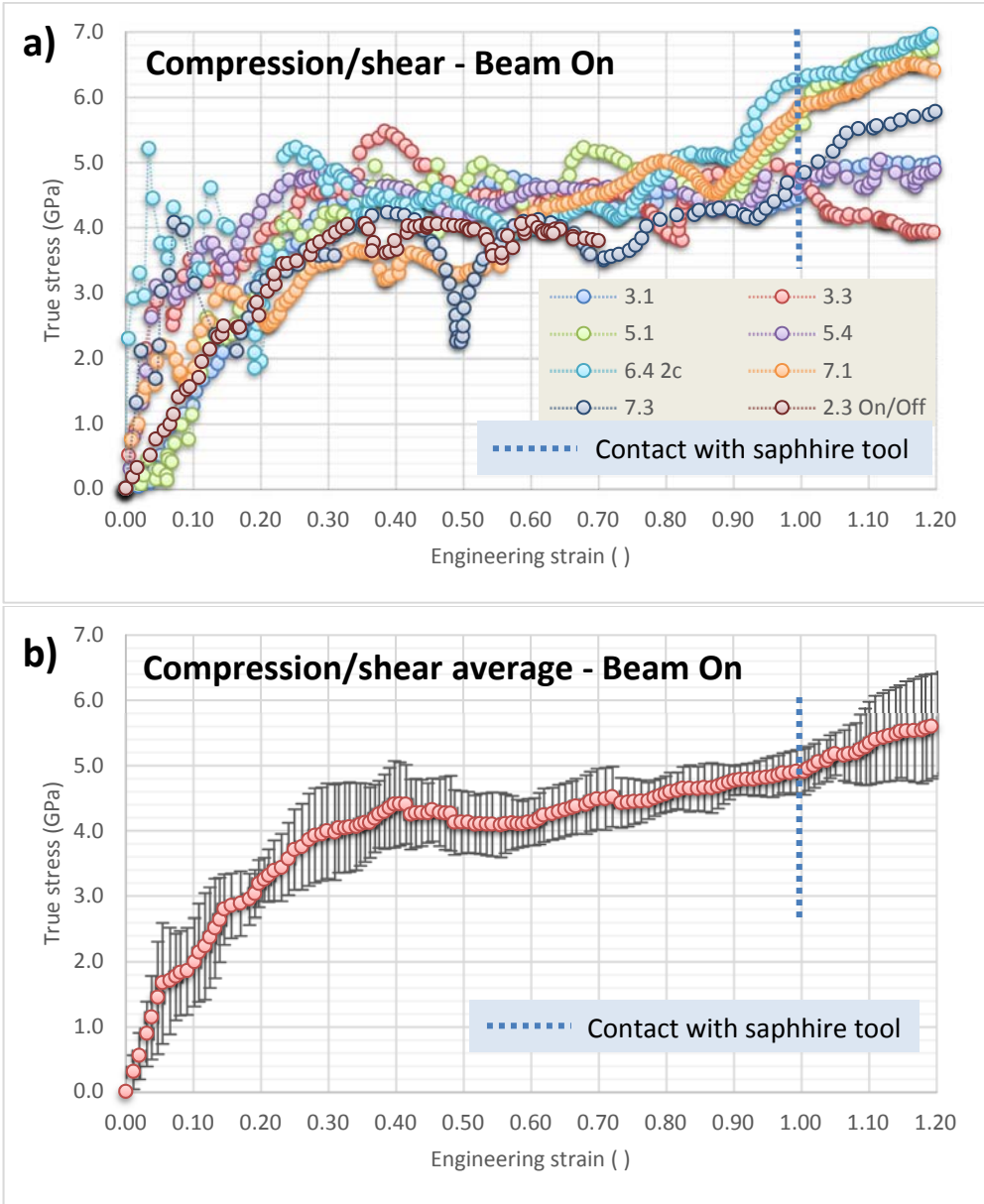


Figure 3.18: Experimental *in situ* TEM compression/shear results including the electron beam effect. a) Stress of individual measurements and b) average stress of 8 samples as a function of average strain. Results represent the mechanical properties of fully amorphous Al_2O_3 . The test were performed under 300 kV electron beam with an average dose of 3.6 nA. 8 % of data points (samples 6.4 2c & 7.3) were discarded from average data. Strain measured using DIC. Stress error in standard deviation. Copyright Erkka J. Frankberg 2017

Comparing the beam ON and beam OFF results, both show a very similar mechanical behaviour. Inside the measurement error of the average results, it seems difficult to notice the effect of electron beam on activation energy or flow stress, if there is one. However, the average beam OFF stress seems to be higher in some parts along the strain.

In compression/shear tests, we had to discard some data from the average calculation, as the deviation is too large from average data. The TEM images after the discarded measurements do not indicate that delamination or fracture induced the divergent data, but is likely caused by errors in aligning the sample and the indenter tool prior testing. The beam OFF strain is reliable as we can calibrate the capacitive measured strain using a known contact point with the sapphire tool below the sample. Therefore, beam OFF results appear smoother overall and almost free of inconsistent data. As a comment, it is quite a challenge to fit the average force data and average DIC strain data together in the compression setup and therefore the corrected capacitive strain data gives more consistent results as a function of stress when calibrated using the known contact point with the stiff anvil tool. Image correlation is still profoundly important to perform in parallel.

Besides the overall mechanical properties, we also observe a strain rate dependant behaviour on the amorphous Al_2O_3 during plastic flow. **Figure 3.19** illustrates the change in yield stress plotted in parallel with the respective engineering strain rate.

The materials response to changing strain rate seems to be a classic viscoplastic response [98]: the flow stress increases with increasing strain rate and decreases with decreasing strain rate. As we have fully amorphous structure, strain hardening observed in **figure 3.19** cannot be explained by dislocation interaction (there are no dislocations!). Instead, the material has a viscous quality leading to changes in stress as a function of strain rate and viscosity of the flowing material dictates proportionality of the stress to strain rate. Later we will discuss in detail of the viscosity of this amorphous solid.

Additionally, a tensile test was performed on a NaCl floated PLD Al_2O_3 film which was further milled using focused ion beam to produce a tensile specimen geometry (see experimental section). **Figure 3.20** illustrates the mechanical behaviour of the film in tension.

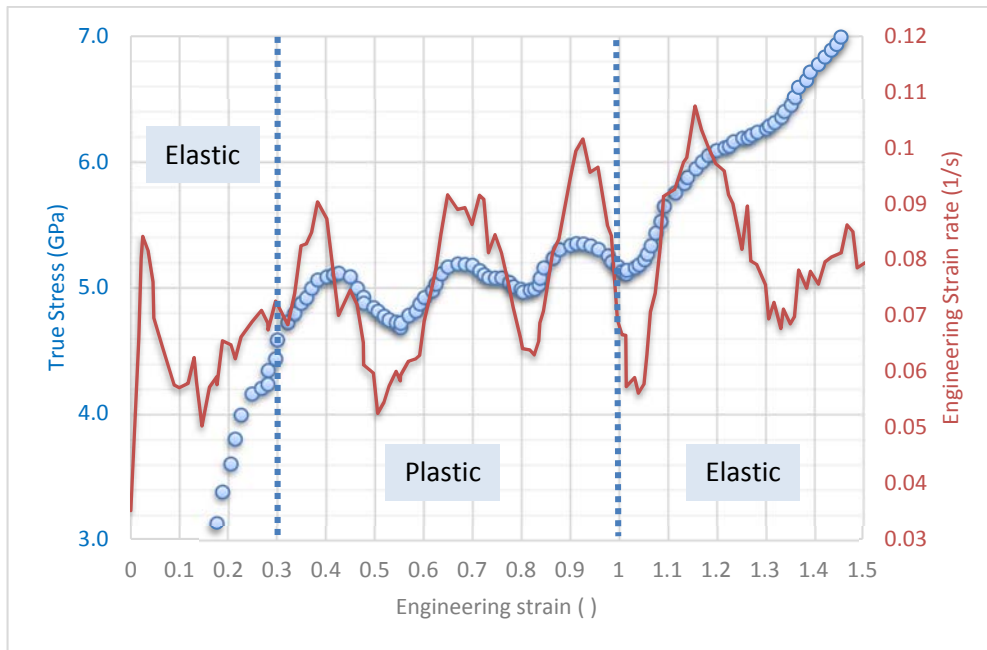


Figure 3.19: Strain rate dependency of the flow stress measured in sample 3.1 (beam ON). Elastic stress builds up until 0.3 strain after which the flow stress is gradually reached. The flow stress fluctuates as a function of strain rate until contact with sapphire tool at roughly 1.0 strain where elastic stress starts to build up again. The strain and strain rate data was measured using DIC and verified with corrected capacitive data and was filtered using the Savitzky-Golay method with 22 points of window and fifth polynomial order using the Origin 8 software. Copyright Erkka J. Frankberg 2017

Again, the most striking feature in tension is that we reach the yield stress of the Al_2O_3 structure after which the structure flows plastically until fracture. The total elongation is approximately 15 %, with around 5 - 10 % of plastic elongation, depending on the interpretation of yield stress. It is typical for a viscoplastic behaviour that a well-defined yield stress is not found [98]. During the “run-in phase” of the test process, the sample film first straightens out before the fully elastic response begins.

The elastic modulus for the tensile test is ≈ 70 GPa, which is more than double to values observed in compression/shear tests and closer to the reported literature values. In tension, the specific cross sectional area and the loading mode is better defined than the area in compression/shear test. Comparing the measurement procedures, it is probable that tensile test gives a better estimation of the elastic modulus of the material.

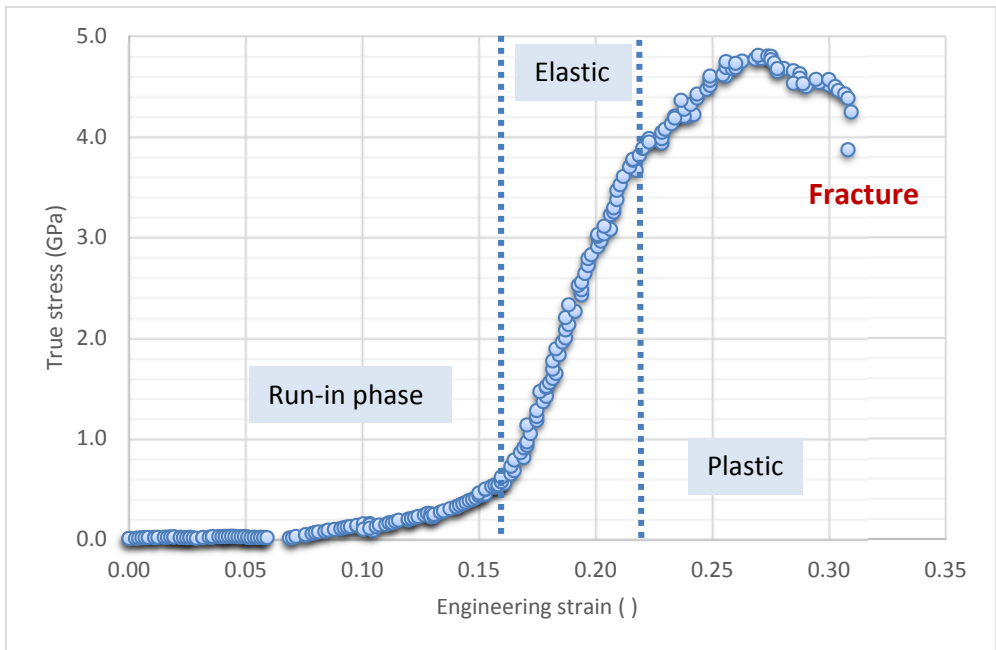


Figure 3.20: Stress as a function of strain in tensile test sample PTP3 of PLD Al_2O_3 . The stress is corrected by removing the average measured spring force ($0.034 \mu\text{N/nm}$) of the push-to-pull device from the raw force measurement data. Results represent a fully amorphous and as-deposited PLD Al_2O_3 structure as no crystals are observed in the deformation volume before or after the test. The film crystallises under a condensed electron beam indicating that it is mostly in the as-deposited state excluding the FIB damaged areas. Strain measured using DIC. The test was performed under 300 kV electron beam with a low electron dose of $0.29 \text{ e}/\text{\AA}^2\text{s}$. Copyright Erkka J. Frankberg 2017

Elastic response is followed by full yielding at a maximum stress of $\approx 4.8 \text{ GPa}$, a level which is similar to the compression/shear tests. Before fracture, we observe a void nucleation and growth in the body of the sample, near to the FIB damaged edge of the sample. The void grows until it reaches the edge of the sample and soon after that, the formed crack becomes unstable and the specimen was fractured. **Figure 3.21** illustrates how the void nucleation happens inside the sample and after some time propagates to the surface while remaining stable. The surface crack extends further until it reaches a critical length and the sample fractures. The nucleated void is stable as it takes 23 seconds with the 1 nm/s nominal tensile pull speed to reach a critical crack length of 135 nm and fracture. Sharply decreasing stress just before fracture signals the reduction of cross-sectional area by crack growth, as it is not compensated in the true stress calculation.

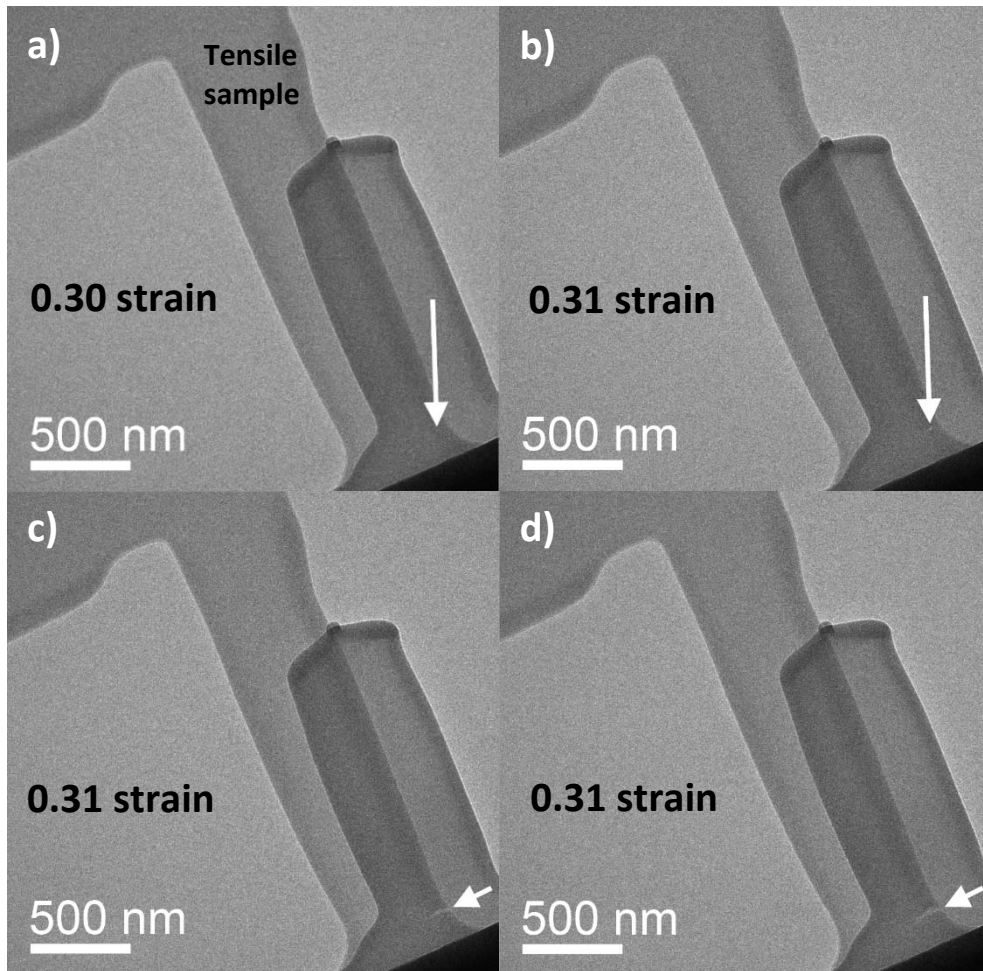


Figure 3.21: bright field transmission electron microscope images of a) void nucleation and b) growth, c) transformation in to a surface crack and d) crack propagation during *in situ* tensile test on sample PTP3. Total strain related to Figure 3.20 is marked in the images. The actual sample overlaps in the image with another piece of the PLD film, which does not contribute to the test results. Copyright Erkka J. Frankberg 2017

We believe that the root cause for the void formation is in the focused ion beam based sample preparation of the tensile specimen. As shown in the characterization results, the ion beam caused defects and ion implantation near the beamed areas of the tensile specimen. When our PLD Al_2O_3 sample is plastically elongated, these defects start to coalesce until big enough to form a detectable void. The relatively large and circular void becomes thermodynamically more stable compared to the other smaller void-like defects around it, and as deformation

continues, the void continues to grow and consume defects around it. **Figure 3.22** shows a STEM image of the tensile specimen with a location of the void nucleation in the FIB damaged area. The void nucleation location is inside the FIB defected zone, which supports our hypothesis. It is possible that when using a fully as-deposited sample, the plastic strain before fracture could be larger.

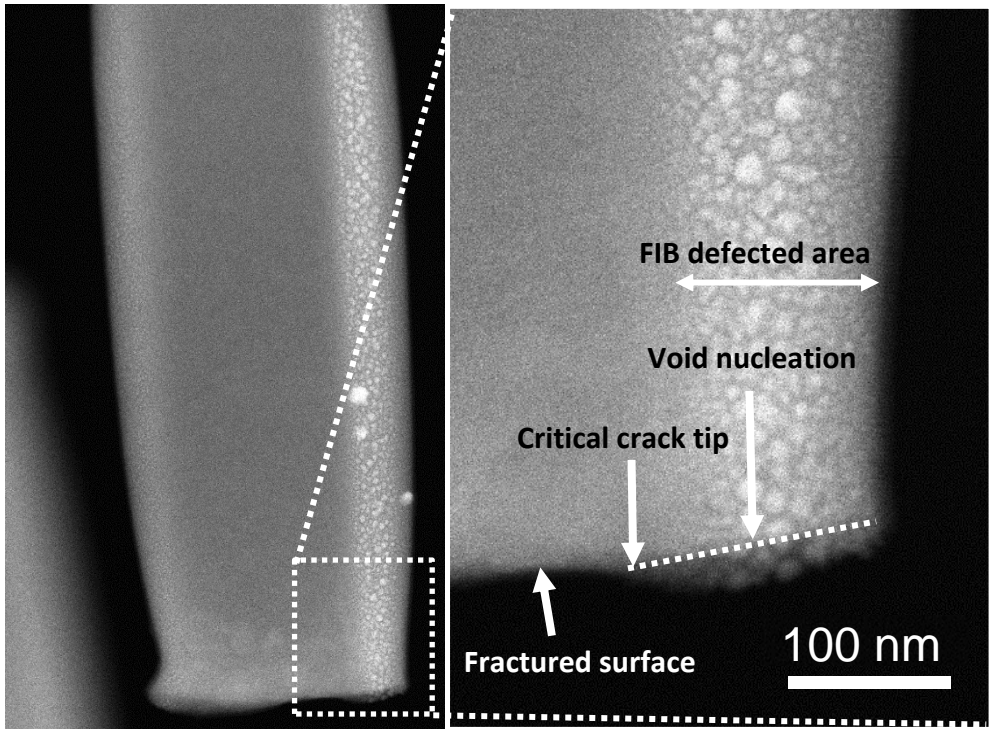


Figure 3.22: STEM image of the fractured tensile sample PTP3 and an insert showing the area where the void nucleated and transformed into a surface crack that led to fracture. Copyright Erkka J. Frankberg 2017

By measuring the crack dimensions, we can estimate the critical stress intensity factor for amorphous Al_2O_3 with the 135 nm crack length and highest measured stress value using the Griffith criterion

$$K_{Ic} = \sigma\sqrt{\pi c} = 4800 \text{ MPa} \sqrt{3.14 * 135 * 10^{-9} \text{ m}} = 3.1 \text{ MPa} \cdot \text{m}^{1/2}$$

Surprisingly the measured K_{Ic} is well aligned with the typically measured critical stress intensity factors for Al_2O_3 $K_{Ic} = 2.0 - 6.0 \text{ MPa} \cdot \text{m}^{1/2}$ [1]. This gives a following thought: Our sample material is still as brittle as bulk Al_2O_3 normally is, but as the

geometry and the flaw size are extremely small, the stress level can rise to a level in which diffusion can activate by the gradient stress field at room temperature. When the plastic deformation mechanism finally activates, the crack nucleation and growth becomes more difficult and the material would exhibit increased “toughness” or resistance to cracking. Again, the crack in our PTP3 experiment is believed to nucleate by external reasons and a crack nucleation might not be possible at all in a sample “au naturel”.

In summary, the combined experimental results show that pulsed laser deposited Al_2O_3 can plastically deform up to 15 - 100 % total elongation without fracture depending on loading geometry. The results are quite unexpected for Al_2O_3 at room temperature and at zero confining hydrostatic pressure. Especially in the light of the broad literature study regarding the mechanical properties of Al_2O_3 and the mechanical properties of ceramic and glass materials in general.

Next, we will discuss the theory and mechanisms behind this exotic mechanical behaviour. To challenge the experimental results we created a molecular dynamic simulation model to give an independent quantification for the mechanical properties of PLD Al_2O_3 .

3.5 Simulated mechanical properties of amorphous Al_2O_3

Molecular dynamic simulation results are presented in **figure 3.23**, in compression and in tension.

First regarding the simulation results, we confirm the yielding of bulk amorphous Al_2O_3 structure at a critical yield stress, in both compression and tension as shown in **figure 3.23**. In compression, after reaching the flow stress, the stress value oscillates around a relatively constant value, but here the manner and reasons for the oscillation are different compared to experimental results, as the strain rate is forced to be constant during each simulation. In tension, we see also oscillation of stress but now the flow stress has a decreasing trend towards higher strain.

When we increase the strain rate, we observe similar strain rate dependent increase in the flow stress as we see for the experimental tests. This signals that the material exhibits a viscous behaviour during yielding which means that an increase in strain rate will cause increase in stress and vice versa.

The simulated elastic modulus or Young's modulus for compression and tension is approximately 94 GPa respectively, which is higher than experimentally measured compression/shear 20 - 30 GPa and tension 70 GPa. However, as noted earlier, there might be several reasons for the difference between the elastic moduli, such as the difficulty of accurate determination of the contact area during the early stage (0 – 0.1 strain) in the experimental tests. We see the simulated moduli as more ideal representation of the elastic properties of fully amorphous Al_2O_3 . This is evidenced for example by the closer correlation of tensile modulus in experimental and simulations compared to compression/shear tests.

The literature elastic modulus for dense amorphous Al_2O_3 (110 - 204 GPa [9, 76, 97]) are reasonably close to the simulated values. We point out that the literature results are obtained using conventional nanoindentation in which the deformation volume is relatively large and likely to contain gamma phase crystals increasing the measured elastic modulus of the film.

We can then show a direct comparison of computed and experimental mechanical data. In **figure 3.24**, we plot the experimental “beam OFF” data with simulated compression test data and in **figure 3.25**, we plot the experimental tensile test data with simulated tensile data. The combined results rise mainly two questions: First, why do we have a large difference in the elastic modulus in the compression results and second, why do we measure a very similar flow stress values when even the lowest difference in simulated and experimental strain rate has a magnitude of 10^8 ?

First, the Matsui interaction potential has been shown to give a good correlation to bulk modulus values of alpha Al_2O_3 compared to experimental values [86]. Regarding elastic modulus of amorphous Al_2O_3 , we believe that the difference in experimental and simulated values comes from the used experimental setups. Particularly in experimental compression, we likely measure a mixed compression and shear modulus rather than pure Young's modulus measured in the compression simulations. Hooke's law relates the shear modulus to Young's modulus by $G = E/2(1 + \nu)$, where ν is the Poisson's ration, which gives theoretical $G \approx 36 \text{ GPa}$, for $E = 94 \text{ GPa}$ and $\nu = 0.3$. The probable fact that we measure partly shear properties during the compression/shear tests will enable us to use definition of shear viscosity when we discuss about the mechanisms of plastic deformation in chapter 3.9.

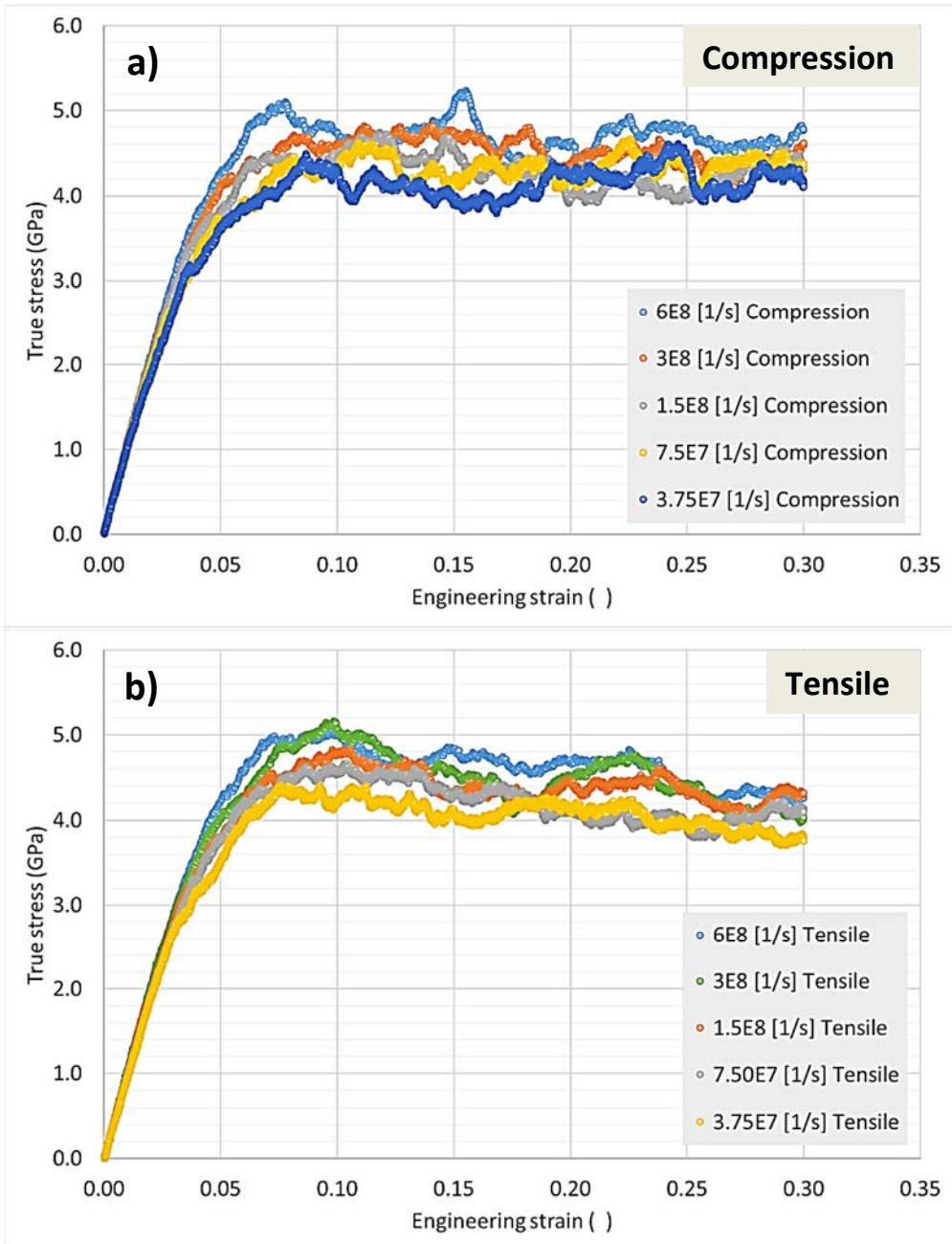


Figure 3.23: Simulated mechanical properties of fully amorphous Al_2O_3 film. Stress as a function of strain a) in compression with varying strain rates and b) in tension with varying strain rates. Lateral confining “hydrostatic” pressure was kept at 1 atm. and each data point is an average of 3 independent measurements. Copyright Erkkka J. Frankberg 2017

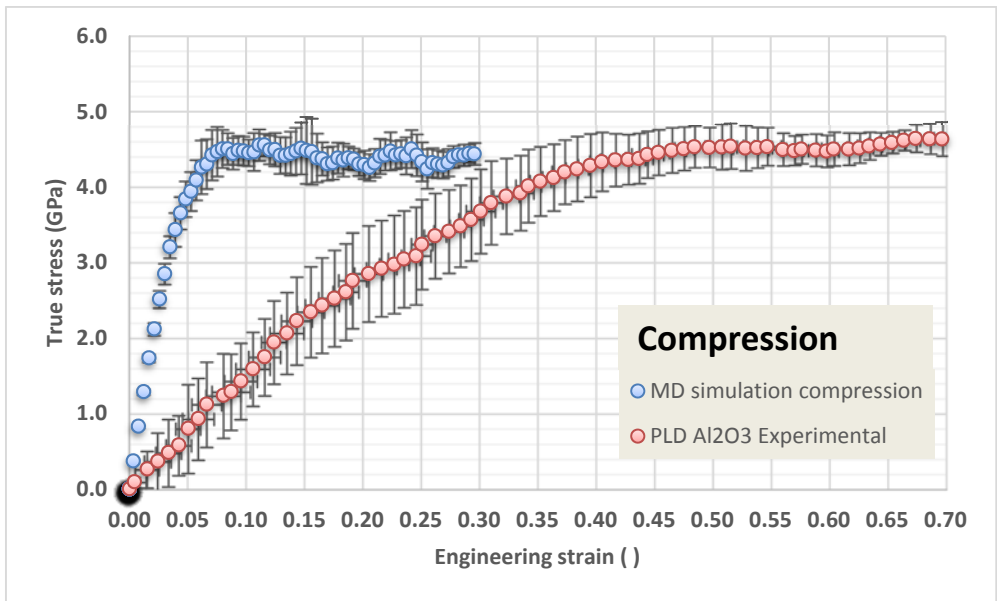


Figure 3.24: Average simulated compression (blue) and average experimental (red) “beam OFF” compression/shear stress data as a function of average strain. Stress error bars are calculated using standard deviation. Copyright Erkka J. Frankberg 2017

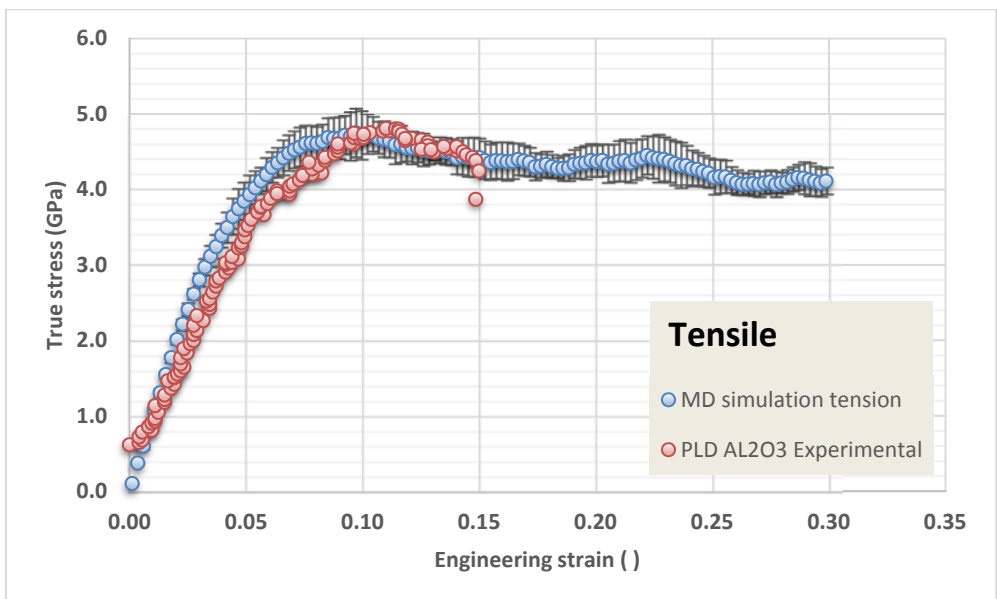


Figure 3.25: Average simulated (blue) and experimental (red) tensile stress data (sample PTP3) as a function of average strain. Stress error bars are calculated using standard deviation. Copyright Erkka J. Frankberg 2017

The relatively low flow stress in simulation is connected to the lower average activation energy obtained in the simulations. Lower activation energy is directly linked to the flow stress as we propose later on. The reason for a lower activation energy might be linked to the fact that the stress field is unrealistically uniform in the simulations using small simulation volume and periodic boundary conditions. Another point of view is that if we assume that plastic deformation requires breaking ion bonds and forming new ones, then one could argue that the maximum flow stress should be limited by the characteristic ionic bond strength of Al_2O_3 and therefore the increase in flow stress even at much higher strain rates would be limited.

Later on, we also show that viscosity of the material decreases as a function of strain rate. This will have negative effect on the increase of flow stress while strain rate is substantially increased in the simulations compared to experiments. On the other hand, even if the increase of flow stress decreases with increasing strain rate, the flow stress in simulations is still lower than was expected.

Fact that we are able to confirm experimentally that yielding and plastic flow occurs in amorphous Al_2O_3 , opens up the opportunity to simulate plasticity of other amorphous ceramics. Before experimental results confirmed it, it would have been easy to ignore plastic behaviour in atomistic simulations!

Summarising, the atomistic simulations show that a melt quenched bulk amorphous Al_2O_3 with equilibrium structure and without impurities can yield plastically at least up to 30 % strain in pure compression and pure tension. The combined experimental and simulation results give strong grounds to discuss the mechanism causing the plastic deformation behaviour of the amorphous Al_2O_3 structure at room temperature and without confining hydrostatic pressure.

3.6 Plastic deformation of amorphous aluminium oxide

In the introduction, we concluded that plastic deformation of oxide structures is previously reported to happen mainly under special conditions (excluding a simple hardness test). In this chapter we summarize the main evidence indicating that room temperature plastic deformation really exists in pulsed laser deposited amorphous aluminium oxide.

First evidence that plastic deformation occurs in the PLD Al_2O_3 film during mechanical loading is given by the creation of permanent residual indentation on

the film, seen after each test. **Figure 3.26** shows a coated anvil prior and after compression/shear test. In **figure 2.10**, the area under the raw force/displacement data curve represents the plastic deformation work done to the sample.

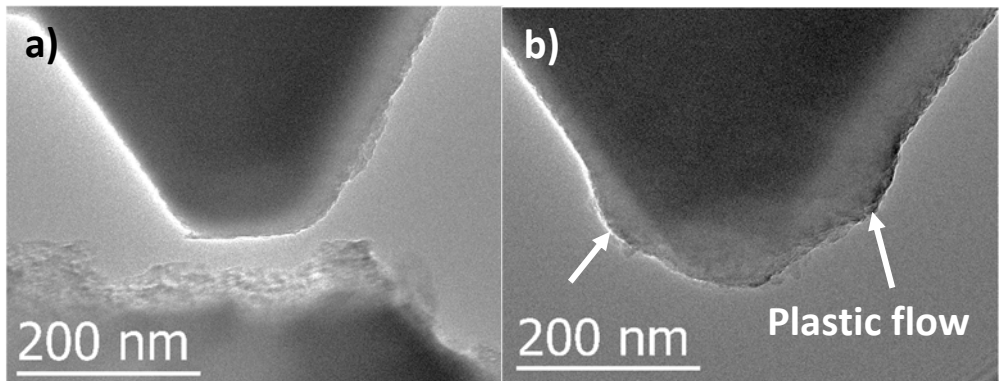


Figure 3.26: TEM images of sample 7.4 a) prior and b) after a compression/shear test showing the permanent changes in dimensions and morphology of the sample tip. Compression/shear test was conducted without electron beam and no fracture or delamination is detected in the data or in the TEM images. Copyright Erkka J. Frankberg 2017

Permanent shape change also occurs in the tensile specimen as we measure permanent elongation and reduction of the width of the sample. **Figure 3.27** shows the sample at onset of full elastic response and at directly after fracture.

Second evidence in favour of plastic deformation are the combined mechanical data from experimental tests and atomistic simulations in **figures 3.24** and **3.25**: The elastic response is followed by a yield stress, after which the material flows with nearly a constant average stress up to 15 - 100 % total strain. In all cases, the strain until fracture is at least two orders of magnitude higher than expected for ceramic and glass structures, which normally fracture with < 0.1 % of total elastic strain [1].

This signals that the geometrical defects in the films are very small, which allows to build up large stress needed to activate the diffusion creep mechanisms. We know that the elastic flexibility increases substantially in smaller structures compared to macroscale such as in nanostructured silicon [99] and silicon carbide fibres. However, it is not yet acknowledged that scaling down could also activate plastic deformation of amorphous ceramics at low temperature.

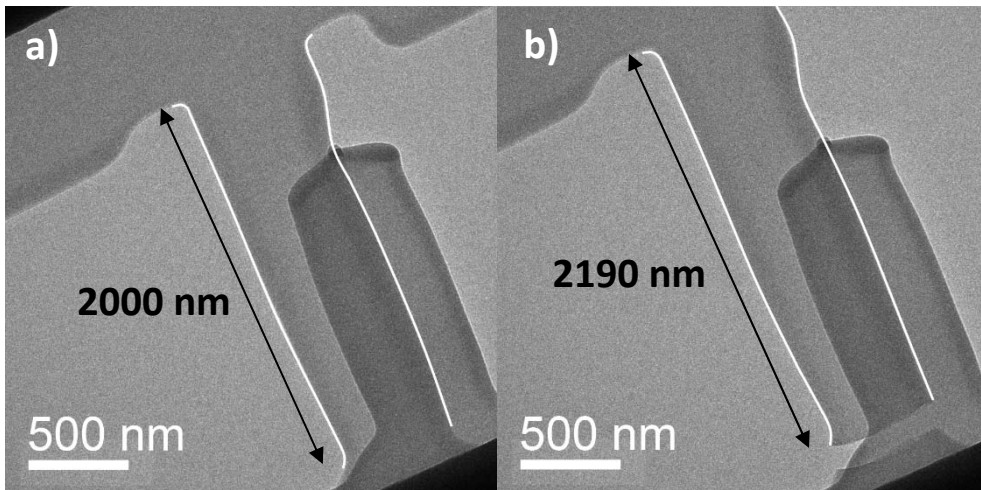


Figure 3.27: a) Tensile test sample PTP3 at the onset of full elastic response (total strain 0.165) and b) 0.1 s after fracture showing the permanent changes in length of the tensile sample. White lines outline the sample under tension in images a) and b). The test was performed under 300 kV electron beam with an electron dose of $0.29 \text{ e}/\text{\AA}^2\text{s}$ and 10 000x nominal magnification. Copyright Erkka J. Frankberg 2017

Based on the earlier literature review, we can conclude that all main plastic deformation mechanisms for solids can be hypothetically possible when a substantially high stress (e.g. order of magnitude $E/10$ -100) can be introduced without fracture. However, according to our observation of plastic deformation, the amorphous Al_2O_3 appears to undergo viscous flow, or more precisely viscous creep as the flow of the material seems to activate only by applying a sufficient stress level. In other words, the material undergoes a transition from a solid to a liquid-like phase once subjected to a critical stress, which acts as an external driving force for surface and bulk diffusion.

The following evidence are in favour of the proposed creep flow mechanism: First, the deforming volume in all samples appear free of crystals, which blocks the possibility of dislocation nucleation and motion. We also do not detect any significant contrast changes in the samples during plastic deformation, which could indicate low energy diffusion paths such as dislocations, shear bands or grain boundaries along the material. This fortifies the assumption that the main available mechanism for mass transfer is via bulk and surface diffusion. As the temperature is near room temperature at the beginning of the tests and remains low up to yield stress, the main (external) energy source for activating diffusional flow will be the stress gradient between sample parts under low and high stress.

Secondly, the deformation and failure happens without clear necking in the tensile test observations, which is characteristic to viscous flow in, for example, glass fiber drawing process [18]. Thirdly, the flow stress after yielding remains relatively constant and changes as a function of strain rate in a manner that is expected if the material flows viscously. Finally, to prove that diffusion is active in these structures, we are able to image surface diffusion happening in-situ in TEM on the surface of amorphous Al_2O_3 showing that the mechanism is active when sufficient driving energy is available.

Surface diffusion during plastic elongation was imaged during rare spontaneous ruptures of the film during TEM characterization, which were caused by charging effects of the non-conductive Al_2O_3 film. This offers direct qualitative evidence of surface diffusion happening during plastic deformation as we can record ion movement on the material surfaces. **Figure 3.28** shows the nanometer-scale diffusion mechanisms occurring during spontaneous tensile elongation and rupture of a few nanometer wide isthmus of PLD Al_2O_3 .

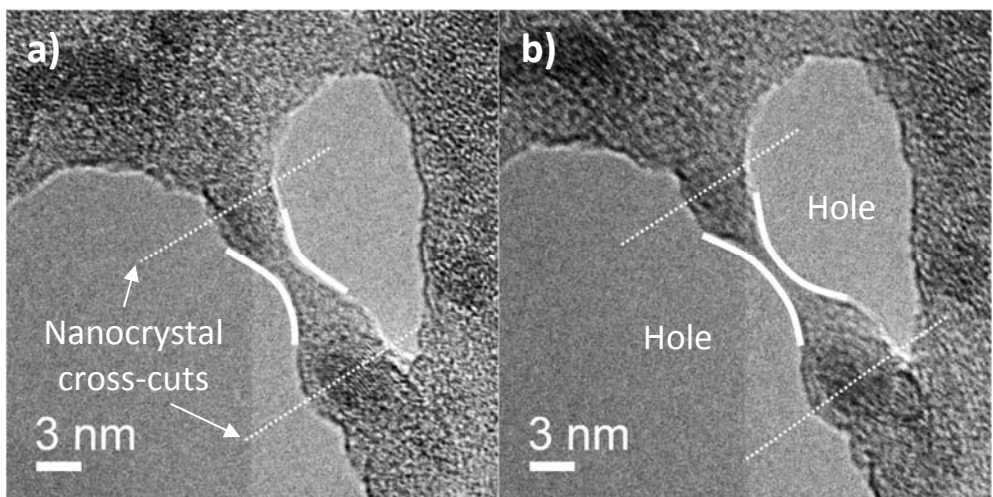


Figure 3.28: *In situ* transmission electron microscopy images of surface diffusion mediated tensile plastic deformation of amorphous PLD Al_2O_3 matrix. a) Two nanocrystals surrounded by an amorphous matrix being pulled apart by charging effects b) image just before fracture, where the thickness of the thinnest section is approximately 7 Å with a total elongation of approximately 13 % between images a) and b) during 9 seconds, measured from the centre of the nanocrystals indicated by dashed white lines. Observations done under 200 kV electron beam. Copyright Erkka J. Frankberg 2016

Here the fracture literally happens only after there are no more ions (bear in mind that the smallest stable structure is Al_2O_3) to hold the structure intact as the

thickness of the tensile “specimen” is approximately 7 Å just before rupture. After the rupture, the elongated amorphous shape rounds back to a spherical granule, clearly indicating active surface diffusion in this small scale. Spontaneous ruptures were observed at wide range of scales, from 1 nm to 100 nm size range and respectively varying electron doses. Observed areas contain nanocrystals and therefore do not crystallize further during imaging using a condensed electron beam.

It is worth noting that all liquids (even water) have an elastic response before viscous flow occurs. That is why falling to water at high speed can be lethal or at least give a nasty bruise during a plunge to the swimming pool. Therefore, it seems plausible that even more rigid amorphous materials could flow under sufficient stress to overcome the elastic response. This is of course, if flaw size is small enough for the Griffith criterion to allow sufficiently high stress without fracture. There are several rightful criticisms presented against viscous flow of amorphous solids below glass transition temperature [61, 62, 63]. But they all look at the problem through self-diffusion, in other words with a notion that flow happens under low stress, close to the solids own gravity, which is logical only for liquids, meaning materials at or beyond melting temperature.

We fully acknowledge that our sample is a pure solid under its own gravity and will not spontaneously flow. Instead, our results suggest that mechanical energy can be used to activate diffusion in similar manner as thermal energy does. We claim that the glass transition temperature or equivalent energy level can also be reached by sufficient external mechanical energy. This would render the amorphous solid into a liquid-like substance, which re-solidifies immediately after the load is released or a fracture occurs. This would also suggest that we should be able to measure the viscosity of the material during the liquid-like deformation. This issue will be discussed later in detail with results.

Meanwhile, criticisms can also be presented against the current results on plastic deformation and next we will discuss the main accusations related to the evidence presented showing the plastic deformation phenomena in our ceramic thin film and mechanism by which the plasticity occurs.

3.7 Discussion on the mechanical behaviour of amorphous Al_2O_3

Here we summarize and discuss the effects that may influence the mechanical behaviour of the PLD Al_2O_3 during experimental studies and therefore lead to non-

perfect conclusions regarding the results. Most pressing criticism is related to whether the plasticity is caused by an external reason and would not be observed in ambient conditions.

First and most pressing criticism is if the electron beam in TEM is the root cause of the plastic deformation and no plasticity can be found outside the beam. This seems to be the current opinion regarding *in situ* TEM mechanical tests done to amorphous SiO₂ nanostructures [11, 83]. Two mechanisms have been suggested that could promote plasticity under an electron beam: heating of the whole sample or promoting local bond rearrangement and diffusion without heating the whole sample.

At least two authors [71, 95] have considered heating of amorphous Al₂O₃ thin films by electron beam irradiation in TEM. Although Murray *et al.* consider heating to be the main cause for crystallization of their amorphous Al₂O₃ films [95], Nakamura *et al.* demonstrate and summarise that the temperature increase in amorphous Al₂O₃ is limited and cannot induce phase transformation from amorphous Al₂O₃ to gamma phase Al₂O₃ [71]. They show that theoretically, the temperature increase from room temperature is around 6 Kelvins for a 200 kV beam, which is very low compared to 873 - 973 K needed to thermally anneal fully amorphous Al₂O₃ into gamma phase Al₂O₃ [60, 75].

Additionally Nakamura *et al.* [71] report that indium (bulk melting point 429 K = 156 °C) nanoparticles placed on top of an amorphous Al₂O₃ film do not coalesce by melting during irradiation of 200 kV beam in TEM. Note that nanoparticles have substantially lower melting temperature compared to bulk materials [114]. We can compare the theoretical maximum increase of temperature during our *in situ* TEM tests by using the same formulation that Nakamura *et al.* used. The maximum temperature increase

$$T_{\max} = W_0[1 + 2 \ln(R/r_0)]/4\pi l_0 k \quad , \quad (3.1)$$

where R [m] is the radius of the sample holder grid hole in which the sample is held, r_0 [m] is the radius of the irradiated region, l_0 [m] is the sample film thickness, k [Wm⁻¹K⁻²] is the thermal conductivity of the sample film and the total absorbed power [J] of the electron beam is

$$W_0 = \phi V \rho_0 r_0^2 \quad , \quad (3.2)$$

where φ [] is the fraction of energy absorbed from the electron beam, V [V] is the acceleration voltage, ρ_0 [A/m²] is the beam current density. **Table 3.2** shows the comparison between theoretical maximum temperature increase during the TEM imaging in Nakamura *et al.* [71] and current study during *in situ* mechanical compression/shear.

Table 3.2: Maximum temperature reached by electron beam irradiation in amorphous Al₂O₃ during TEM observations and during *in situ* TEM compression/shear tests.

	Nakamura <i>et al.</i>	Current study	Remarks to current study
R [m]	$6.4 * 10^{-5}$	$2.0 * 10^{-3}$	Distance to heat sink
r_0 [m]	$200 * 10^{-9}$	$500 * 10^{-9}$	Measured from TEM images
l_0 [m]	$15 * 10^{-9}$	$500 * 10^{-9}$	Anvil tool under the film is thick
k [Wm ⁻¹ K ⁻¹]	1.6	1.6	Sapphire tool has even higher k
φ []	0.01	0.01	Fraction of energy absorbed
V [V]	$2 * 10^6$	$3 * 10^6$	We used 300 kV beam
ρ_0 [A/m ²]	600	4545.5	$I/\pi r_0^2$
I [A]	$7.5 * 10^{-11}$	$3.6 * 10^{-9}$	Electron beam current
W_0 [J]	$1.50 * 10^{-7}$	$2.23 * 10^{-6}$	Exposed in a 75/360 ° sector
T_{max} [K]	6	5	

As the heat is additionally conducted away by the diamond indenter during contact with sample film, we can summarize that the plasticity is probably not caused by a bulk heating effect during our *in situ* TEM mechanical tests. Additionally during the beam OFF tests, possible heating happens only during alignment of the sample.

Then what about local diffusion? The TEM beam irradiation has been shown to cause local atomic rearrangements and crystallization of the amorphous Al₂O₃ film [71, 95]. The rearrangements of Al - O bonds are likely to cause the crystallization [71] and it seems plausible that the local rearrangement could also promote diffusion mediated plastic deformation. Could this effect fully cause the plasticity phenomena, or put in reverse, without it there is no plasticity?

To confirm that a local beam effect exists, we also observe that TEM electron beam can cause significant dynamism in the thin films, to our observation especially by surface diffusion detected *in situ*. The atomic rearrangement also happen in the bulk as we detect the collapse of the amorphous structure into gamma phase Al₂O₃ when a critical beam intensity is applied to the as-deposited film (**Figure 3.2**).

As an example, we can show that the concentrated electron beam causes the surface atoms of the amorphous phase to diffuse which causes local Ostwald ripening (=fusion), of small amorphous granules in the amorphous Al_2O_3 film. **Figure 3.29** shows *in situ* Ostwald ripening of a smaller amorphous granule into the nearest larger granule under 200 kV electron beam. Crystalline parts of the granules do not seem to fuse under the electron beam, as is also shown earlier [73], but we also witness that the existing crystals can further grow by succumbing the amorphous phase around them under condensed electron beam.

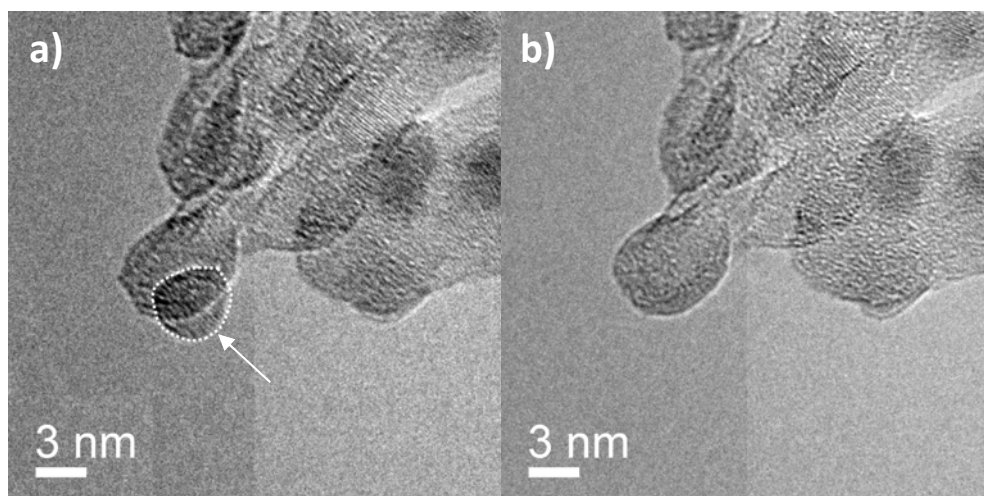


Figure 3.29: *In situ* observation of local surface diffusion activated by electron beam in amorphous Al_2O_3 structure, leading to Ostwald ripening; a) flux of ions from smaller (circled) to larger granule leading to b) full removal of the smaller granule by visible diffusion 8 second later. Copyright Erkkä J. Frankberg 2016

The local promotion of diffusion effect was raised as a main aspect in the studies on amorphous SiO_2 nanostructures to explain the observed plasticity as no plasticity was observed outside the beam [11, 83]. The effect explaining plastic deformation is that the rearrangement and diffusion of surface atoms can blunt the nucleating surface flaws of the otherwise fully fragile material. As the forming crevices are always thermodynamically less stable compared to flat parts of the film, leading to flow of atoms in to the crevice if sufficient activation energy is given. **Figure 3.30** visualizes the relative thermodynamic stability of surface structures. This aspect is very familiar in the sintering theory regarding powder processing [38]. Blunting the nucleating surface flaws that could cause breakage already during the elastic strain could be the reason for reaching high enough stress to activate plastic deformation.

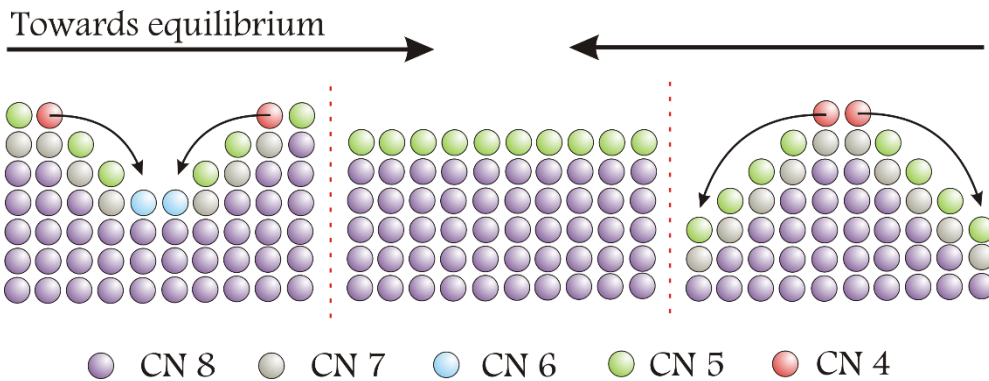
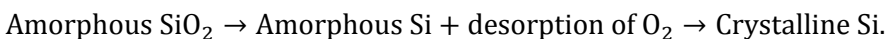


Figure 3.30: Thermodynamic equilibrium of surface structures. Under sufficient activation energy, ions with lower coordination number (CN) diffuse in order to increase coordination and the resulting flux of ions acts to level sharp geometrical shapes. Copyright Erkka J. Frankberg 2017

However, this is opposed by two facts. First, we were able to fracture the material during electron beam exposure in the tensile test (after activating the plastic deformation). Secondly, we were not able to fracture any of the compression/shear samples tested without electron beam. The nucleation of the void in our tensile test sample was likely caused by the FIB preparation, but its evolution into a surface flaw and growth should have been stopped by the increased surface diffusion as electron beam was ON during the experiment.

If the local atomic rearrangement would be causing the plasticity, we should observe a brittle behaviour in all tests done without electron beam. As this is not the case, we can assume that the local rearrangement can only lower the average activation energy, which should lead to a lower tension needed to deform the sample. In light of our experimental and simulation results, it is highly unlikely that the plasticity would be possible only under the electron beam. Instead, for amorphous SiO₂ there could be other factors explaining the results. For example, it is known that electron excitation causes various different structural changes in amorphous SiO₂ and following transformation occur under 200 kV electron beam [71]



Transformation from oxide to a semiconductor metal will likely change the diffusion and deformation properties of the amorphous SiO₂ significantly. In amorphous Al₂O₃, no reduction to metallic aluminium has been detected under electron beam

[71]. Therefore, a direct comparison of amorphous Al_2O_3 to amorphous SiO_2 properties under electron beam is difficult if not arguably pointless and the results on SiO_2 are not directly valid for other amorphous oxides. Seems that when conducting *in situ* TEM experiments with SiO_2 [83], one should pay extra attention on the role of the electron beam for example during beam ON – beam OFF type of tests.

Based on the discussion, it seems unlikely that plastic deformation of amorphous Al_2O_3 nanostructures is limited to TEM observations, but as we do see increased surface and bulk diffusion under condensed electron beams, whenever possible, any experimental done *in situ* in an electron microscope should also be performed also without electron beam to rule out the significance of the effect. Finally, to test the electron beam effect *in situ*, we performed a compression/shear test where we switched the electron beam OFF during the plastic deformation. **Figure 3.31** shows the stress as a function of strain for a compression/shear test done using beam ON/OFF technique.

We detected no fracture or delamination after beam switch-OFF, as also evident in the shown data. Immediately after switch-OFF, we observe a small (0.1 GPa) upward shift in true stress. However, soon after the switch-OFF, the film seems to continue yielding with approximately equal yield stress despite of the beam switch-OFF. The strain rate sensitivity of flow stress is observable, and during the beam switch-OFF event the stress follows strain rate. The dynamic strain rate can also fully account the changes in stress for plastic flow in the experiment and during switch-OFF event.

Another phenomenon that could lead to heating of the material, and cause the yielding, is called “adiabatic heating” which is a natural part of plastic deformation. According to studies mostly relying on steel research, approximately 60 – 95 % of the work used for the plastic deformation dissipates away as heat [100]. Work of plastic deformation, and therefore the available work for adiabatic heating can be described as

$$W_{\text{plastic}} = W_{\text{total}} - W_{\text{elastic}} \quad , \quad (3.3)$$

where W_{total} is the total work of deformation and W_{elastic} is the elastic work done. In adiabatic heating, the work of plastic deformation generates heat faster than it is conducted away, leading to increase in the temperature of the deforming material.

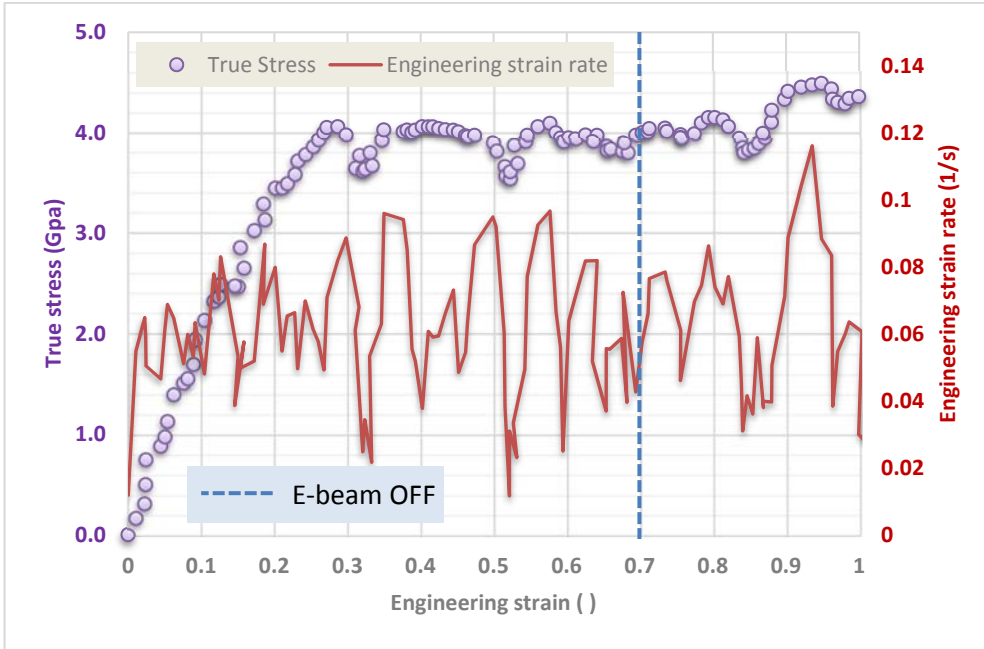


Figure 3.31: “Electron beam ON/Electron beam OFF” -test done in compression/shear to an amorphous Al_2O_3 sample 2.3. The dashed line points out the switch-OFF event. The strain and strain rate data is drawn using corrected capacitive measurement. Strain rate data was filtered using the Savitzky-Golay method with 22 points of window and fifth polynomial order using the Origin 8 software. Copyright Erkka J. Frankberg 2017

It is very likely that the sample will heat up during plastic deformation due to extremely high stress levels, but the main question is would this phenomena be able to initiate plastic deformation? The answer is simply no, as the elastic deformation prior to plastic deformation includes little (in ideal case zero) energy dissipation as heat. Therefore, at the yield stress, the sample is still at room temperature if it has not been heated up by other external heat sources. Nevertheless, it is possible that the heating during plastic deformation will lower the overall flow stress, caused by a local softening along the deformed volume.

A simple calculation gives the order of magnitude for the potential adiabatic heating in a solid [100].

$$\Delta T = \frac{\beta}{\rho C} \int_0^\epsilon \sigma d\epsilon \quad , \quad (3.4)$$

where β is the Taylor-Quinney factor (factor by which plastic work is transformed into heat), ρ is the density of the solid, C is the heat capacity, ε is the strain and σ is the stress. We can assume that at room temperature, $\beta = 0.6 - 0.95$, $\rho = 3325 \text{ kg/m}^3$, $C = 72.3 \text{ J/mol} \cdot \text{K}$ ($T = 273.15 \text{ K}$, $\alpha - \text{Al}_2\text{O}_3$ [101]) and $\sigma = 4.8 \cdot 10^9 \text{ Pa}$. Then for each strain step of $\varepsilon = 0.01$ the maximum potential temperature increase would be around 119 - 189 K. When compensated with thermal conductivity, the real temperature change will be less, and as we do not detect heat-induced crystallization, the temperature increase is substantially lower. This shows that due to the large stress level in the sample, adiabatic heating could very well influence the mechanical behaviour after yielding especially in our compression/shear tests where strain rates are fast, $\dot{\varepsilon} = 0.01 - 0.1 \text{ 1/s}$. Unfortunately, we lack direct experimental measurements of the adiabatic heating.

In tensile sample PTP3, we see a decrease in flow stress after yielding. However, it is unclear whether this is an adiabatic effect, as atomistic simulation with a thermostat set to 300 K show similar decrease in flow stress after yielding. The effect of adiabatic heating should increase by increasing strain rate, but in our experimental data, the viscous-like behaviour seems to dominate the level of flow stress. The effect of adiabatic heating could be studied by measuring experimental tensile yield stress using much higher strain rates than here. The simulations use an extremely high strain rate, but the thermostat keeps the temperature fixed at 300 K to rule out any heating effects. In the future, it might be possible to estimate the heat dissipation and adiabatic heating also by using the simulations.

One criticism that rises regarding our molecular dynamic simulation results is that how well they describe a true bulk behaviour of amorphous Al_2O_3 . As we use periodic boundary conditions in all of our current atomistic simulations, we should be free of surface effects, meaning we simulate the bulk behaviour. Our elementary box of atoms, which is then multiplied to produce the bulk, is large enough not to contain any "size effects". Normally using periodic boundary conditions, the radius of the elementary atom box describes the volume in which atoms are unique. If this radius is too small, there is possibility that the atomic movements are dictated too much by individual force fields of surrounding ions or atoms. Therefore, the box size needs to be big enough that the force field affecting each unique ion is averaged into an unchanging field by placing enough unique ions surrounding the ion under observation. We carefully selected the box size not to give such an effect. Regarding literature state-of-the-art, we found no atom simulation studies done to simulate mechanical properties of amorphous Al_2O_3 .

Criticism can be presented regarding the tensile test setup. Could the plasticity be a side effect of the defects and ion implantation caused by the focused ion beam milling? Gallium (+III) sits just below Aluminium (+III) in the periodic table, which explains that even at low temperature gallium is soluble to Al_2O_3 and can form solid solutions such as GaAlO_3 [102]. This means that Ga can substitute Al in the structure without causing phase changes. The possibility that GaAlO_3 has lower activation energy than Al_2O_3 , and therefore would promote room temperature creep, is out of scope of this study. Other point is that as Al_2O_3 is a fiercely stoichiometric oxide [1] therefore, it is not certain whether gallium can substitute aluminium ions in the lattice. Instead, it would not be a surprise to find gallium as metallic inside interstitials, voids and defects caused by the high-energy ion beam. As these aspects are out of scope, we have to rely on other clues and the most pressing clue is that the void formation and fracture happens inside the defected and gallium rich areas. Another clue is that also the centre of the sample in original as-deposited state undergoes the plastic deformation without void nucleation. Furthermore, we simply cannot overrule the plasticity found in the experimental compression/shear tests and atomic simulations, as there we have no effect of ion milling on the samples.

If we compare to amorphous SiO_2 , the effect of implanted gallium ions on mechanical properties would be harder to predict as silicon's oxidation number (+IV) makes direct substitution with Ga (+III) difficult, and in fact phase diagram shows zero solubility for Ga in SiO_2 [103]. Therefore, the focused ion beam milling with gallium is potentially more detrimental to SiO_2 compared to Al_2O_3 .

Discussion is important regarding whether plastic deformation in amorphous Al_2O_3 is possible. Two recent *in situ* investigations give mixed results: van der Rest *et al.* [104] loaded a porous and amorphous Al_2O_3 samples in tension using a "lab-on-a-chip" technique. They reached tensile fracture stresses below 1 GPa and they state that: "All on-chip test specimens fail in a brittle manner before plastic yielding, and this despite the small size of the samples". This seems logical in the light of the low critical stress intensity factor measured in our tensile experiment and the fact that the Al_2O_3 film in study of van der Rest *et al.* already contain pre-existing flaws in form of 2- 30 nm voids/pores [104]. As known, the flaws concentrate the stress and fracture occurs, since below critical stress there is no active plastic deformation mechanism available. On the other hand, Esmaeily *et al.* [82] report significant plastic deformation in amorphous Al_2O_3 nanotubes during *in situ* measurements with a tensile strength of 4.1 GPa, which is very close to our observations.

Other mechanical studies on amorphous Al_2O_3 thin films using methods that are more conventional also give mixed results. Some report a fully plastic behaviour [9] and some report fully elastic behaviour leading to fracture [82, 105, 115].

Based on the discussion, we are determined to conclude that plastic deformation of amorphous Al_2O_3 is a diffusion-based phenomena activated by stress gradients in the tested thin films. Plastic deformation can be activated at or very close to room temperature with a strong gradient stress field and requires no additional external driving energy source to function. The film needs to be sufficiently free of flaws in order to reach the required stress level needed to activate creep diffusion. To summarise the plastic behaviour and explain the mechanism of plastic deformation, we need a mathematical context, which we will present next.

3.8 Theory of plastic deformation in amorphous Al_2O_3

We propose a theory in which the tested solid, amorphous aluminium oxide (Al_2O_3) thin film, behaves at room temperature as a viscoelastic solid under a critical load and as a viscoplastic solid at a critical load at which it deforms purely by viscous flow. The plastic deformation can also be called “viscous creep” as a stress field acts as the main activation energy for the diffusion-based deformation. But note that here creep is not rate limited phenomenon such as thermally activated creep since the material goes through a liquid-like, viscous behaviour.

First, we define the boundary conditions for the plastic deformation of an amorphous material:

1. The deforming material has infinite dimensions \rightarrow no surface atoms.
2. The ions or molecules are randomly distributed inside the volume of deformation, in other words, the material is fully amorphous and isotropic.
3. The material does not undergo any secondary deformation such as fracture, shear banding or dislocation glide.
4. Temperature and strain rate remain constant.

Once loaded, the material will first exhibit a normal elastic response in which the stored elastic energy related to Hooke’s law [1] equals to

$$U_{\text{elastic}} = \frac{1}{2} \varepsilon \sigma_{app} = \frac{1}{2} \frac{\sigma_{app}^2}{E}, \quad [\text{Pa}] = \left[\frac{\text{N}}{\text{m}^2} \right] \quad (3.5)$$

where E is the elastic modulus of the solid, ε is the total strain the solid is subjected to and σ_{app} is a uniform applied stress. In a realistic loading situation of a solid material, the total elastic work becomes

$$W_{elastic} = V_{e-def} * \frac{1}{2} \frac{\sigma_{app}^2}{E}, \quad [J] = [m^3] \left[\frac{N}{m^2} \right] = Nm \quad (3.6)$$

where V_{e-def} is the elastic deformation volume. It is useful to calculate also the elastic work per mole

$$W_{elastic/mole} = N_A \Omega * \frac{1}{2} \frac{\sigma_{app}^2}{E}, \quad [J/mol] = \left[\frac{1}{mol} \right] \left[\frac{m^3}{ion} \right] \left[\frac{N}{m^2} \right] \quad (3.7)$$

where N_A is the Avogadro constant and Ω is the ionic volume

$$\Omega = \frac{M}{\rho * N_A}, \quad \left[\frac{kg/mol}{kg/m^3 * ion/mol} \right] = \left[\frac{m^3}{ion} \right] \quad (3.8)$$

where M is the molar mass, and ρ is the density. The total work of plastic deformation is then described by simply multiplying the amount of ions or atoms N_{def} in the deforming volume V_{def} by the effective activation energy Q_{eff} . The amount of diffusing atoms during plastic deformation is given by

$$N_{def} = \frac{V_{def} * \rho}{M}. \quad [mol] = \frac{[m^3] * [kg/m^3]}{[kg/mol]} \quad (3.9)$$

Then the total work of plastic deformation

$$W_{def} = \frac{V_{def} * \rho_s}{M_s} * Q_{eff}, \quad [J] = \frac{[m^3] * [kg/m^3]}{[kg/mol]} [J/mol] \quad (3.10)$$

where ρ_s is the density of the solid and M_s is the mass of one mole of the solid. Here the effective activation energy is given as per mole.

We use the term “effective” activation energy for two reasons; first, in order to maintain charge balance, it is uncertain if we move single ions or if the elementary unit of diffusion needs to be a neutral group of ions, in this case Al_2O_3 . Secondly, a single diffusion step in amorphous material is not well defined by any constant activation energy value; instead, the energy of each diffusion step is randomly distributed. Still we can predict that the activation energy will have a lower and upper boundary and the effective activation energy describes a mean value of the random distribution.

The effective activation energy Q_{eff} should be a value close to the self-diffusion activation energy, which in the case of O^{-2} ions in amorphous Al_2O_3 has been determined to be 1.3 ± 0.2 eV or 125 ± 19 kJ/mol [47]. As we lack data on Al^{+3} diffusion in amorphous Al_2O_3 , here we have to assume that the aluminium activation energy approximately equals average diffusion activation energy of oxygen. Whether this could be true, is of course under debate [46].

Then the total work done to deform the amorphous solid becomes

$$W_{\text{total}} = W_{\text{elastic}} + W_{\text{def}} \quad (3.11)$$

The stored elastic energy (for a uniform stress field) at yield stress 4.5 GPa ($E = 20 - 70$ GPa) would equal roughly 1.5 – 4.5 kJ/mol. Plastic deformation work is typically order of magnitude larger and demonstrates that plastic deformation will dominate the measured total work [1].

We can include a material specific strain rate dependence in our theory, which will modify the boundary condition number 4. For example based on atomistic simulations of amorphous Al_2O_3 , we get approximately 8 % increase in the σ_{def} if we increase the strain rate by an order of magnitude. According to our plastic deformation work theory, the parameter that changes according to strain rate, and in fact the only parameter that can change is the activation energy Q_{eff} . This is analogous to viscous liquids where the stress is proportional to strain rate and suggest that more energy is needed to stir a viscous liquid faster.

The viscous behaviour after yielding can be approximately Newtonian or change dynamically as a function of strain rate. Accordingly, The strain rate dependence factor $\Gamma []$ is either linear or curved as a function of strain rate and the strain rate dependant plastic work becomes

$$W_{\text{def}}(\dot{\epsilon}) = \frac{V_{\text{def}} * \rho_s}{M_s} * (Q_{\text{eff}} * \Gamma(\dot{\epsilon})_{\text{a-Al}_2\text{O}_3}) \quad (3.12)$$

We acknowledge that the real plastic deformation energy depends also on other variables, but their contribution is out of scope of the current study. The most important variables to be studied in the future include the ratio between bulk and surface atoms (boundary condition 1.), temperature (boundary condition 4.), ratio between amorphous and crystalline volume (boundary condition 2.) and the elastic constant.

Figure 3.32 illustrates the energy residual, which is the difference between experimentally measured total work W_{measured} and the calculated, strain rate corrected, theoretical plastic work $W_{\text{theor.}}$ values ($E_{\text{residual}} = W_{\text{theor.}} - W_{\text{measured}}$).

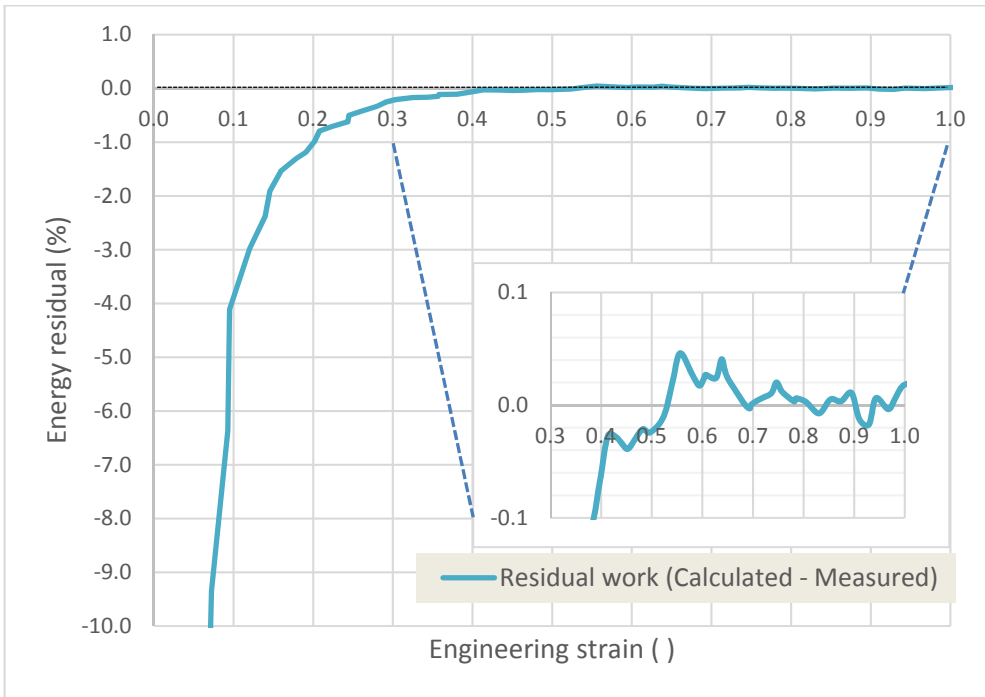


Figure 3.32: The energy residual ($W_{\text{theor.}} - W_{\text{measured}}$) for sample 3.1. Values used for theoretical calculations: activation energy 115 kJ/mol, density 3.255 g/cm³ (MD simulated relaxed bulk value) and molecular mass 101.96 g/mol. Strain rate corrected activation energy was obtained by correcting part of the full effective activation energy 115 kJ/mol by strain rate (90 kJ/mol [± 25 kJ/mol x DIC strain rate deviation from average DIC strain rate]). Copyright Erkka J. Frankberg 2017

Figure illustrates that the deviance can be very large ($> 10\%$) during the elastic response. However, after the onset of full plastic flow beginning from approximately 0.3 - 0.4 strain, we can measure $< \pm 0.1\%$ deviation of theory from the experimentally measured work $W = Fs$, where s [m] is the calibrated displacement. Results indicate excellent predicting power for the theory as we can consistently predict the plastic work with similar error for compression/shear samples and the tensile sample. The theoretical prediction of the total work of deformation after plastic yielding is summarized in the **Table 3.3**.

Table 3.3: Summary of literature, theoretical and simulated values of effective activation energy in amorphous Al_2O_3 . Error presented in standard deviation.

	Literature values (Oxygen diffusion)	Theoretical prediction [Current study]	Simulations [Current study]
“Effective” activation energy Q_{eff}	125 ± 19 kJ/mol [47, 48]	115 ± 4.9 kJ/mol (strain rate corrected)	9 ± 0.4 kJ/mol

The average effective activation energy calculated from our theory is approximately 115 kJ/mol, which can be matched with the experimentally measured work and which is in line with oxygen self-diffusion data for amorphous Al_2O_3 [48, 47].

Activation energy of atomistic simulations is substantially smaller. This is believed to be due to a fact that we use a thermostat, which negates the thermal component of the work or the fact that the stress field is assumed uniform in the whole simulated bulk. This will not be the case when compressing a real bulk, such as is in our experimental. The plastic flow volume in simulations is too large for a given stress, therefore energy kJ/mol appears smaller. We would need to give up using the periodic boundary conditions because they create the uniform stress field. This would require us to use a much, e.g. 10 times, larger simulation volumes and number of simulated ions, which was out of scope with current resources. Another reason for low simulated activation energy could be due to distribution of thermal energy component in the activation energy. Current simulations assume work to happen over the whole simulated volume, since the stress field is effectively constant over the volume. We later discuss that due to distribution of thermal activation energy, the percentage of ions moving inside the plastic volume at any given moment needs to be only 39 vol. % in order to accommodate equilibrium stress, or critical stress. If calculated for that volume, we would get higher effective activation energy per ion in simulations.

In the next chapter, we also show that the ratio of activation energy as a function of strain rate should decrease, as viscosity of amorphous Al_2O_3 seems to decrease as a

function of strain rate. This means that less work is needed to induce a given strain at a higher strain rate.

3.9 Viscous behaviour of amorphous Al_2O_3 at room temperature

The thorough discussion regarding the plastic deformation leads us to claim that the plastic deformation is based on viscoplasticity: diffusional flow of ions from compressive to tensile regions in which the driving energy is mainly received from mechanical energy, although a small thermal component remains in the total activation energy. Viscoplasticity often refers to a “Bingham solid” which is a solid that transforms into a fluid at a yield stress [98], although often the absolute yield stress is not easily defined.

As the activation energy has a large mechanical component, it is a creep mechanism and extends beyond the Nabarro-Herring creep and Coble creep mechanisms into a new low temperature domain. Additionally the observed viscoplastic phenomena has the potential to reveal the creep mechanism in Coble creep, if we assume grain boundaries as an amorphous phase, as is proposed in the concept of “nanoglass” by Gleiter [6]. This concept is already very close to Coble creep as it acts as a function of grain boundary volume [1], therefore we could think that grain boundaries have properties similar to glassy phase.

To gather evidence of the viscous behaviour, we can exploit the work theory regarding plastic deformation proposed in the earlier chapter. First, we define viscosity in compression and in tension, as typically viscosity is defined using shear stress/strain.

In the compression/shear experimental, the definition of shear viscosity can be used, as the sample flows against two rigid tools. Calculating viscosity in compression/shear, we assume that the compressive stress and strain rate are approximately equivalent to shear stress and shear strain rate. Shear viscosity

$$\eta_{\text{shear}} = \frac{\tau}{\dot{\gamma}} \cong \frac{\sigma_{\text{def}}}{\dot{\epsilon}} \quad , \quad [\text{Pa} \cdot \text{s}] = \left[\frac{\text{Ns}}{\text{m}^2} \right] = \left[\frac{\text{N}/\text{m}^2}{1/\text{s}} \right] \quad (\text{compr./shear test}) \quad (3.13)$$

where τ is shear stress and $\dot{\gamma}$ is shear strain rate. In tension, we use the definition of extensional viscosity [106] in which

$$\eta_{\text{tension}} = \frac{\sigma_{\text{def}}}{\dot{\epsilon}}, \quad [\text{Pa} \cdot \text{s}] = \left[\frac{\text{Ns}}{\text{m}^2} \right] = \left[\frac{\text{N}/\text{m}^2}{1/\text{s}} \right] \quad (\text{tensile test}) \quad (3.14)$$

where η_{tension} is the extensional viscosity and $\dot{\epsilon}$ is the extensional strain rate. For ideal Newtonian liquid under uniaxial flow and at low strain rate $3\eta_{\text{shear}} = \eta_{\text{tension}}$ as given by the “Trouton ratio” [106].

The critical stress σ_{def} needed to “stir” our amorphous sample is

$$\sigma_{\text{def}} = \frac{W_{\text{def}}}{V_{\text{def}}}, \quad \left[\frac{\text{N}}{\text{m}^2} \right] = \left[\frac{\text{Nm}}{\text{m}^3} \right] \quad (3.15)$$

where W_{def} is the work of plastic deformation and V_{def} is the volume of deformation (related to the critical stress field). If we assume viscous flow to happen during plastic deformation, then the viscosity as a function of strain rate can be rewritten as

$$\eta(\dot{\epsilon}) = \frac{W_{\text{def}}}{\dot{\epsilon} * V_{\text{def}}}, \quad \left[\frac{\text{Ns}}{\text{m}^2} \right] = \frac{[\text{Nm}]}{\left[\frac{1}{\text{s}} \right] * [\text{m}^3]} \quad (3.16)$$

Work of plastic deformation can be calculated directly using the measured force and displacement data. The true deformation volume was calculated as indicated in the chapter 2. Note that the strain rate in tensile test is an order of magnitude lower compared to compression/shear tests. **Figure 3.33** and **Figure 3.34** show viscosity data on compression/shear and tensile tests.

From the data we can deduce that our calculations work only for plastic deformation data (as should be), and the elastic data gives random viscosity values, although always below the plastic data. If we think the PLD Al_2O_3 as a viscoplastic solid, we could also ask whether the changes of “viscosity” in the elastic data are a sign of a changing magnitude of the plastic component in deformation.

The fully “plastic” viscosity data can be plotted into a single graph with the simulated viscosity as an insert shown in **Figure 3.35**. First, we can see a shift in the viscosity data when moving from shear viscosity in the compression/shear tests, to extensional viscosity in tensile tests. With the used estimation methods for plastic deformation volume, the ratio $\eta_{\text{tension}}/\eta_{\text{shear}}$ is 1.13, which is not that close to the Trouton ratio. In our experimental, the PLD Al_2O_3 exhibits viscosity values in the

range of $10^{10} - 10^{13} \text{ Pa} \cdot \text{s}$ as a function of strain rate. It is difficult to draw definite conclusions between the simulated and experimental viscosity data, as the gap between the strain rates is several orders of magnitude. Nevertheless, all data show similar trend in which viscosity decreases as a function of strain rate. The simulated viscosity data can also yield some clues to why the simulated activation energy is small compared to the experimental values.

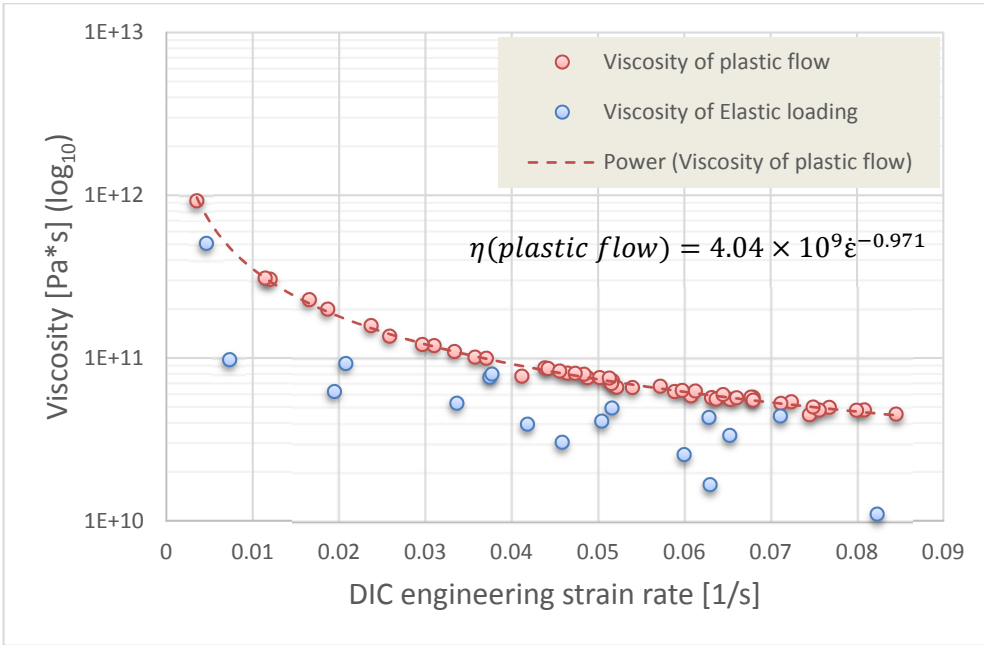


Figure 3.33: Calculated Log viscosity data as a function of momentary strain rate for compression/shear sample 3.1. Blue data points represent the elastic data set and red data points are selected to include only the full plastic flow data. Copyright Erkka J. Frankberg 2017

Extensional and shear viscosity data seem to be closely related. This is probably because the flow stress in compression/shear tests is dominated by compressive part of the loading, which have equivalent flow stress to tensile tests shown for example in the atomistic simulations. We can also imagine that for some reason the Trouton ratio is not relevant in these measurements. In addition, if we would correct the immediate tensile plastic volume with a coefficient ≈ 1.13 , in the grounds that we underestimate the plastic volume in our calculations, then both shear and extensional datasets would fall into the same power-law line. As we do not have FEM analysis on the tensile test, we will assume that Trouton ratio could hold also

in this case in addition to polymers where the ratio is typically used [106], but only if we could measure pure shear loading in the experimental setup.

Both shear and extensional viscosity follow a similar power law from 0.001 to 0.1 strain rate, which signals a gradual transition under stress from a solid to a viscoplastic solid. In our strain rate measurement range, we detect no sharp transition from a solid to liquid. The power-law for the viscosity as function strain rate for amorphous Al_2O_3 can be written as:

$$\begin{aligned}\eta_{\text{shear}}(\dot{\epsilon}) &\cong 4.04 \times 10^9 \cdot \dot{\epsilon}^{-0.971} \text{ Pa} \cdot \text{s}, \quad \{\dot{\epsilon} = 0.01 - 0.1\} \\ \eta_{\text{tension}}(\dot{\epsilon}) &\cong 4.22 \times 10^9 \cdot \dot{\epsilon}^{-0.983} \text{ Pa} \cdot \text{s}, \quad \{\dot{\epsilon} = 0.001 - 0.01\}\end{aligned}$$

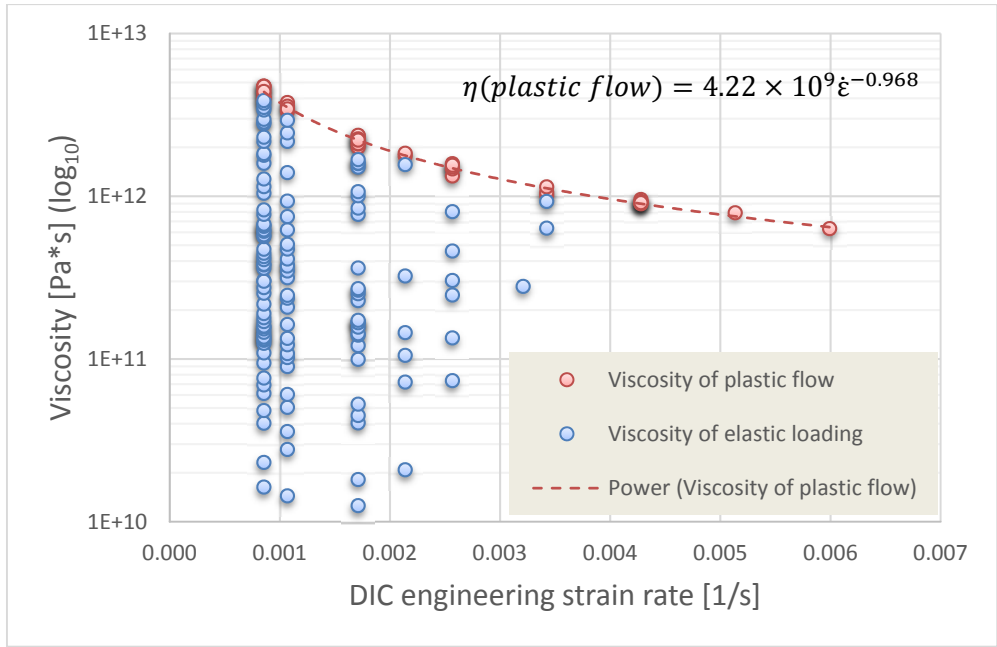


Figure 3.34: Calculated Log viscosity data as a function of momentary strain rate for PTP3 tensile data. Blue data points represent the elastic data set and red data points are selected to include only the full plastic flow data. Data appears in columns, as it is the maximum strain rate resolution for the used imaging conditions with image correlation method. Copyright Erkka J. Frankberg 2017

It seems likely that before applying any stress, the amorphous film ($\text{a-Al}_2\text{O}_3$) is a solid and the viscosity approaches infinity (ideal solid state)

$$\lim_{\dot{\epsilon} \rightarrow 0} \eta_{\text{a-Al}_2\text{O}_3}(\dot{\epsilon}) = \infty. \quad (3.17)$$

As we apply a stress field, we force deformation over the solid, and in order for the solid to flow at an infinitesimally slow speed, the viscosity has to become a finite quantity. This might mean that even under relatively low stress (few hundred megapascals for example) a finite viscosity could be measured, but would be extremely large as for example in the case of granite rock [107].

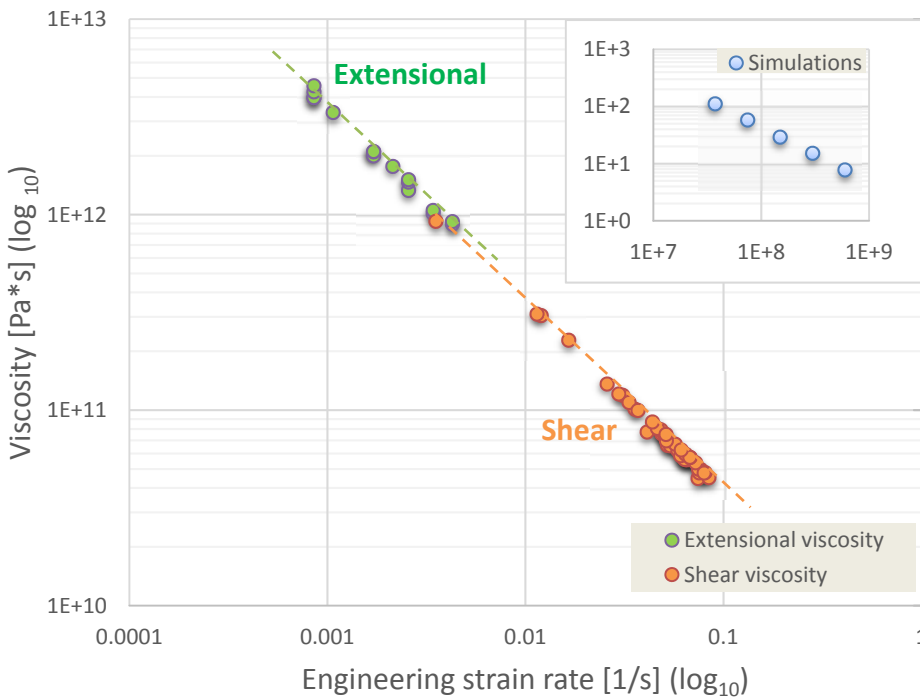


Figure 3.35: Combined extensional (green) and compression/shear (orange) data on viscosity (Log 10) as a function of strain rate (Log 10) during plastic flow. Insert shows the viscosity calculated with simulated compression data using averaged flow stress between 8 - 30 % total strain. Copyright Erkka J. Frankberg 2017

Another possible way to comprehend the decrease in viscosity with increasing strain rate during plastic deformation is that, in order to increase strain rate, each moment we must move a greater volume of material. This produces a greater amount of adiabatic heat per time unit, which increases the heat component of diffusion. Stress will still increase with increasing strain rate as long as viscosity remains a positive quantity. However, as simulation give similar decreasing trend for viscosity as a function of strain rate and as we believe our experimental samples are at room

temperature, the adiabatic heating does not necessarily explain the behaviour and it should be addressed in future studies.

The viscosity results give more understanding regarding the work theory of plastic deformation introduced earlier. As we are able to measure viscosity of the amorphous Al_2O_3 , then the strain rate dependence factor Γ [] in **equation 3.12**, modifying the effective activation energy will correlate to the viscosity of our sample. With our current results, we can say that the correlation used in this study is still an approximation and further studies are needed to find an analytical result on how viscosity and activation energy are related.

Regarding the flow stress as function of strain rate, we can calculate from the power laws that the flow stress will increase approximately 7 - 13 % depending on the loading mode, when we increase the strain rate by an order of magnitude. The molecular dynamic simulations support this well, as the increase in flow stress is approximately 8 % when we increase the strain rate by an order of magnitude.

Now what is different to a liquid deformation and viscoplasticity or viscous creep? In a liquid, all molecules are moving together in a unison as they all have enough thermal activation to move. For example, water is above its melting point and therefore will flow under its own gravity. In a viscoplastic movement of a solid glass below glass transition temperature, the movement is restricted to a volume that is under sufficiently high stress, which can be studied for example using the contact theory. The diffusional movement leading to permanent creep deformation in a glass is mediated by vacancy-like free sites, which means that only a set amount of volume under the stress is moving at any given moment. Our results show that this leads to a very different dynamic response in creep-mediated viscosity compared to a liquid: The stress increases when we increase strain rate because the viscosity remains a positive quantity, but the viscosity is decreasing with increasing strain rate. An example of this behaviour can be seen in **figure 3.35**.

Can a solid amorphous material, a glass, flow under the glass transition temperature? Our answer is yes, under a sufficient stress field a finite viscosity can be measured in an amorphous solid. The notion that a flat glass panel would thicken up from its bottom over few thousand years is still nonsense, as a typical glass panel will fracture at very low stress (due to pre-existing defects) and the viscosity would remain extremely high, although finite, and possibly taking perhaps more than 20 million years before any measurable change would occur [61]. One also has to remember that directed diffusion (creep) and random self-diffusion are competing mechanisms. When stress is low, heat activation can overcome and the random

motion dominantly determines the flow direction of ions. There is a vivid ongoing discussion regarding this question in both literature [61, 62, 63, 107, 108, 109] and in the popular discussion [110, 111]. The discussion still seems to linger over the popular myth of the creep of old church windows, which should be discarded as false.

As a summary, the viscous behaviour of amorphous Al_2O_3 is proposed to be non-Newtonian and viscosity is related to strain rate by a power law. This could explain earlier results showing non-Newtonian creep behaviour for fine-grained $\alpha\text{-Al}_2\text{O}_3$ [55], if we assume that a crystalline Al_2O_3 grain boundary and amorphous phase have similar ionic structure.

3.10 On the applicability of Nabarro-Herring and Coble creep

We can test whether the observed creep behaviour can be explained by some other thermally activated creep mechanism such as Nabarro-Herring creep or Coble creep. My personal view is that the observed plastic flow is mediated by a high concentration of vacancy-like holes in glass structure, which is signalled by much lower theoretical density of glasses compared to equivalent crystalline phase. Both Nabarro-Herring and Coble creep start from the assumption that plastic deformation by creep is based on thermally activated self-diffusion, which can be directed to certain direction by a uniform stress gradient and mediated by vacancy diffusion. Thermal activation means that diffusion, and therefore plastic deformation, will be diffusion rate limited phenomena. This means that over a critical strain rate, the deformation contains an increasing elastic component leading to a fracture when the critical stress intensity is reached [7].

A given temperature approximately equals to self-diffusion rate D , which is a measure of how many atoms move across a specific area in a time unit. Diffusion rate can be determined using the characteristic diffusion rate with Arrhenius type temperature dependence as

$$D = D_0 e^{\left(-\frac{Q}{RT}\right)} \quad (3.18)$$

The characteristic diffusion constant D_0 in oxides is typically derived from D values measured using ^{18}O isotope diffusion annealing [46, 47]. To study the applicability to our results, we can simulate what would be the critical strain rate predicted by the Nabarro-Herring or Coble creep for the tensile specimen PTP3 of amorphous Al_2O_3 using parameters $T = 300 \text{ K}$, $\omega = 8$, $d = 50 \text{ nm}$, $\sigma = 5 \text{ GPa}$, $\Omega_{\text{ion}} =$

$5.2 * 10^{-29} \text{ m}^3/\text{ion}$ and according to Nakamura *et al.* a self-diffusion rate $D_{\text{ion}}(273 \text{ K}) = 1.042 * 10^{-37} \text{ m}^2/\text{s}$ for amorphous Al_2O_3 [47]. For Cobble creep we assume that in our tensile test, the grain boundary thickness equals sample diameter $\delta_{\text{gb}} = d$ and therefore Nabarro-Herring equation gives an estimate in both cases.

$$\dot{\epsilon}(\text{N-H}) = \frac{\omega \Omega_{\text{ion}} D_{\text{ion}} \sigma}{k_B T d^2} \quad / \quad \dot{\epsilon}(\text{Coble}) = \frac{\Psi \Omega_{\text{ion}} D_{\text{ion}} \delta_{\text{gb}} \sigma}{k_B T d^3} \quad (3.19)$$

We assume that the rate control happens by the oxygen ions moving along their fastest path. **Table 3.4** summarizes the results.

Table 3.4: Maximum strain rates as a function of temperature predicted by Nabarro-Herring and Coble creep for the tensile specimen PTP3 of amorphous Al_2O_3 .

Temperature	Maximum thermally activated creep strain rate [1/s]
273 K	$2.3 * 10^{-20}$
300 K (Room Temp.)	$3.0 * 10^{-18}$
600 K	$1.1 * 10^{-7}$
973 K (Crystallization T)	0.0010

Based on the result at room temperature (300 K), it seems impossible that the observed plastic deformation in our tensile (or compression/shear) test is a rate limited, thermally activated process. Interestingly at crystallization temperature (973 K), the experimental and predicted creep strain rate matches quite well. This is most probably coincidence since we observed no fracture in compression/shear tests where strain rates are 1 - 2 orders of magnitude higher, or in simulations, where strain rate is 11 orders of magnitude higher. We also do not observe any crystallization, which would have signalled the temperature increase.

There is a fundamental difference in thermal and mechanical activation of diffusion. Once the diffusion is activated by a stress field, the whole volume does not need to be deforming simultaneously. We could postulate that the difference between a thermal and mechanical activation is that of a solid and liquid. The thermal activation energy of liquids is so high that their own gravity is enough to deform them. Mechanical activation energy in a solid enables a part of the solid under sufficient stress field to exhibit a viscous creep as long as the stress is applied. Once stress is relieved the behaviour returns to that of a solid. There are signs that this kind of behaviour could apply also for crystalline nanomaterials [84], where deformation of a single crystal happens by a liquid-like flow instead of dislocations.

For mechanically activated deformation of solids, an updated theory is needed and which we address in this work. The inability of N-B and Coble creep models to explain our results signals that rate limited vacancy diffusion is not the mechanism of plastic flow in inorganic glasses at low temperature. Instead, we believe that the flow is allowed by translation and rotation of ionic bonds in the glass structure, which is mediated by high concentration of vacancy-like free sites. This mechanism will not be diffusion rate limited, but at low temperature requires extremely high stress given the high bond strength in ionic (and covalent) materials.

3.11 Modelling the stress-strain behaviour of amorphous Al_2O_3

Based on our deformation work theorem, we can estimate the stress vs. strain behaviour of the material. First, the material will exhibit a normal elastic response in which the stored elastic stress equals to

$$\sigma_{\text{elastic}} = E\varepsilon, \quad \left[\frac{\text{N}}{\text{m}^2} \right] = \left[\frac{\text{N}}{\text{m}^2} \right] [] \quad (3.20)$$

The stress needed to activate the plastic deformation in the deformation volume is gained when we know that total work $W_{\text{def}} = Fs$, [Nm]. Then dividing the **equation 3.10** with the deformation volume gives

$$\frac{W_{\text{def}}}{V_{\text{def}}} = \frac{\rho_s}{M_s} * Q_{\text{eff}} \quad (3.21)$$

In which the left side reduces into stress

$$\frac{W_{\text{def}}}{V_{\text{def}}} = \sigma_{\text{def}} \quad , \quad \left[\frac{\text{Nm}}{\text{m}^3} \right] = \left[\frac{\text{N}}{\text{m}^2} \right] \quad (3.22)$$

and the right side reduces equally into stress

$$\frac{\rho_s}{M_s} * Q_{\text{eff}} = \sigma_{\text{def}} \cdot \left[\frac{\text{kg}/\text{m}^3}{\text{kg}/\text{mol}} \right] [\text{J}/\text{mol}] = \left[\frac{\text{J}}{\text{m}^3} \right] = \left[\frac{\text{Nm}}{\text{m}^3} \right] = \left[\frac{\text{N}}{\text{m}^2} \right] \quad (3.23)$$

Therefore, the critical stress needed to induce and maintain plastic deformation given by the theory is

$$\sigma_{\text{def}} = \frac{\rho_s}{M_s} * (Q_{\text{eff}}), \quad \left[\frac{\text{N}}{\text{m}^2} \right] = \frac{\left[\frac{\text{kg}}{\text{m}^3} \right]}{\left[\frac{\text{kg}}{\text{mol}} \right]} \left[\frac{\text{J}}{\text{mol}} \right] \quad (3.24)$$

With the given boundary conditions, σ_{def} is a constant value and remains constant throughout the deformation. The stress as a function of strain can be then calculated by the following equation

$$\sigma(\epsilon) = E\epsilon, \{E\epsilon \leq \sigma_{\text{def}}\} \quad \wedge \quad \sigma(\epsilon) = \frac{\rho_s}{M_s} * Q_{\text{eff}}, \{E\epsilon \geq \sigma_{\text{def}}\} \quad (3.25)$$

The proposed **equation 3.25** allows us to draft a rough outline of mechanical behaviour as shown in **3.36**.

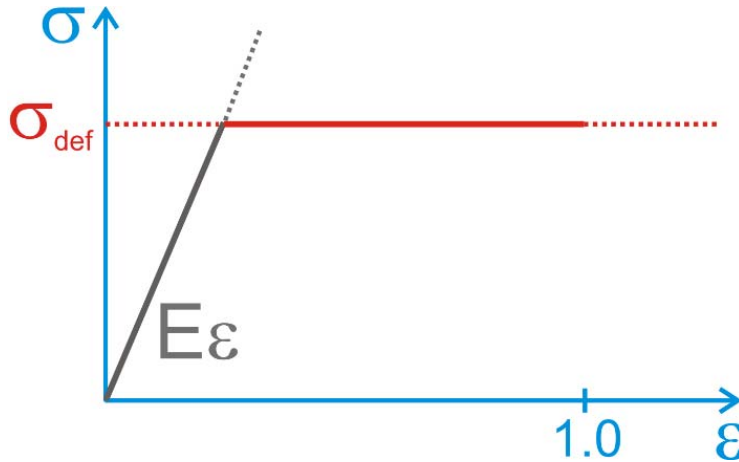


Figure 3.36: Stress/strain curve drafted using equation 3.25. Elastic stress builds up until a critical stress level is reached, under which plastic deformation activates and a constant stress is maintained as no more elastic energy can be stored without activating diffusion.

Copyright Erkka J. Frankberg 2017

Using the literature values of activations energy ($Q_{\text{eff}} = 106 - 144 \text{ kJ/mol}$ [47]), the corresponding critical stress predicted by the theory for amorphous Al_2O_3 is $\sigma_{\text{def}} = 3.4 - 4.6 \text{ GPa}$ (simulated relaxed density $\rho = 3.25 \text{ g/cm}^3$ & $M = 101.96 \text{ g/mol}$). Predicted critical stress is in line with the experimentally measured average critical (yield) stress for beam OFF compression/shear ($4.5 \pm 0.3 \text{ GPa}$) for tension (4.8 GPa), and for simulated compression ($4.5 \pm 0.2 \text{ GPa}$) and simulated tension ($4.7 \pm 0.2 \text{ GPa}$).

To further increase the predicting power, we can write the critical stress as a function of strain rate as explained in the theory.

$$\sigma_{\text{def}}(\dot{\epsilon}) = \frac{\rho_s}{M_s} * (Q_{\text{eff}} * \Gamma(\dot{\epsilon})_{\text{a-Al}_2\text{O}_3}), \quad \left[\frac{\text{N}}{\text{m}^2} \right] = \frac{\left[\frac{\text{kg}}{\text{m}^3} \right]}{\left[\frac{\text{kg}}{\text{mol}} \right]} \left[\frac{\text{J}}{\text{mol}} \right] \quad (3.26)$$

The rough presentation of **equation 3.25** is useful in some cases, but the shift between elastic and plastic deformation is unrealistically sharp. Diffusion is still fundamentally a thermally activated process and we operate over 0 K. Phonon theory explains that if a solid material has a temperature > 0 K, the energy is not constant throughout the lattice, but randomly fluctuates around a mean value [112]. The random vibrations of ions in the lattice, described by phonons, is what we usually call as heat. The available thermal activation energy is distributed in a solid by a probability function, which describes the probability that any selected ion will oscillate with a given energy. Due to the distribution of energy, some ions in the solid will diffuse with stress under the critical stress σ_{def} .

One of the most well know probability density functions is the Maxwell-Boltzmann distribution that was originally developed to describe the behaviour of ideal gases. Since general diffusivities of solids and viscous liquids are much slower than of gases, Maxwell-Boltzmann distribution will likely overestimate the magnitude and distribution of the energy. To get a density function that is more accurate we would need to use the quantum mechanics based description of the phonon energy and energy distribution [112].

To be able to apply the energy distribution function we first need to consider that how the total elastic and plastic work is divided to single ions. The elastic work per deformed volume

$$\frac{W_{\text{elastic}}}{V_{\text{def}}} = E\epsilon, \quad \left[\frac{\text{J}}{\text{m}^3} \right] = \left[\frac{\text{N}}{\text{m}^2} \right] \quad (3.27)$$

The elastic work stored on a single ion is then

$$W_{\text{elastic/ion}} = E\epsilon\Omega, \quad \left[\frac{\text{J}}{\text{m}^3} \right] \left[\frac{\text{m}^3}{\text{ion}} \right] = \left[\frac{\text{J}}{\text{ion}} \right] \quad (3.28)$$

where Ω is the ionic volume

$$\Omega = \frac{M}{\rho * N_A} , \quad \left[\frac{\text{kg/mol}}{\text{kg/m}^3 * \text{ion/mol}} \right] = \left[\frac{\text{m}^3}{\text{ion}} \right] \quad (3.29)$$

where N_A is the Avogadro constant. For plastic work per deformed volume, first, we divide the work done at each strain point by the corresponding deformation volume to measure how much work is done per deformation volume, this corresponds directly to **equation 3.22**, but we treat the work as energy per volume.

$$\frac{W_{\text{def}}}{V_{\text{def}}} = \sigma_{\text{def}} , \quad \left[\frac{\text{J}}{\text{m}^3} \right] = \left[\frac{\text{N}}{\text{m}^2} \right] \quad (3.30)$$

Then the work needed to yield/diffuse a single ion is

$$W_{\text{def/ion}} = \sigma_{\text{def}} \Omega . \quad \left[\frac{\text{J}}{\text{m}^3} \right] \left[\frac{\text{m}^3}{\text{ion}} \right] = \left[\text{J/ion} \right] \quad (3.31)$$

Then by current theory and boundary conditions, in order to allow plastic flow below the critical stress values, the values of available thermal activation energy Q_T as a function of strain should equal to difference of $W_{\text{def/ion}} - W_{\text{elastic/ion}}$

$$Q_T(\epsilon) = W_{\text{def/ion}} - W_{\text{elastic/ion}} = \sigma_{\text{def}} \Omega - E \epsilon \Omega . \quad (3.32)$$

Then we need to find a cumulative distribution for the thermal activation energy. Here we could use any suitable distribution function that describes the real energy distribution in an amorphous solid as well as possible. The available functions include at least Planck/Bose-Einstein, Fermi-Dirac and Maxwell-Boltzmann distributions. The general form of the probability density function of energy can be given for example as classical mechanics Maxwell-Boltzmann-type of distribution

$$f(W) = \frac{1}{A e^{E/k_B T}} \quad (3.33)$$

Where $A []$ is a normalization term which can change with temperature. Or as a quantum mechanics Planck or Bose-Einstein distribution for energy

$$f(W) = \frac{1}{A e^{E/k_B T} - 1} \quad (3.34)$$

The corresponding cumulative distribution is then given as function of strain as

$$\text{CDF } f(\varepsilon) = \sum_{i=1}^n f(\varepsilon)_i \quad (3.35)$$

Finally, we can equate that the stress as a function of strain can be presented as

$$\begin{aligned} \sigma(\varepsilon) &= E\varepsilon - [E\varepsilon * \text{CDF } f(\varepsilon)], \quad \{E\varepsilon \leq \sigma_{\text{def}}\} \\ \wedge \\ \sigma(\varepsilon) &= \sigma_{\text{def}}, \quad \{\sigma_{\text{def}} - E\varepsilon \leq 0 \wedge E\varepsilon - [E\varepsilon * \text{CDF } f(\varepsilon)] \geq \sigma_{\text{def}}\} \end{aligned} \quad (3.36)$$

Using the limit $\sigma(\varepsilon) = \sigma_{\text{def}} \{E\varepsilon - [E\varepsilon * \text{CDF } f(\varepsilon)] \geq \sigma_{\text{def}}\}$ is justified by thinking that once critical stress value is reached, no more elastic energy can be stored because full plastic flow is activated.

Figure 3.37 shows a general stress-strain behaviour of the material with viscoplastic behaviour predicted by **equation 3.36**, when applying an energy distribution hypothesis to the theory with original boundary conditions.

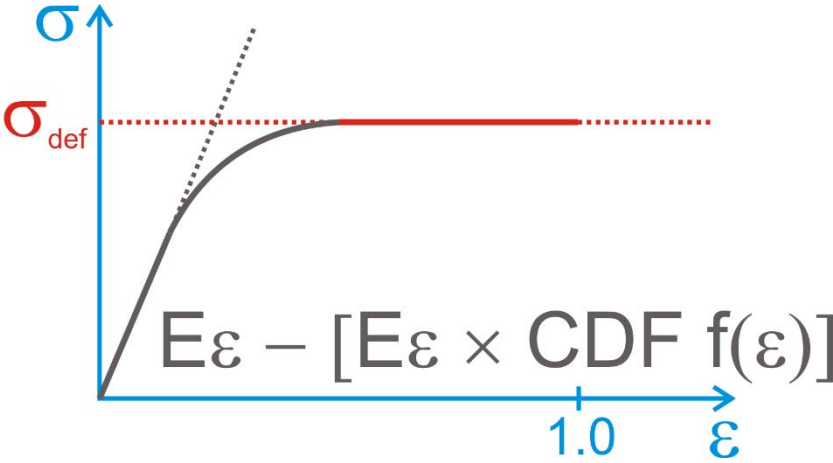


Figure 3.37: Stress strain behaviour of an amorphous solid below glass transition temperature with elastic behaviour modified by probability function of thermal activation energy. Copyright Erkka J. Frankberg 2017

Quantum dynamic considerations are out scope of this work, therefore we can evaluate the distribution of thermal energy in amorphous Al_2O_3 using the classical Maxwell-Boltzmann distribution. In this case, we give an estimate of thermal

activation energy $Q_T(\epsilon)$ by using the definition of kinetic energy. For a solid, the kinetic energy of each ion W_{kinetic} should equal the thermal activation energy as a function of strain available for each ion as

$$W_{\text{kinetic}} = \frac{1}{2}mv^2 = Q_T(\epsilon) \quad , \quad (3.37)$$

where m (kg) is the mass of ions and v is the velocity of ions. By reordering the variables, we learn that velocity of ions

$$v = \sqrt{\frac{2|Q_T(\epsilon)|}{m}} \quad . \quad (3.38)$$

The Maxwell-Boltzmann distribution function states that the distribution function of ion velocities (kinetic energy) is written as

$$f(v) = 4\pi \left[\frac{M}{2\pi RT} \right]^{\frac{3}{2}} v^2 \exp \left[\frac{-Mv^2}{2RT} \right] \quad . \quad (3.39)$$

Adding the definition of ion velocity, the distribution of thermal activation energy for a solid then becomes

$$f(Q_T) = 4\pi \left[\frac{M}{2\pi RT} \right]^{\frac{3}{2}} \sqrt{\frac{2Q_T(\epsilon)}{m}}^2 \exp \left[\frac{-M \sqrt{\frac{2Q_T(\epsilon)}{m}}^2}{2RT} \right] \quad . \quad (3.40)$$

Finally, the thermal activation can be given as a function of strain as given in **equation 3.32**, which yields a distribution function

$$f(\epsilon) = 4\pi \left[\frac{M}{2\pi RT} \right]^{\frac{3}{2}} \sqrt{\frac{2(\sigma_{\text{def}}\Omega - E\epsilon\Omega)}{m}}^2 \exp \left[\frac{-M \sqrt{\frac{2(\sigma_{\text{def}}\Omega - E\epsilon\Omega)}{m}}^2}{2RT} \right] \quad . \quad (3.41)$$

As the number of ions in our experimental is very large, we can state that the maximum probability equals the mean probability of the events and we do not need to use Darwin-Fohler method [113]. As the stored elastic energy increases as a

function of strain, more and more atoms will be able overcome the diffusion barrier, therefore we calculate the cumulative effect of the distribution as

$$\text{CDF } f(\varepsilon) = \sum_{i=1}^n f(\varepsilon)_i \quad , \quad (3.42)$$

where CDF $f(\varepsilon)$ is the cumulative distribution function of thermal activation energy as a function of total strain in the solid. Here we assume that probability [%] of number of ions given by the cumulative distribution function equals to volume percent [vol. %] in a solid.

Figure 3.38 shows how the experimentally measured average data of beam OFF compression/shear correlates with the prediction using **equation 3.36** and while using the maximum reported literature value of oxygen activation energy $Q_{\text{eff}} = 144 \text{ kJ/mol}$ for amorphous Al_2O_3 , experimentally measured elastic modulus of $E = 20 \text{ GPa}$, temperature of 105 K and absolute values of Q_T .

As seen in the figure, the fit can be good with experimental compression/shear data (flow stress etc.). The results seem to account for the gradual shift from elastic to plastic behaviour observed in both experimental and simulated results. This fortifies the hypothesis that the gradual change from elastic to plastic deformation is likely thermally activated. The challenges of using Maxwell-Boltzmann energy distribution are also clear: The temperature is set to 105 K , which is quite far from room temperature used in experimental setup.

Under critical stress the Maxwell-Boltzmann energy distribution predicts that approximately 39 vol. % of ions inside the given stress field are moving at any given time to accommodate full plastic flow. It would seem logical that not all ions inside the stress field need to move in unison in order to allow full plastic flow. The specific ions, which activate and diffuse, constantly change as the thermal activation energy fluctuates in the total volume of the solid, and therefore allow flowing with constant stress. If we would activate any more ions, the flow stress would decrease, which would not happen in reality as we constantly apply maximum load on the sample.

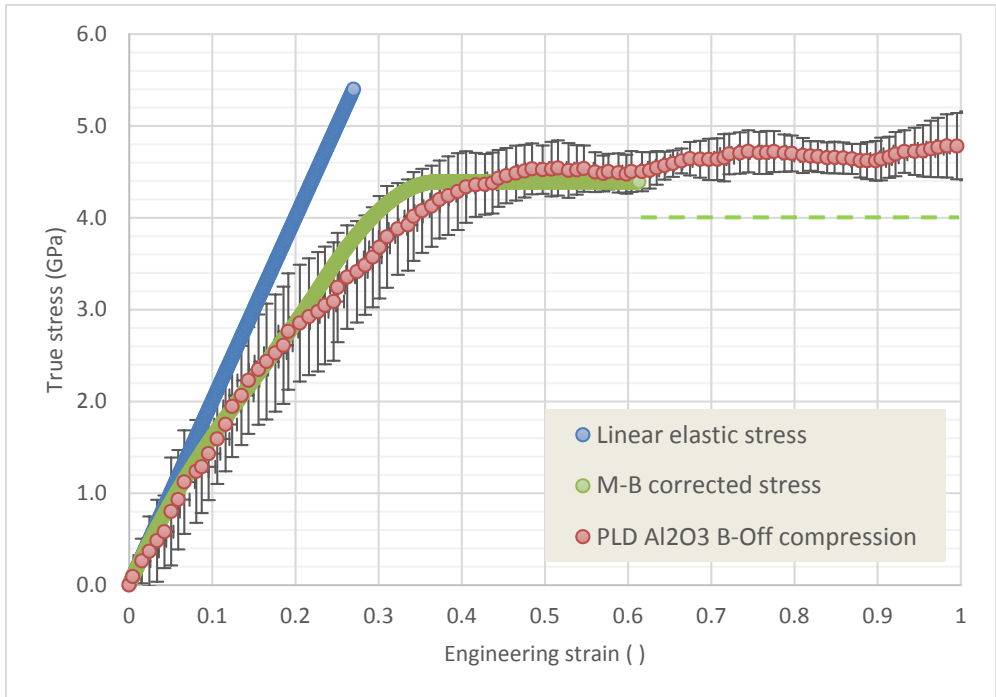


Figure 3.38: Comparison of average experimental stress/strain behaviour of beam OFF tests to the theoretical stress/strain behaviour obtained using equation 3.36 with Maxwell-Boltzmann energy distribution. Calculations are done using effective activation energy $Q_{eff} = 144$ kJ/mol, $E = 20$ GPa and temperature is set to 105 K. Copyright Erkkä J. Frankberg 2017

The role of thermal activation energy gives new perspective to the critical stress needed for flow stress. More true definition would be “equilibrium stress” because it is effectively the maximum attainable stress in an amorphous solid when boundary condition 4 holds. If more than 39 vol. % of the ions move, the stress would start to decrease again.

4. Conclusions

We show that amorphous aluminium oxide (Al_2O_3) thin films at room temperature can undergo viscoplastic deformation with 15 – 100 % total strain without fracture, depending on the sample preparation method and loading geometry. Plastic deformation was found to activate independently of the electron beam during *in situ* transmission electron microscopy experiments.

The mechanism of deformation was determined to be mechanically activated “viscous creep”. Flow will likely happen by translation and rotation of ionic bonds in the glass structure, which is mediated by high concentration of vacancy-like free sites. The diffusion-mediated creep of the material resembles viscous flow, in which no observable necking occurs and the stress is proportional to strain rate by definition of viscosity, and no other strengthening mechanism were observed. On the other hand, the mechanism is similar to creep as it is activated by a gradient stress field in addition to ambient thermal energy. The results lead to the conclusion that viscous creep of inorganic glass can be activated even at room temperature by increasing the stress to a sufficient level. Therefore, mechanical energy is equivalent to thermal energy in the activation of diffusion in these materials.

The key constituent to allow sufficiently high stress levels, up to several gigapascals, was the extremely low geometrical flaw size in the samples. This is underlined by the measured critical intensity factor ($K_{\text{Ic}} = 3.1 \text{ MPa} \cdot \text{m}^{1/2}$) for the amorphous Al_2O_3 thin film material, which is very similar to normally measured values for bulk Al_2O_3 ($K_{\text{Ic}} = 2 - 6 \text{ MPa} \cdot \text{m}^{1/2}$). This explains that the material remains brittle also in the extreme nanosize. However, at sufficiently high stress, diffusion mediated viscous flow activates before brittle fracture and the material can yield up to 100 %, and possibly beyond, as no necking or strain hardening phenomena occur during viscous flow.

Based on the results we proposed a theory that consistently predicts the work and critical flow stress in amorphous Al_2O_3 . Applicability of the theory to other dense amorphous ceramics needs to be tested in the future. The presented results and theoretical considerations will help to understand complex plasticity phenomena in materials, especially in ceramics including a glassy phase, such as plastic deformation during indentation experiments, grain boundary mediated superplasticity, creep assisted densification during pressure assisted sintering and static creep under constant load.

References

- [1] M. W. Barsoum, *Fundamentals of Ceramics*, McGraw-Hill, 668 p., 1997
- [2] D. R. H. Jones & M. Ashby, *Engineering materials 1*, 4th edition, Butterworth-Heinemann, 496 p., 2011
- [3] A. H. Heuer, K. P. D. Lagerlöf & J. Castaing. Slip and twinning dislocations in sapphire (α -Al₂O₃). *Philosophical Magazine A*, 78:3, p. 747-763, 1998
- [4] C.E. Inglis. Stresses in a plate due to the presence of cracks and sharp corners. *Trans. Inst. Naval Archit.* 44, p. 219-241, 1913
- [5] A.A. Griffith. The Phenomena of Rupture and Flow in Solids. *Phil. Trans. R. Society A221*, p. 163-198, 1921
- [6] H. Gleiter. Nanocrystalline materials. *Progress in Materials Science* 33:4, p. 223-315, 1989
- [7] J. Karch, R. Birringer & H. Gleiter. Ceramics ductile at low temperature. *Nature* 330, p. 556 – 558, 1987
- [8] E. Calvié, L. Joly-Pottuz, C. Esnouf, P. Clément, V. Garnier, J. Chevalier, Y. Jorand, A. Malchère, T. Epicier, K. Masenelli-Varlot. Real time TEM observation of alumina ceramic nano-particles during compression. *Journal of European ceramic society*, 32:10, p. 2067-2071, 2012
- [9] F. García Ferré, E. Bertarelli, A. Chiodoni, D. Carnelli, D. Gastaldi, P. Vena, M. G. Beghi, F. Di Fonzo. The mechanical properties of a nanocrystalline Al₂O₃/a-Al₂O₃ composite coating measured by nanoindentation and Brillouin spectroscopy. *Acta Materialia* 61, p. 2662–2670, 2013
- [10] T. J. Brown, N. E. Idoine, E. R. Raycraft, R. A. Shaw, E. A. Deady, S. F. Hobbs, T. Bide. *World mineral production 2011-2015*, Keyworth - British geological survey, 2017
- [11] K. Zheng, C. Wang, Y.-Q. Cheng, Y. Yue, X. Han, Z. Zhang, Z. Shan, S. X. Mao, M. Ye, Y. Yin & E. Ma. Electron-beam-assisted superplastic shaping of nanoscale amorphous silica. *Nature communications* 1:24, 2010
- [12] E. Kannisto, E. Cura, E. Levänen, S-P. Hannula. Mechanical properties of alumina based nanocomposites. *Key Engineering Materials* 527 p. 101 – 106, 2013

- [13] E. J. Frankberg, L. Joly-Pottuz, F. García Ferré, T. Salminen, J. Kalikka, S. Koneti, L. Roiban, T. Douillard, B. Le Saint, J. Akola, E. Levänen, F. Di Fonzo, K. Masenelli-Varlot. In situ deformation of nanocrystalline Al₂O₃ thin films at room temperature. European Materials Research Society (E-MRS) spring meeting, Strasbourg, France, oral presentation 5/2017. Available from: [https://www.researchgate.net/publication/317092706_In_situ_deformation_of_nanocrystalline_Al₂O₃_thin_films_at_room_temperature](https://www.researchgate.net/publication/317092706_In_situ_deformation_of_nanocrystalline_Al2O3_thin_films_at_room_temperature)
- [14] E. J. Frankberg, L. Joly-Pottuz, F. García Ferré, T. Salminen, J. Kalikka, S. Koneti, L. Roiban, T. Douillard, B. Le Saint, J. Akola, E. Levänen, F. Di Fonzo, K. Masenelli-Varlot. Plastic deformation of nanostructured Al₂O₃ at room temperature. Nanobrücke – Hysitron User meeting, Manchester, England, oral presentation 4/2017
- [15] E. J. Frankberg, L. Joly-Pottuz, F. García Ferré, T. Salminen, J. Kalikka, S. Koneti, L. Roiban, T. Douillard, B. Le Saint, J. Akola, E. Levänen, F. Di Fonzo, K. Masenelli-Varlot. Plastic deformation of nanostructured Al₂O₃ at room temperature. Collaboration meeting between Tampere University of Technology, Italian Institute of Technology and INSA de Lyon, Milano, Italy, oral presentation 3/2017
- [16] E. J. Frankberg, L. Joly-Pottuz, F. García Ferré, T. Salminen, T. Douillard, B. Le Saint, V. Kekkonen, S. Chaudhuri, J. Liimatainen, F. Di Fonzo, E. Levänen, Karine Masenelli-Varlot. In situ deformation of nanocrystalline Al₂O₃ thin films at room temperature. European Microscopy Congress 2016, Lyon, France, oral presentation 9/2016. Available from [http://emc-proceedings.com/abstract/in-situ-deformation-of-nanocrystalline-al₂o₃-thin-films-at-room-temperature/](http://emc-proceedings.com/abstract/in-situ-deformation-of-nanocrystalline-al2o3-thin-films-at-room-temperature/)
- [17] W. D. Callister Jr., Materials Science and Engineering: An Introduction, 720 p., 2007
- [18] C. B. Carter, M. G. Norton, Ceramic materials: Science and Engineering, Springer, 701 p., 2007
- [19] S. Takematsu, T. Mizuguchi, H. Nakashima, K.-I. Ikeda, H. Abe. Evaluation of surface energy by molecular dynamics simulation and discussion about cleavage fracture in α -Al₂O₃. Journal of the Ceramic Society of Japan 112:1301, p. 46 – 49, 2004
- [20] G. Irwin. Analysis of stresses and strains near the end of a crack traversing a plate, Journal of Applied Mechanics 24, p. 361–364, 1957

- [21] R. von Mises. Mechanics of solid bodies in the plastically-deformable state - Mechanik der festen Körper im plastisch deformablen Zustand. Nachr. d. Kgl. Ges. Wiss. Göttingen, Math.-phys. Klasse 4, p. 582–592, 1913
- [22] L. Carroll, M. Sternitzke, B. Derby. Silicon carbide particle size effects in alumina based nanocomposites. *Acta Metallurgica et Materialia* 44:11, p. 4543-4552, 1996
- [23] C. R. Jones C. H. Henager Jr., R. H. Jones. Crack bridging by SiC fibers during slow crack growth and the resultant fracture toughness of SiC/SiCf composites. *Scripta Metallurgica et Materialia* 33:12, p. 2067-2072, 1995
- [24] Y. Maniette, M. Inagaki, M. Sakai. Fracture toughness and crack bridging of a silicon nitride ceramic. *Journal of the European Ceramic Society* 7:4, p. 255 – 263, 1991
- [25] R. C. Garvie, R. H. Hannink, R. T. Pascoe. Ceramic Steel? *Nature* 258, p. 703 – 704, 1975
- [26] I. Levin, D. Brandon. Metastable alumina polymorphs: crystal structures and transition sequences. *Journal of the American Ceramic Society* 81:8, p. 1995 – 2012, 1998
- [27] K. P. D. Lagerlöf, A. H. Heuer, J. Castaing, J. P. Rivière, T. E. Mitchell. Slip and Twinning in Sapphire (α -Al₂O₃). *Journal of American Ceramic Society* 77:2, p. 385–397, 1994
- [28] H. W. Rauch, W. H. Sutton, L. R. McCreight. *Ceramic Fibers and Fibrous Composite Materials*. Elsevier, 452 p., 2013
- [29] K. P. D. Lagerlöf. Basal Slip and Twinning in Sapphire (α -Al₂O₃) in: *Plastic deformation of Ceramics*, editors: R.C. Bradt, C.A. Brookes, J.L. Routbort, Springer Science & Business Media, p. 63 – 74, 1995
- [30] R. L. Bertolotti, W. D. Scott. Compressive creep of Al₂O₃ single crystals. *Journal of the American Ceramic Society* 54:6, p. 286 - 291, 1971
- [31] C. T. Bodur, J. Chang, A. S. Argon. Molecular dynamics simulations of basal and pyramidal system edge dislocations in sapphire. *Journal of the European Ceramic Society* 25:8, p. 1431-1439, 2005
- [32] P. W. Bridgman. *Studies in large plastic flow and fracture*, McGraw, 362 p. 1952

- [33] J. Castaing, J. Cadoz, S. H. Kirby. Deformation of Al₂O₃ single crystals between 25 °C and 1800 °C: Basal and prismatic slip. *Journal de Physique Colloques*, 2:C3, p.C3-43 - C3-47, 1981
- [34] J. Castaing, A. He, K. P. D. Lagerlöf, A. H. Heuer. Deformation of sapphire (α -Al₂O₃) by basal slip and basal twinning below 700°C. *Philosophical Magazine*, 84:11, p. 1113 – 1125, 2004
- [35] J. Castaing, J. Cadoz, S.H. Kirby. Prismatic slip of Al₂O₃ single crystals below 1000°C in compression under hydrostatic pressure. *Journal of the American Ceramic Society*, 64:9, 504 – 511, 1981
- [36] J. D. Snow, A. H. Heuer. Slip systems in Al₂O₃. *Journal of American Ceramic Society* 56:3, p. 153 - 157, 1973
- [37] S. L. Korinek, J. Castaing. Slip and twinning in polycrystalline alumina (α -Al₂O₃) deformed under hydrostatic pressure between 600 ° and 1000 °C. *Journal of American Ceramic Society* 86:4, p. 566 – 573, 2003
- [38] M. N. Rahaman. *Ceramic Processing*. Taylor & Francis Group, 473 p., 2007
- [39] H. Mehrer, *Diffusion in Solids*, Springer-Verlag, 654 p., 2017
- [40] R. W. Siegel. Vacancy concentrations in metals. *Journal of Nuclear Materials*. 69-70, p. 117 – 146, 1978.
- [41] K. Matsunaga, T. Tanaka, T. Yamamoto, Y. Ikuhara. First-Principles calculations of intrinsic defects in Al₂O₃. *Physical Review B* 68, 085110, 2003
- [42] T. V. Perevalov, O. E. Tereshenko, V. A. Gritsenko, V. A. Pustovarov, A. P. Yelisseyev, C. Park, J. H. Han, C. Lee. Oxygen deficiency defects in amorphous Al₂O₃. *Journal of applied physics* 108:1, 013501, 2010
- [43] E. D. Aluker, V. V. Gavrilov, S. A. Chermov. Short-lived Frenkel defects in α -Al₂O₃. *Physica status solidi (b)*, 171:1, p. 283 – 288, 1992
- [44] Z. Guo, F. Ambrosio, A. Pasquarello. Oxygen defects in amorphous Al₂O₃: A hybrid functional study. *Applied physics letters* 109:6, 062903, 2016
- [45] C. Århammar, A. Pietzsch, N. Bock, E. Holmström, C. M. Araujo, J. Gråsjö, S. Zhao, S. Green, T. Peery, F. Hennies, S. Amerioun, A. Föhlisch, J. Schlappa, T. Schmitt, V. N. Strocov, G. A. Niklasson, D. C. Wallace, J.-E. Rubensson, B. Johansson, and R. Ahuja. Unveiling the complex electronic structure of amorphous metal oxides. *PNAS* 108:16, p. 6355–6360, 2011

- [46] A.H. Heuer. Oxygen and aluminium diffusion in α - Al_2O_3 : How much do we really understand? *Journal of the European Ceramic Society* 28:7, p. 1495 – 1507, 2008
- [47] R. Nakamura, T. Toda, S. Tsukui, M. Tane, M. Ishimaru, T. Suzuki, H. Nakajima. Diffusion of oxygen in amorphous Al_2O_3 , Ta_2O_5 and Nb_2O_5 . *Journal of Applied Physics* 116:3, 033504, 2014
- [48] T. Nabatame, T. Yasuda, M. Nishizawa, M. Ikeda, T. Horikawa, A. Toriumi. Comparative studies on oxygen diffusion coefficients for amorphous and γ - Al_2O_3 films using ^{18}O isotope. *Japanese journal of applied physics*, 42:1:12, 2003
- [49] F. R. N. Nabarro. Report of a Conference on Strength of Solids, The Physical Society, London, p. 75, 1948 (The conference was held at Bristol University in the UK in 1947.)
- [50] C. Herring. Diffusional viscosity of a polycrystalline solid. *Journal of Applied Physics* 21:5, p. 437, 1950
- [51] R. L. Coble. A model for boundary diffusion controlled creep in polycrystalline materials. *Journal of Applied Physics* 34:6, 1963
- [52] R. S. Gordon. Mass transport in the diffusional creep of ionic solids. *Journal of the American ceramics society* 56:3, p. 147 – 152, 1973
- [53] W. H. Gitzen, *Alumina as a ceramic material*, American Ceramic Society, 253 p., 1970
- [54] J. B. Watchman Jr., I. H. Maxwell. Plastic deformation of ceramic-oxide single crystals. *Journal of the American Ceramics Society* 37:7, p. 291 – 299, 1954
- [55] R. M. Cannon, W. H. Rhodes, A. H. Heuer. Plastic deformation of fine-grained alumina (Al_2O_3): I, Interface-controlled diffusional creep. *Journal of the American Ceramic Society*, 63:1-2, p. 46–53, 1980
- [56] T. Nakagawa, I. Sakaguchi, N. Shibata, K. Matsunaga, T. Mizoguchi, T. Yamamoto, H. Haneda, Y. Ikuhara. Yttrium doping effect on oxygen grain boundary diffusion in Al_2O_3 . *Acta Materialia* 55:19, p. 6627 – 6633, 2007
- [57] D. Prot, M. Le Gall, B. Lesage, A. M. Huntz, C. Monty. Self-diffusion in α - Al_2O_3 . IV. Oxygen grain-boundary self-diffusion in undoped and yttria doped alumina polycrystals. *Philosophical Magazine A* 73:4, p. 935 – 949, 1996

- [58] V. V. Hoang, N. N. Linh, N. H. Hung. Structure and dynamics of liquid and amorphous $\text{Al}_2\text{O}_3 \cdot 2\text{SiO}_2$. *The European physical journal applied physics* 37:1, p. 111 – 118, 2007
- [59] S. K. Lee, C. W. Ahn. Probing of 2 dimensional confinement-induced structural transitions in amorphous oxide thin film. *Scientific reports* 4:, 4200, 2014
- [60] R. Nakamura, T. Shudo, A. Hirata, M. Ishimaru, H. Nakajima. Nanovoid formation through the annealing of amorphous Al_2O_3 and WO_3 films. *Scripta materialia*, 64:2, 197 – 200, 2011
- [61] J. Zhao, S. L. Simon, G. B. McKenna. Using 20-million-year-old amber to test the super-Arrhenius behaviour of glass-forming systems. *Nature Communications* 4, Article number: 1783, 2013
- [62] E. D. Zanotto. Do cathedral glasses flow? *American Journal of Physics* 66:5, p. 392 – 395, 1998
- [63] E. D. Zanotto, P. K. Gupta. Do cathedral glasses flow?—Additional remarks. *American Journal of Physics* 67:3, p. 260 – 262, 1999
- [64] P.W. Anderson. Through the glass lightly. *Science* 267:5204, p. 1615-1616, 1995
- [65] A. L. Greer, Y. Q. Cheng, E. Ma. Shear bands in metallic glasses. *Materials science and engineering: R: Reports* 74:4, p. 71 – 132, 2013
- [66] D. Rodney, A. Tanguy, D. Vandembroucq. Modeling the mechanics of amorphous solids at different length scale and time scale. *Modelling and simulation in materials science and engineering* 19:8, 49 p., 2011
- [67] F. Wakai, S. Sakaguchi, Y. Matsuno. Superplasticity of Yttria-Stabilized Tetragonal ZrO_2 Polycrystals. *Advanced ceramic materials* 1:3, p. 259 – 263, 1986
- [68] T. G. Langdon. Seventy-five years of superplasticity: historic developments and new opportunities. *Journal of Materials Science* 44, p. 5998 – 6010, 2009
- [69] M. D. Groner, F. H. Fabreguette, J. W. Elam, S. M. George. Low-temperature Al_2O_3 atomic layer deposition. *Chemistry of materials* 16:4, p. 639 – 645, 2004

- [70] A. Carradò, M. A. Taha, N. A. El-Mahallawy. Nanocrystalline γ -Al₂O₃ thin film deposited by magnetron sputtering (MS) at low temperature. *Journal of coatings technology and research* 7:4, p. 515 – 519, 2010
- [71] R. Nakamura, M. Ishimaru, H. Yasuda, H. Nakajima. Atomic rearrangements in amorphous Al₂O₃ under electron-beam irradiation. *Journal of Applied Physics* 113:6, 064312, 2013
- [72] F. García Ferré, A. Mairov, L. Ceseracciu, Y. Serruys, P. Trocellier, C. Baumier, O. Kaïtasov, R. Brescia, D. Gastaldi, P. Vena, M. G. Beghi, L. Beck, K. Sridharan, F. Di Fonzo. Radiation endurance in Al₂O₃ nanoceramics. *Scientific Reports* 6, Article number: 33478, 2016
- [73] C. Pan, P. Shen, S.-Y. Chen. Condensation, crystallization and coalescence of amorphous Al₂O₃ nanoparticles. *Journal of Crystal Growth* 299:2, p. 393–398, 2007
- [74] R. Nakamura, M. Ishimaru, A. Hirata, K. Sato, M. Tane, H. Kimizuka, T. Shudo, T. J. Konno, H. Nakajima. Enhancement of nanovoid formation in annealed amorphous Al₂O₃ including W. *Journal of Applied Physics* 110, 064324, 2011
- [75] P. Eklund, M. Sridharan, G. Singh, J. Bottiger. Thermal Stability and Phase Transformations of γ -/Amorphous-Al₂O₃ Thin Films. *Plasma processes and polymers* 6:S1, p. S907–S911, 2009
- [76] C. Cibert, H. Hidalgo, C. Champeaux, P. Tristant, C. Tixier, J. Desmaison, A. Catherinot. Properties of aluminium oxide thin films deposited by pulsed laser deposition and plasma enhanced chemical vapor deposition. *Thin Solid Films* 516, p.1290 – 1296, 2008
- [77] C.C. Koch. Synthesis of nanostructured materials by mechanical milling: problems and opportunities, *Nanostructured Materials* 9:1–8, p. 13–22, 1997
- [78] K. Lu. Nanoparticulate materials: synthesis, characterization, and processing. John Wiley & Sons, 464 p. 2013
- [79] G. R. Karagedov, N.Z. Lyakhov. Mechanochemical grinding of inorganic oxides, *KONA Powder and particle journal* 21, 76 – 87, 2003
- [80] C. Knieke, M. Sommer, W. Peukert. Identifying the apparent and true grinding limit. *Powder Technology* 195:1, p. 25 – 30, 2009

- [81] E. Calvié, J. Réthoré, L. Joly-Pottuz, S. Meille, J. Chevalier, V. Garnier, Y. Jorand, C. Esnouf, T. Epicier, J. B. Quirk, K. Masenelli-Varlot. Mechanical behaviour law of ceramic nanoparticles from transmission electron microscopy *in situ* nano-compression tests. Materials Letters 119:15, p. 107 – 110, 2014
- [82] A. S. Esmaily, S. Mills, J. M. D. Coey. Exceptional room-temperature plasticity in amorphous alumina nanotubes fabricated by magnetic hard anodisation. Nanoscale 9:16, p. 5205 – 5211, 2017
- [83] M. Mačkovíc, T. Przybilla, C. Dieker, P. Herre, S. Romeis, H. Stara, N. Schrenker, W. Peukert, E. Spiecker. A novel approach for preparation and *in situ* tensile testing of silica glass membranes in the transmission electron microscope. Frontiers in materials 4:10, DOI: 10.3389/fmats.2017.00010, 2017
- [84] J. Sun, L. He, Y.-C. Lo, T. Xu, H. Bi, L. Sun, Z. Zhang, S. X. Mao, J. Li. Liquid-like pseudoelasticity of sub-10-nm crystalline silver particles. Nature Materials 13, p. 1007–1012, 2014
- [85] M. Matsui. A transferable interatomic potential model for crystals and melts in the system CaO-MgO- Al₂O₃-SiO₂. Mineralogical Magazine 58A, 571 – 572, 1994
- [86] M. Matsui. Molecular dynamics study of the structures and bulk moduli of crystals in the system CaO-MgO-Al₂O₃-SiO₂. Physics and Chemistry of Minerals, 23:6, p. 345 – 353, 1996
- [87] S. Blonski, S. H. Garofalini. Molecular dynamics study of silica-alumina interfaces, Journal of physical chemistry 100:6, p. 2201 – 2205, 1996
- [88] P. Sarobol, M. Chandross, J. D. Carroll, W. M. Mook, D. C. Bufford, B. L. Boyce, K. Hattar, P. G. Kotula, A. C. Hall. Room temperature deformation mechanisms of alumina particles observed from *in situ* micro-compression and atomistic simulations. Journal of Thermal Spray Technology 25:1-2, p. 82 – 93, 2016
- [89] T. Salminen. Production of Nanomaterials by Pulsed Laser Ablation. Doctoral Thesis 1121, Tampere University of Technology, 2013
- [90] P. J. Heaney, E. P. Vicenzi, L. A. Giannuzzi, K. J. T. Livi. Focused ion beam milling: A method of site-specific sample extraction for microanalysis of Earth and planetary materials. American Mineralogist 86, p. 1094 – 1099, 2001

- [91] PI 95 PicoIndenter User manual, Hysitron Inc. 2011
- [92] G. Gutiérrez, B. Johansson. Molecular dynamics study of structural properties of amorphous Al_2O_3 . *Physical review B* 65:10, 104202, 2002
- [93] G. Gutiérrez, A. B. Belonoshko, R. Ahuja, B. Johansson. Structural properties of liquid Al_2O_3 : a molecular dynamics study. *Physical review E* 61:3, p. 2723 – 2729, 1999
- [94] A. B. Belonoshko. Melting of corundum using conventional and two-phase molecular dynamic simulation method. *Physics and chemistry of minerals* 25:2, p. 138 – 141, 1998
- [95] J. Murray, K. Song, W. Huebner, M. O’Keefe. Electron beam induced crystallization of sputter deposited amorphous alumina thin films. *Materials Letters* 74, p. 12 – 15, 2012
- [96] D. B. Williams, C. B. Carter. *Transmission electron microscopy part 1: Basics*” Springer Science, 757 p., 2009
- [97] G. Alcalá, P. Skeldon, G. E. Thompson, A. B. Mann, H. Habazaki, K. Shimizu. Mechanical properties of amorphous anodic alumina and tantala films using nanoindentation. *Nanotechnology* 13:4, p. 451 – 455, 2002
- [98] A. Malkin, V. Kulichikhin, S. Ilyin. A modern look on yield stress fluids. *Rheologica Acta* 56:3, p. 177 – 188, 2017
- [99] H. Zhang, J. Tersoff, S. Xu, H. Chen, Q. Zhang, K. Zhang, Y. Yang, C.-S. Lee, K.-N. Tu, J. Li, Y. Lu. Approaching the ideal elastic strain limit in silicon nanowires, *Science advances* 2:8, 2016
- [100] Z. Polo, R. Eulalio. On the Taylor–Quinney coefficient in dynamically phase transforming materials: Application to 304 stainless steel. *International Journal of Plasticity* 40, p. 185 – 201, 2013
- [101] D. A. Ditmars, S. Ishihara, S. S. Chang, G. Bernstein, E. D. West. Enthalpy and heat-capacity standard reference material: synthetic sapphire ($\alpha\text{-Al}_2\text{O}_3$) from 10 to 2250 K. *Journal of research of the national bureau of standards* 87:2, p. 159, 1982
- [102] V. G. Hill, R. Roy, E. F. Osborn. The system alumina-gallia-water. *Journal of the American ceramics society*. 35:6, p. 135 – 142, 1952
- [103] N. A. Toropov. *Transactions of 7th International Ceramics Congress, United Kingdom* p. 435-442, 1960

- [104] A. van der Rest, H. Idrissi, F. Henry, A. Favache. D- Schryvers, J. Proost. J.-P. Raskin, Q. Van Overmeere, T. Pardoen. Mechanical behavior of ultrathin sputter deposited porous amorphous Al_2O_3 . *Acta Materialia* 125, p. 27 – 37, 2017
- [105] D. Mercier, V. Mandrillon, G. Parry, M. Verdier, R. Estevez, Y. Bréchet, T. Maindron. Investigation of the fracture of very thin amorphous alumina film during spherical nanoindentation. *Thin Solid Films* 638, p. 34-47, 2017
- [106] H. A. Barnes. *A handbook of elementary rheology*. University of Wales, 200 p., 2000
- [107] N. Kumagai, S. Sadao, I. Hidebumi. Long-term creep of rocks: results with large specimens obtained in about 20 years and those with small specimens in about 3 years. *Journal of the society of materials science (Japan)* 27:293, p. 155 – 161, 1978
- [108] J. C. Mauro, Y. Yue, A. J. Ellison, P. K. Gupta, D. C. Allan. Viscosity of glass-forming liquids. *PNAS* 24:47, p. 19780-19784, 2009
- [109] Y. Yu, M. Wang, D. Zhang, B. Wang, G. Sant, M. Bauchy. Stretched exponential relaxation of glasses at low temperature. *Physical review letters* 115:16, 165901, 2015
- [110] Corning museum of glass. Does glass flow? <http://www.cmog.org/article/does-glass-flow> , cited 05.09.2017
- [111] Gizmodo. The ‘glass is a liquid’ myth has finally been destroyed. <http://io9.gizmodo.com/the-glass-is-a-liquid-myth-has-finally-been-destroyed-496190894> , cited 05.09.2017
- [112] P. K. Misra. *Physics of Condensed Matter*. Academic Press, 688 p., 2011
- [113] C. G. Darwin, R. H. Fowler. On the partition of energy. *Philosophical magazine and journal of science* 44:261, p. 450 – 479, 1922
- [114] W. H. Qi, M. P. Wang. Size and shape dependent melting temperature of metallic nanoparticles. *Materials Chemistry and Physics* 88:2-3 p. 280 – 284, 2004
- [115] S-H. Jen, J. A. Bertrand, S. M. George. Critical tensile and compressive strains for cracking of Al_2O_3 films grown by atomic layer deposition. *Journal of Applied Physics* 109:8, 084305, 2011

Tampereen teknillinen yliopisto
PL 527
33101 Tampere

Tampere University of Technology
P.O.B. 527
FI-33101 Tampere, Finland

ISBN 978-952-15-4102-5
ISSN 1459-2045